

# Durham E-Theses

---

## *An Automated NLO Framework in Sherpa*

ARCHIBALD, JENNIFER

---

### How to cite:

ARCHIBALD, JENNIFER (2011) *An Automated NLO Framework in Sherpa*, Durham theses, Durham University. Available at Durham E-Theses Online: <http://etheses.dur.ac.uk/3286/>

---

### Use policy

The full-text may be used and/or reproduced, and given to third parties in any format or medium, without prior permission or charge, for personal research or study, educational, or not-for-profit purposes provided that:

- a full bibliographic reference is made to the original source
- a link is made to the metadata record in Durham E-Theses
- the full-text is not changed in any way

The full-text must not be sold in any format or medium without the formal permission of the copyright holders.

Please consult the [full Durham E-Theses policy](#) for further details.

# **An Automated NLO Framework in SHERPA**

Jennifer Archibald

A thesis submitted to Durham University  
for the degree of Doctor of Philosophy



## Abstract

There has recently been a strong drive towards next-to-leading order (NLO) accuracy in Monte Carlo event generators. This thesis is concerned with the implementation of a framework for NLO calculations within the matrix element generator AMEGIC++, which forms part of the Monte Carlo event generator SHERPA. An interface is presented for the connection of one-loop matrix elements to SHERPA, conforming with the Binoth Les Houches Accord. Automated Catani-Seymour dipole subtraction is presented for the cases of QCD corrections for processes involving massive final state particles, and the supersymmetric partners of quarks and gluons, namely squarks and gluinos. Similar dipole subtraction techniques are also applied to the case of photonic corrections. An automated implementation of on-shell subtraction, relevant for separating real-emission NLO corrections from leading order production and decay processes, is also presented. With the completion of this work, the event generator SHERPA, when interfaced to suitable one-loop code, is equipped to calculate all necessary components of QCD and electroweak NLO calculations.

©2011 The copyright of this thesis rests with the author. No quotation from it should be published without the prior written consent and information derived from it should be acknowledged.

## Acknowledgements

Firstly, I would like to thank my supervisor, Frank Krauss for his guidance and wisdom, generously offered and gratefully received, over the duration of this research.

I thank my collaborators on the SHERPA team for their help and support; particularly Tanju Gleisberg for invaluable help and close collaboration at the very initial stages of this project.

I would also like to extend my gratitude to Stefan Dittmaier and Max Huber for many useful discussions on the intricacies of electroweak higher-order corrections, and for providing support for and numbers of their RADY program, as well as their hospitality at Freiburg University.

For useful discussion of the technicalities of NLO SUSY calculations, particularly in reference to on-shell subtraction, I would like to thank Tilman Plehn and Dorival Gonçalves Netto.

I also thank Paul Mellor for help with the one-loop matrix element for single-top production.

Finally, I would also like to thank my friends and family for their inexhaustible patience and support.

# Contents

<b>1. Introduction</b>	<b>2</b>
1.1. Testing the Theory	2
1.2. A Monte Carlo Event Generator	3
1.3. Next-to-leading Order	8
1.4. NLO Calculations	9
<b>2. Binoth Les Houches Accord</b>	<b>16</b>
2.1. Basic Principles	16
2.2. Special Considerations for EW Interface	19
2.2.1. Regularisation Scheme	19
2.2.2. Renormalisation Scheme	21
2.2.3. Unstable Massive Particles	22
2.3. Sherpa/Rady Interface	23
<b>3. Dipole Formalism</b>	<b>29</b>
3.1. Introduction	29
3.2. Observables	30
3.3. Soft and Collinear Singularities	31
3.4. Collinear Counterterm	32
3.5. Dipole Splitting Functions	34
3.6. Integrated Dipole Terms	36
3.7. Proliferation of Terms	37
3.7.1. Phase Space Restriction	40
3.8. General Structure of the Calculation	42
3.9. Summary	45
<b>4. Massive QCD Dipoles</b>	<b>46</b>
4.1. Quasi-collinear Limit	47
4.2. Organisation of the Calculation	48

---

4.3. Phase Space Restriction . . . . .	50
<b>5. Supersymmetry: Dipoles and On-Shell Subtraction</b>	<b>51</b>
5.1. Introduction to Supersymmetry . . . . .	51
5.2. QCD Dipoles for SUSY Processes . . . . .	53
5.2.1. Phase space restriction . . . . .	54
5.3. On-Shell Subtraction . . . . .	54
5.3.1. Width as a Regulator . . . . .	57
5.3.2. A Standard Model Example . . . . .	58
<b>6. Photonic Corrections</b>	<b>60</b>
6.1. Real Subtraction Terms . . . . .	61
6.2. Integrated Subtraction Terms . . . . .	62
6.3. Renormalisation Scheme . . . . .	62
6.4. Regularisation Scheme . . . . .	63
6.5. Factorisation Scheme . . . . .	64
6.6. Recombination and Cuts on Real-emission Phase Space . . . . .	64
<b>7. Tests of the Implementation</b>	<b>66</b>
7.1. Internal Tests of Dipole Subtraction . . . . .	66
7.1.1. Technical Cut-off Parameter Variation . . . . .	66
7.1.2. Phase Space Restriction Parameter . . . . .	70
7.2. Internal Tests of On-shell Subtraction . . . . .	72
7.2.1. Width Variation . . . . .	77
7.2.2. On-shell Cancellation . . . . .	78
7.3. Comparative Tests . . . . .	80
7.4. First Physical Applications . . . . .	82
<b>8. Summary</b>	<b>89</b>
<b>A. Massive QCD dipoles</b>	<b>91</b>
A.1. Notation . . . . .	91
A.2. Final-final . . . . .	92
A.2.1. $Q \rightarrow Q g$ . . . . .	92
A.2.2. $q \rightarrow q g$ . . . . .	95
A.2.3. $g \rightarrow g g$ . . . . .	96
A.2.4. $g \rightarrow Q \bar{Q}$ . . . . .	97
A.2.5. $g \rightarrow q \bar{q}$ . . . . .	98

<b>A.3. Final-Initial</b> . . . . .	99
A.3.1. $Q \rightarrow Q \, g$ . . . . .	99
A.3.2. $g \rightarrow Q \, \bar{Q}$ . . . . .	99
<b>A.4. Initial-final</b> . . . . .	101
A.4.1. $\tilde{a}i : q, a : q, i : g$ . . . . .	101
A.4.2. $\tilde{a}i : g, a : q, i : q$ . . . . .	101
A.4.3. $\tilde{a}i : q, a : g, i : q$ . . . . .	101
A.4.4. $\tilde{a}i : g, a : g, i : g$ . . . . .	102
<b>A.5. Organisation of the Calculation</b> . . . . .	102
<b>B. SUSY Integrated Dipole Phase Space Restriction Formulae</b>	<b>109</b>
B.1. Final state squark emitter, with final state spectator . . . . .	109
B.2. Final state squark emitter, with initial state spectator . . . . .	110
<b>C. On-shell Subtraction Technicalities</b>	<b>111</b>
C.1. Reshuffling Procedure . . . . .	111
C.2. Higher Multiplicity Final States . . . . .	113
<b>D. Photonic Corrections</b>	<b>116</b>
D.1. Notation and Conventions . . . . .	116
D.2. Integrated Subtraction Terms . . . . .	116
<b>Bibliography</b>	<b>120</b>
<b>List of Figures</b>	<b>128</b>
<b>List of Tables</b>	<b>130</b>

# Chapter 1.

## Introduction

*“It is the theory that decides what we can observe.”*

— Albert Einstein, 1879–1955

### 1.1. Testing the Theory

For the past fifty years, experimental particle physicists have been using colliders to explore the fundamental particles and forces. As the years have passed, the scale of these experiments has increased, but the underlying philosophy is the same: by giving two particles a large centre of mass energy, and allowing them to interact, we can study the outgoing products of the collision to learn about the building blocks of the universe, and how they interact.

The Large Hadron Collider (LHC) at the European Organisation for Nuclear Research (CERN) is the most ambitious project of this kind to date; with significantly more energy and luminosity than any previous venture, not only will it lead the search for new physics by exploring higher energies, but the abundance of statistics will allow precision tests of known physics described by the Standard Model.

However, this anticipated leap forward in understanding is not without its challenges. On a fundamental level, the very construction of the machine and detectors was an engineering feat of Herculean proportions, but the labours do not end there. The work of understanding the detectors is well under way, but it will take a long time before they are fully understood and calibrated. With more luminosity than ever before, the

problem of pile-up, where there is more than one interaction per bunch crossing, must be addressed. The identification of and control over systematic uncertainties arising from, for example, particle identification, background rejection, energy scales and resolution functions is another daunting task (see e.g. reference [1]). And, on top of all this, the very collection and analysis of data will take many years.

However, the challenge is not just for the experimental community. Without a precise understanding of the predictions of the Standard Model, deviations from these expectations indicating new physics may not be recognisable. And without a strong understanding of the predictions of differing Beyond the Standard Model (BSM) theories, new physics, once found, will be uncharacterisable.

For most experimental observables at particle colliders, theoretical predictions are fundamentally based on perturbative expansions. The expansion parameters are taken to be coupling constants, which indeed are, in general, small. However, while asymptotic freedom means that the coupling for Quantum Chromodynamics (QCD) is small at large momentum transfer, the coupling becomes large at small energy scales, which leads to the breakdown of perturbation theory, and large non-perturbative effects. As it is a hadron collider, all interactions at the LHC will involve coloured particles, at least in the initial state, so a deep understanding of the behaviour of QCD, even in these non-perturbative regions, is imperative. Fortunately, however, many non-perturbative effects are universal (that is, not process dependent), and may thus be phenomenologically modelled. Computer programs have been written to simulate these perturbative and non-perturbative aspects of a particle collision. These programs are called Monte Carlo event generators.

## 1.2. A Monte Carlo Event Generator

A Monte Carlo event is a complex mix of perturbative and non-perturbative physics, and the constituent parts of the simulation range from well-understood, theoretically grounded calculations, to wholly phenomenological models, constrained by data. As our link between theoretical predictions and experimental results, it is imperative that our Monte Carlo simulations accurately reflect the physics of theoretical models, and are as predictive as possible. A recent extensive review, covering all aspects of Monte Carlo physics, is given by reference [2]. There are several publicly available multi-purpose

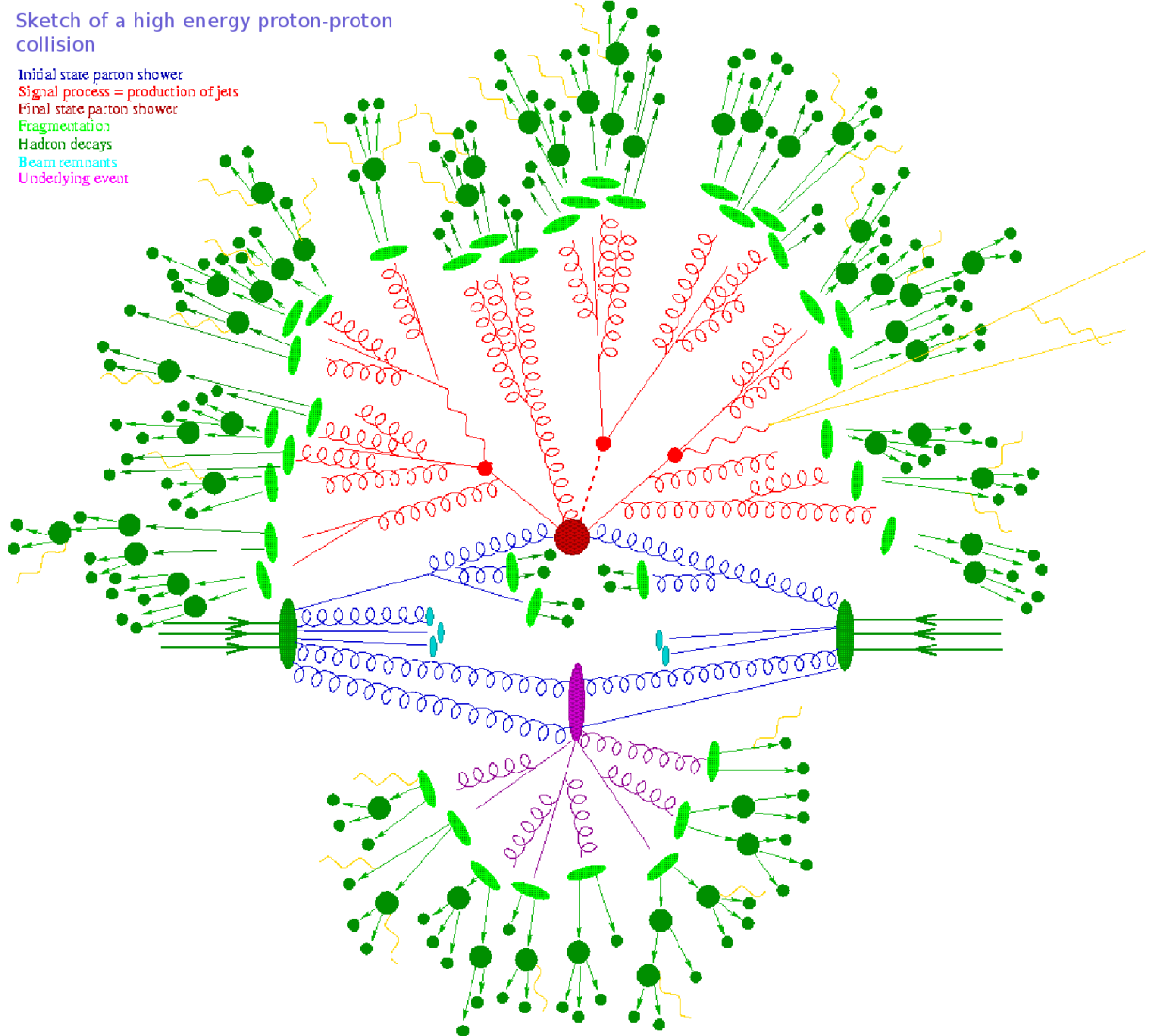


**Figure 1.1.:** A pictorial representation of a Monte Carlo event ([www.sherpa-mc.de](http://www.sherpa-mc.de)).

Monte Carlo event generators, which provide some or all of the following features, including SHERPA [3], Herwig(++) [4, 5], Pythia [6, 7] and Ariadne [8].

The Monte Carlo event generator is based on the parton model of QCD, first postulated in the late 60's by Bjorken and Feynman, and since detailed in many particle physics textbooks, such as references [9–11]. The only experimentally accessible strongly interacting states are colourless combinations of the fundamental coloured particles, quarks and gluons, called hadrons. The fundamental particles contained within a hadron are referred to as *partons*. In this low energy limit, the strong coupling is large, meaning that not only are the partons strongly bound together, but also the structure and interactions of the partons within the hadron cannot be described by perturbation theory.

The hadron consists of a set of *valence* quarks, relating to the quantum numbers of the hadron, and also a *sea* of gluons and quark and anti-quark pairs.

While perturbation theory may not be used to describe the hadron, it may still be used to describe particle interactions at high energy particle colliders, where the distances probed are small, and momentum transfers are large. In this regime, the strong coupling becomes small [12, 13], and perturbation theory is valid. As such, when probed at high energies, hadrons may be described as a collection of *asymptotically free* partons.

According to the factorisation theorem [14], the interactions of hadrons in a particle collider may be described by a convolution of non-perturbative functions describing the distributions of partons within the hadrons with a leading order perturbative calculation of the scattering of the individual partons contained within the hadrons. This factorisation of the non-perturbative long distance effects and the perturbative hard cross section forms the basis of the parton model, and all perturbative theoretical predictions for hadron colliders.

The functions describing the distributions of these partons within the hadron are called parton distribution functions (PDFs). At leading order, the PDFs may be considered to represent the probability of finding a particular parton, carrying a particular momentum fraction, in a particular hadron which is probed at a particular scale, known as the *factorisation scale*. The PDFs acquire a dependence on the factorisation scale through the absorption of collinear singularities into a ‘bare’ distribution and thus the evolution of the PDFs under changes in the factorisation scale are perturbatively described. Therefore, if the PDFs are defined at one scale, they may be evolved to any other scale. The distributions themselves may not be calculated from first principles, as they are non-perturbative quantities, associated with the long distance behaviour of the partons. They are, however, process-independent, and can therefore be parametrised and tuned to data.

Of course, after the interaction, the resultant, or final-state, coloured partons may not be considered to be free particles: due to confinement, they must fragment into colourless hadrons. This process may be described by so-called fragmentation functions. These non-perturbative functions are very similar in concept to the PDFs, consisting of non-perturbative distributions with perturbative scale evolution, and, therefore, must also be parameterised and experimentally measured.

Once connected to a phase space generator these simple constituent parts can produce a crude estimate of experimental results.

However, to increase the accuracy and predictive power there are many improvements which can be made to this simple Monte Carlo event generator. It is known that charged particles radiate. In particular, it can be seen from the production of jets at colliders that coloured particles radiate many further soft or collinear partons, creating a cascade, or shower, of particles. In a Monte Carlo, this can be simulated using a parton shower algorithm, which produces radiation probabilistically from both initial and final state coloured partons. A theoretically rigorous parton shower algorithm resums potentially large soft and collinear logarithmic contributions to all orders in the strong coupling, in regions of phase space where these terms are enhanced, improving the convergence of the perturbative series.

The same principle may be applied to electromagnetic radiation, and the effect of photon radiation from initial and final state particles may be included in a similar way.

A Monte Carlo can be further improved by considering the interface between matrix elements and the parton shower. Both fixed order matrix elements and parton showers are approximations to the true scattering amplitude, but the two approximations are valid in different regions of phase space. Fixed order matrix elements are an excellent approximation for describing final states with high energy, well-separated partons; but diverge unphysically when final state partons are soft or collinear, and can, computationally speaking, only be feasibly calculated for a relatively small number of final state particles. Parton showers resum the large logarithms in these areas of phase space producing a much better approximation of emissions in the soft or collinear limit, and can create a large number of final state particles; but do not accurately describe hard wide-angle emissions. Therefore, a combination of the two approximations would be advantageous: a system which allows the matrix element to describe all hard, wide-angle emissions, and the parton shower to describe all soft or collinear emissions. This requires mixing matrix element contributions with greater final state multiplicities with matrix element contributions with lesser final state multiplicities, where the extra emissions are described by the parton shower. Thus, a merging algorithm must be employed to ensure that these contributions may be added without double counting, while ensuring that all regions of phase space are covered. Several such algorithms have been produced and implemented in various Monte Carlos [15–20].

The simple idea of independent fragmentation of final state partons into hadrons, may be made more sophisticated by considering the colour connections between various final state partons. There are several models for this hadronisation treatment, and they may be roughly separated into two classes: string fragmentation [21–23], where a

string-like colour connection between final state partons breaks up due to spontaneous quark pair production; and cluster hadronisation [24, 25], where colour-singlet clusters with low invariant masses are formed and decay into hadrons.

Our seemingly naive (yet remarkably effective) idea of factorisation allows us to describe our incoming hadrons as a pair of free partons, with probabilistic distributions given by the PDFs. However, this is obviously only an approximation, as we know that the incoming hadrons, by definition, consist of a collection of partons. The interactions of these remaining partons, which are not involved in the hard interaction, result in additional soft activity in the event, called the underlying event. However, there is also no reason why there may not be more than one pair of partons involved in hard interactions from one pair of hadrons. This effect is modelled by Multiple Parton Interactions (MPI), which allow for more than one hard perturbative interaction per event. While the perturbative part of this treatment is well understood, it is still unclear how one should properly treat the parton distribution functions for these processes. Reviews of this subject can be found in references [26–28].

As we can see from Figure 1.1, our improved Monte Carlo event consists of a complicated web of processes, resulting in highly complex final states. However, at the centre of it all is still our simple leading order perturbative matrix element, shown in the figure as the dark red central blob. Therefore, despite our improvements, the accuracy of any Monte Carlo simulated event is still limited by the perturbative accuracy of the matrix element.

Fixed order matrix element uncertainties may be reduced by calculating the next-to-leading order (NLO) corrections. As well as the challenges of calculating the components of an NLO calculation, integrating these corrections into a full Monte Carlo event generation framework presents its own challenges, and recently much progress has been made towards this. The MC@NLO [29] and POWHEG [30–32] algorithms allow event generation with NLO matrix elements, and very recent developments have addressed the problem of multi-jet merging of the NLO matrix elements and parton showers [33, 34]. These are huge leaps forward in the quest for higher accuracy and more predictive powers for Monte Carlo event generators. However, this new technology first requires the framework in which to calculate NLO cross sections using a Monte Carlo event generator, and this topic shall be discussed in this thesis.

### 1.3. Next-to-leading Order

With any perturbative expansion, the leading order term is generally only a crude approximation of the full result. Even more worryingly, the quality of this approximation is difficult to quantify, without knowledge of the next term in the expansion.

A naive order-of-magnitude estimate of the size of the next-to-leading order (NLO) term in the expansion is given by the size of the expansion parameter. Using this rough rule of thumb, QCD corrections should be of the order of  $\sim 10\%$ , and electroweak corrections of the order of a few percent of the leading order term. However, the importance of NLO corrections also depends not only on the process of interest, but also on the particular areas of phase space studied, and the true effect of the NLO corrections may be much greater than these rough estimates.

Traditionally, in QCD, the theoretical error due to the truncation of the expansion is estimated by varying the renormalisation and factorisation scales of the calculation. This provides an estimate of the error since the full all-orders result must be independent of these scales, so any residual scale dependence is a result of the truncation, rather than the underlying theory.

A closer look at the dependency of the coupling on the renormalisation scale can easily explain why a leading order calculation is, in many cases, insufficient to accurately describe data.

The running of the strong coupling means that the value of the coupling falls with the scale at which it is evaluated. A typical scale of the relevant process is usually chosen for this renormalisation scale, although the exact choice is somewhat arbitrary: there is no reliable, universal choice which may be considered more correct than any other. This potentially huge arbitrary variation in the coupling is technically a higher order correction, and thus, to leading order accuracy, there is no distinction between the results for any choice of scale. The effect of the falling coupling on a leading order process is magnified for higher multiplicities, where the coupling appears to a higher power. In fact, the uncertainty in the cross section due to the running of the coupling scales approximately linearly with the perturbative order, as

$$(\alpha_s + \Delta\alpha_s)^n \approx \alpha_s + n\Delta\alpha_s . \quad (1.1)$$

Leading order calculations lead to scale variation plots with a steeply falling total cross section.

Therefore, the total normalisation of the leading order cross section is almost completely arbitrary, and at least NLO accuracy is required for an estimate of the total cross section.

Of course, if the effect of including an NLO correction is only equivalent to setting the overall normalisation of the leading order process, then a constant reweighting factor, known as a K-factor, is all that is required. However, the NLO correction will, in general, not produce a constant K-factor over all of the phase space, in which case it is not sufficient to set the overall normalisation of the leading order cross section using the NLO result.

Including the NLO corrections, the scale uncertainties for any particular calculation are, in general, significantly reduced, which is indicative of the improved approximation to the full result.

## 1.4. NLO Calculations

The NLO cross section for a process with  $m$  external particles may be written as

$$\sigma_{NLO} = \int_m d\sigma_{LO} + \int_m d\sigma_V + \int_{m+1} d\sigma_R , \quad (1.2)$$

where the first two terms represent the Born and virtual loop contributions respectively, which are integrated over an  $m$ -particle phase space, and the third term represents the real-emission contribution, which is integrated over an  $m + 1$ -particle phase space.

Schematic diagrams for these contributions to the NLO calculation are shown in Figure 1.2. The virtual contribution involves appropriately-named *loop* diagrams, with two particle lines of the Born diagram connected by an additional propagator, creating a full circle, or loop, of internal propagator lines. These virtual diagrams are contracted with the Born diagram, resulting in a contribution with two additional powers of the coupling. The real-emission contribution is given by diagrams representing the leading order process with one additional (unresolved) parton. Squaring the real-emission diagrams again results in a contribution with two additional powers of the coupling.

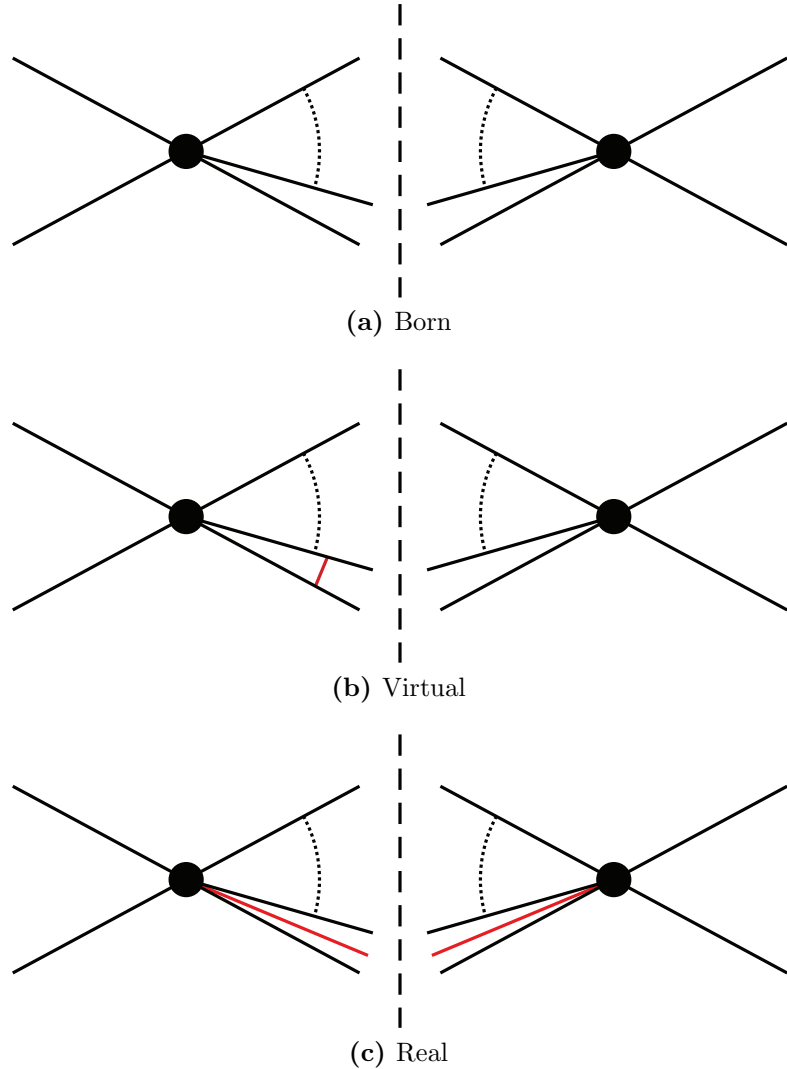


**Figure 1.2.:** Schematic diagrams of NLO contributions.

The Born and real emission matrix elements are trivial to calculate; an automated general purpose matrix element generator, such as AMEGIC++, can easily produce these terms. The virtual matrix elements are, however, less trivially obtained. For many years, the virtual matrix elements have had to be calculated separately for each process studied, and it is only in recent years that the first automated tools for their calculation have been developed [35–43]. Many of the existing virtual matrix elements are accessible only through standalone codes developed by different authors, using different conventions. In order to make use of these existing codes in a general NLO framework, an interface must be constructed. However, it is essential that the conventions, scheme choices and parameters are identical between the one-loop program, and the NLO framework. As such, an industry-wide standard has been established, allowing the inclusion of external

loop matrix elements into NLO frameworks, via a standard interface. Chapter 2 of this thesis describes the Binoth Les Houches Accord for electroweak NLO calculations, and its first implementation in SHERPA.

The virtual cross section must be integrated over the same phase space as the leading order cross section, having the same external particles. However, there is an additional momentum, which runs in the loop, which is undetermined from the external momenta by momentum conservation. This loop momentum must be integrated over analytically, and leads to singularities in the cross section. These singularities may be separated into two distinct classes: ultraviolet divergences and infrared divergences. Ultraviolet (UV) divergences are associated with the upper limit (or lack thereof) of this loop momentum integral, and are removed by so-called *renormalisation*. Naively, at leading order, it is assumed that parameters in our theory, such as masses and coupling constants, correspond directly to experimentally measurable quantities. However, the radiative corrections to these ‘bare’ parameters diverge, which is directly contradicted by finite experimental measurements. The trick to renormalisation is the realisation that the bare parameters are not physical quantities, and only the combination of the bare quantities and the corrections are measured. Therefore, if the bare quantities are assumed to be infinite, in such a way that their infinities cancel exactly those UV divergences from the loop corrections, then what is left is a finite, measurable, *renormalised* quantity. This redefinition is applied to masses, couplings and fields in the theory, and the UV divergences are thus absorbed into the redefinitions. It should be noted that while this procedure solves the problem of UV divergences, there is some freedom in the exact implementation, resulting in a residual dependence on the *renormalisation scheme*.

The other type of divergence which appears in the loop momentum integral, namely infrared (IR) divergences, cannot be absorbed into this redefinition.

The IR divergences result from occasions when the momentum of one of the particles in the loop becomes on-shell ( $p^2 \rightarrow m^2$ ), or collinear to another external momentum. These divergences cancel with divergences in the real-emission cross section, where the extra, unresolved particle becomes soft or collinear with an external particle. This cancellation is guaranteed for physically meaningful quantities by the Kinoshita-Lee-Nauenberg and the Bloch-Nordsieck theorems [44–46].

When NLO cross sections are computed analytically, this cancellation can occur on the integrand level, thus resulting in a finite and calculable cross section.

However, analytical calculations are of limited use. Results must be calculated for each observable independently. High multiplicity final states involve tortuously complicated phase space integrals, even without including experimental cuts. In practice, analytical calculations are only possible for a few simple inclusive observables.

Monte Carlo integration offers many benefits, as well as the ability to cope with complicated high-multiplicity phase space integrals. Many observables may be studied simultaneously, without extra computation. Experimental cuts and complicated observables and analyses present no problem.

However, for numerical integration methods such as Monte Carlo, the two divergent contributions must be combined after integration, as the two phase space integrals (the  $m$ -particle phase space for the virtual and  $m+1$ -particle phase space for the real-emission) must be computed separately.

This has two consequences. Firstly, the divergences in the virtual cross section must be regularised in order to meaningfully quantify its value. This is possible as the integration over the loop momentum is performed analytically, before the Monte Carlo integration. There are several common choices for regularisation schemes, the two most popular being dimensional regularisation, and mass regularisation. By describing the divergence in terms of some infinitesimally small parameter, it is possible to both isolate the divergence, extracting the finite part, and also to quantify the divergent part, in order to check the cancellation with the real-emission contribution. Once the divergences associated with the integration of the loop momentum are regularised, the integral over the external momenta may be performed numerically.

The second consequence is for the calculation of the real-emission contribution. The divergences in the real-emission cross section are not as easily regularised. The singularities manifest themselves in a less explicit way, with the cross section simply diverging in certain regions of phase space. Thus, naively, the  $m+1$ -particle phase space integral is completely unsuited to numerical integration.

However, the situation is not as dire as this would suggest. While the cross section does diverge in certain areas of phase space, the location of these divergences are known: where one of the external particles has very low energy (is soft), or is collinear to another particle. Not only this, but the structure of the singularity is universal, factorising as a process independent singular factor multiplying the underlying Born leading order cross section. The universal structure of the divergences is described in detail in Section 3.3.

As such, it is possible to isolate and remove these divergences. Several algorithms have developed for this purpose. These can be roughly separated into two classes: phase space slicing techniques, and subtraction methods.

Phase space slicing [47–52] involves separating the phase space into finite regions where the cross section may be safely calculated, and divergent regions where the cross section should not be integrated numerically. This separation is controlled by at least one cut off parameter, for example in the energy and relative angles of external particles, or in invariant mass variables. The cut off parameters are unphysical, and as such, the final result should be independent of their values. Below the cut off, where the cross section diverges, the integration is performed analytically, cancelling the divergences in the virtual part.

However, this procedure can prove inefficient. The cut off parameter is constrained to be small, as the factorisation of the cross section used in calculating the contribution below the cut off is only valid in the soft or collinear limit. Thus, if the cut off is too high, the accuracy of the result is reduced. However, if the cut off is too low, then logarithms of the cut off scales, which are a result of introducing the unphysical phase space slice, may become large. These logarithms should cancel between the analytically and numerically integrated slices. However, if the scale becomes too small, and the logarithms become too large, then the calculation faces the numerical instability of subtracting large numbers, as well as the inefficiency of the Monte Carlo spending time precisely determining the integral of a large term which cancels in the final result anyway. Thus, phase space slicing methods may suffer from relative inefficiency and inaccuracy (see, for example references [53, 54]).

The other set of methods, subtraction algorithms, are becoming increasingly popular. Widely used examples of this method include the Frixione-Kunszt-Signer (FKS) subtraction formalism [55] and the Catani-Seymour dipole subtraction formalism [56], although other variations have been used [51, 57–65]. These techniques rely on the universal structure of infrared divergences and the ability to construct suitable local subtraction terms: by constructing an auxiliary term which exactly matches the divergent part of the cross section, without introducing any additional spurious poles, the divergence may be subtracted. This leads to a new integral, which is finite everywhere in phase space, and may, thus, be numerically integrated. Therefore, we can write,

$$\sigma_{NLO} = \int_m d\sigma_{LO} + \int_m d\sigma_V + \int_{m+1} [d\sigma_R - d\sigma_A] + \int_{m+1} d\sigma_A , \quad (1.3)$$

where the terms labelled  $A$  are the subtraction terms. Of course, an arbitrary term may not just be subtracted from the cross section, without changing its overall result. Therefore, the subtraction term must be added again, resulting in the last term in equation (1.3).

In equation (1.3), the first integration over the  $m + 1$ -particle phase space is now finite, as the subtraction term exactly matches the divergent parts of the real emission cross section. Note, however, that the problem has not been solved, only moved, as the second  $m + 1$ -particle phase space integral is still divergent.

If the subtraction term is chosen carefully, then it is possible to integrate the subtraction term analytically over a one-particle phase space. This integration is obviously divergent, but the same regularisation scheme used for the calculation of the virtual cross section may be used for this analytical integration. As such, the integrated subtraction term becomes a numerical integral over an  $m$ -particle phase space, and its regularised poles exactly cancel the poles in the virtual cross section. The resulting structure for the calculation is given by

$$\sigma_{NLO} = \underbrace{\int_m d\sigma_{LO}}_{\mathcal{B}} + \underbrace{\int_m \left[ d\sigma_V + \int_1 d\sigma_A \right]}_{\mathcal{VI}} + \underbrace{\int_{m+1} [d\sigma_R - d\sigma_A]}_{\mathcal{RS}} . \quad (1.4)$$

As the construction of the subtraction terms relies on the universal structure of divergences, rather than any process-specific information, it is possible to implement these terms in an entirely general, automated, process-independent way. This full automation of a subtraction algorithm was first achieved for the case of Catani-Seymour dipole subtraction for massless QCD [66] in the matrix element generator AMEGIC++, within the SHERPA framework, and has since been implemented by several independent groups, such as TeVJet [67] (automated Catani-Seymour dipole subtraction), MadDipole [68–70] (automated Catani-Seymour dipole subtraction for massless and massive QCD, and photonic corrections), MadFKS [71] (automated FKS subtraction), AutoDipole [72] (automated QCD dipole subtraction), SuperAutoDipole [73] (automated QCD dipole subtraction, including supersymmetric partons).

The details of the Catani-Seymour dipole subtraction procedure, are reviewed in Chapter 3, with particular reference to the automation of dipole subtraction in AMEGIC++ for massless QCD partons [66].

In Chapter 4, the extension of an implementation of massless QCD dipoles to include massive coloured final states is discussed. In Chapter 5, the further extension to NLO QCD for supersymmetric theories is presented, including the derivation of phase space restriction formulae, and an automatisation of on-shell subtraction procedures for separating real-emission corrections from leading order production and decay.

In Chapter 6, the application of the dipole formalism to photonic corrections is discussed.

Tests of the implementations of these tools are presented in Chapter 7, including the validation of results by comparison to independent existing code or results, where possible. The first physical applications of the framework are presented.

# Chapter 2.

## Binoth Les Houches Accord

### 2.1. Basic Principles

As discussed in Section 1.4, at NLO, the leading order Born cross section for a  $2 \rightarrow m$  process receives two additional contributions: the virtual one-loop amplitude, and the real-emission amplitude. The virtual amplitude occupies the same  $m$ -particle phase space as the leading order amplitude, but the real emission amplitude includes an additionally emitted final state particle, and therefore is integrated over an  $(m + 1)$ -particle phase space. Thus the calculation has the structure

$$\sigma_{NLO} = \int_m d\sigma_{LO} + \int_{m+1} d\sigma_R + \int_m d\sigma_V, \quad (2.1)$$

where the labels  $LO$ ,  $R$  and  $V$  indicate Leading Order, Real-emission and Virtual contributions respectively.

For an automated multipurpose matrix element generator, such as AMEGIC++, the Born and real-emission contributions to the NLO cross section for any process are trivial to calculate. However, automation of the virtual contribution is highly non-trivial. While there are several groups which have made significant progress in this field in the past few years [35–43], it would seem sensible to take advantage of the modularity of the NLO calculation to allow Monte Carlos to utilise existing one-loop programs, rather than requiring each Monte Carlo to compute these internally. This may be achieved through an interface, allowing the one-loop program (OLP) to provide matrix element results for individual phase space points, as required by the Monte Carlo.

The one-loop matrix element is, as previously discussed in Section 1.4, both UV- and IR-divergent. The UV divergences can be removed by renormalisation, and this should be performed by the OLP. However, the IR divergences are required for the cancellation of divergences with the real-emission contribution, and therefore must be regularised and passed to the Monte Carlo along with the finite contribution. These IR divergences may then be cancelled by the Monte Carlo, using a subtraction scheme such as Catani-Seymour dipole subtraction described in Chapter 3.

In order to make a multipurpose Monte Carlo NLO framework as useful and flexible as possible, the ability for the Monte Carlo to utilise the results of many different one-loop codes is obviously advantagous, and thus a general standardised interface is desirable.

From the perspective of the one-loop provider, the ability to interface with an NLO framework, such as the one available in SHERPA, also has obvious advantages. The art of calculating loop matrix elements is far removed from the mechanics of numerical integration and event generation, thus it is sensible to separate these fields of development. SHERPA provides rigorously tested subtraction terms, tree matrix elements, and efficient phase space integration, as well as interfaces with parton distribution functions, and anaysis machinery for producing histograms. The benefits of each one loop provider being spared from producing code for these functions for each individual process studied are clear, not only in the time saved, but also in the reduction of potential bugs in the code. Additionally, ultimately, the one-loop amplitudes thus interfaced with SHERPA may be used for full event simulations, using NLO parton shower machinery such as POWHEG [30–32], and even NLO precision matrix element and parton shower merging [33, 34].

Another obvious beneficiary of the option to combine many different one-loop programs with a single Monte Carlo through a simple standardised interface is the user. Any user with a wish to simulate several different NLO processes would find it far more convenient to use a single Monte Carlo framework with a standardised user interface, than to learn to use several different stand-alone codes.

With these many benefits in mind, an industry-wide standard has been designed to facilitate the easy interface of one-loop codes to Monte Carlos, known as the Binoth Les Houches Accord (BLHA). Using this standard interface, a Monte Carlo user should be easily able to connect the one-loop code, effectively as a black-box, after choosing the required settings for the interface, during the initialisation phase.

**Initialisation Phase** The order-contract phase occurs before run time, and is an opportunity for the Monte Carlo and user to specify what exactly is required of the one-loop program. This includes choosing schemes and settings, as well as specifying parameters. The requested settings are passed to the one-loop program via an order file. The order file contains standard flags to specify the settings and parameters. This file is read by the one-loop program, and a contract file is written. The contract file confirms which of the requested settings are available within the one-loop program, and flags any settings with which there are problems. If all settings are available, then the contract file contains the agreement between the one-loop program and the Monte Carlo, as to exactly what the one-loop program should be calculating. For purely QCD process, the example file may be quite simple:

```
## example order file
CorrectionType          QCD
MatrixElementSquareType CHSUMMED
IRRegularisation        CDR
Power_Alphas            2
ModelFile               model_sm.slha

2 -> 2 1 -1 6 -6
2 -> 2 21 21 6 -6
```

This order file contains all essential settings for the calculation of QCD loop corrections to top pair production at a hadron collider. Setting the order of  $\alpha_s$  to 2 excludes processes with electroweak intermediate states, and the model file contains all necessary parameter settings, in this case specifically the mass of the top. The computed one-loop matrix elements should be colour- and helicity-summed (CHSUMMED), and the conventional dimensional regularisation scheme is used for the regularisation of IR divergences.

**Run-Time Phase** At the start of run-time, the Monte Carlo must first initialise the OLP, using the function

```
OLP_Start(char*,&int)
```

The name of the contract file from the initialisation phase is passed as the first argument, to remind the OLP of the commitments it has made. The second argument allows the OLP to accept the contract, by returning 1, or to indicate a problem with the contract by returning anything else. After this the Monte Carlo may begin integration. The

phase space generator of the Monte Carlo generates a phase space point and this set of momenta is passed to the one-loop program via a calling function. The one-loop program then calculates the one-loop amplitude for that point, according to the settings and parameters agreed in the contract file, and returns this result to the Monte Carlo. The function through which this information is exchanged is

```
OLP_EvalSubProcess(label,momenta,scale*,coupling*,results*)
```

where `label` is an integer which labels the relevant subprocess, as agreed in the initialisation phase; `momenta` is a one-dimensional array containing the components of the four momenta for each particle, along with the particle's mass; `scale` gives the renormalisation scale as a double precision number, or an array of scales as required; `coupling` gives the value of the coupling, or an array of phase space dependent couplings or variables; and `results` is an array which contains the one-loop results.

This basic structure applies to both QCD and electroweak NLO frameworks. However, due to the additional complexity of electroweak calculations, there are extra considerations when providing an interface for electroweak one-loop programs.

## 2.2. Special Considerations for EW Interface

An interface for NLO electroweak calculations will, in general, be more complicated than one for QCD. These specific settings will be discussed briefly here.

### 2.2.1. Regularisation Scheme

In order to parameterise the divergences in the loop amplitude, a regularisation scheme must be chosen. Regularising the divergence allows the singularity to be quantified, enabling cancellation of singular terms. Whichever scheme is chosen, conventions or parameters must be specified before runtime, so that the result can be properly used within the NLO framework. While this is true of both QCD and electroweak calculations, the choice of regularisation scheme is often more complicated in electroweak calculations, as explained below.

**Dimensional Regularisation** For QCD loop calculations the standard choice of scheme is dimensional regularisation. In this scheme, the number of dimensions is extended from

$d = 4$  to  $d = 4 - 2\epsilon$ , where  $\epsilon$  is infinitesimally small. As such, the divergences in the loop amplitude manifest themselves as poles of the form  $\frac{1}{\epsilon}$  and  $\frac{1}{\epsilon^2}$ . This scheme is the default for the standard Binoth Les Houches Accord interface. Using this scheme, the result from the one-loop program is passed to the Monte Carlo as an array of three real numbers. The three numbers correspond to the coefficients of the double and single  $\epsilon$  poles, and the finite piece. A convention which must be agreed on for this scheme is the choice of  $\epsilon$ -dependent prefactor for the result:

$$\mathcal{I}(\{k_j\}, \text{R.S.}, \mu_R^2, \alpha_s(\mu_R^2), \alpha, \dots) = C(\epsilon) \left( \frac{A_2}{\epsilon^2} + \frac{A_1}{\epsilon} + A_0 \right). \quad (2.2)$$

A conventional choice for this prefactor is

$$C(\epsilon) = \frac{(4\pi)^\epsilon}{\Gamma(1-\epsilon)} \left( \frac{\mu^2}{\mu_R^2} \right)^\epsilon = (4\pi)^\epsilon \frac{\Gamma(1+\epsilon)\Gamma(1-\epsilon)^2}{\Gamma(1-2\epsilon)} \left( \frac{\mu^2}{\mu_R^2} \right)^\epsilon + \mathcal{O}(\epsilon^3), \quad (2.3)$$

and this was chosen as the recommended standard for the BLHA, but other choices are also possible, as long as the convention used is made clear by the one-loop program. It should be noted that conventional dimensional regularisation and the 't Hooft-Veltman scheme have the same soft and collinear dimensional treatment, and that results computed in these schemes may be related to those using dimensional reduction. Further discussion of these schemes may be found in references [74–77].

**Mass Regularisation** However, another regularisation scheme is preferred by many of the electroweak one-loop programs. Mass regularisation uses (formally infinitesimally) small masses for the particles involved in the process to regularise the divergences. In this scheme, the divergences appear as large logarithms of the form  $\log\left(\frac{m^2}{Q^2}\right)$ , where  $Q^2$  is a typical scale of the process, and  $Q^2 \gg m^2$ . There are two variations of this scheme: either the photon can be given an unphysical mass, as well as the fermions; or dimensional regularisation can be used for the photon divergences, while mass regularisation is used for the fermions.

For infrared-safe observables, the divergences due to the logarithms exactly cancel with the corresponding contributions from the real-emission part, just as the  $\epsilon$  poles in dimensional regularisation cancel. However, for processes with muons in the final state, an analysis may look at non-infrared-safe observables. This is due to the fact that muons and photons are often measured in different parts of the detector, and therefore it is possible to effectively separate the measurements of a collinear muon and

photon pair. For calculations involving non-collinear-safe observables, the divergences do not completely cancel. This causes problems for dimensionally regularised calculations, where the incomplete cancellation results in remaining physically meaningless  $\epsilon$  poles. For mass regularisation, however, the incomplete cancellation results in terms with logarithms of the muon mass. As the muon mass is a physical quantity, this result is meaningful. As such, mass regularisation is often preferred for the calculation of electroweak one-loop amplitudes.

Using this scheme, the one-loop program passes only one result to the Monte Carlo, and no prefactor is introduced. However, the values of the regulatory masses of all of the particles used in the calculation must be exchanged during initialisation, such that the regulatory masses used in the subtraction terms match those of the one-loop contribution. Note that, at least for infrared-safe observables, the regulatory mass may well be unrelated to the physical mass of the fermions.

### 2.2.2. Renormalisation Scheme

The electroweak renormalisation scheme must be consistent between the OLP and MC, fixing the definitions of couplings and parameters. Without a full transfer of information relevant to these definitions, the MC would be unable to independently reproduce the OLP’s calculation of the Born matrix elements. Therefore, the OLP must specify not just the renormalisation scheme used, but also all parameters needed to calculate the leading order matrix element, including couplings and masses.

Moreover, the interface must allow for as much flexibility as possible in the definition of the renormalisation scheme. Therefore, as well as supporting standard schemes, such as the  $\alpha(0)$  scheme, the  $\alpha(M_Z)$  scheme, or a running coupling with  $\alpha(\mu)$  for some scale  $\mu$ , the interface should also support the possibility of using several different couplings in a single amplitude.

The choice of electroweak renormalisation scheme is not only process dependent, but can also depend to some extent on personal preference. With this in mind, the **OLPdefined** scheme is a flexible setting, allowing the one-loop program (OLP) author to choose a suitable scheme for that particular process. When this scheme is chosen by the user, the one-loop code must provide two couplings:

- $\alpha_{OLP}$ , which is the effective coupling used by the one-loop code in the calculation of the leading order matrix element. It is defined as

$$\alpha_{OLP} = \alpha(0) \left( \frac{|\mathcal{A}_{LO}^{OLP}|^2}{|\mathcal{A}_{LO}^{MC}|^2} \right)^{1/P}, \quad (2.4)$$

where  $P$  is the leading order power of alpha,  $OLP$  labels the LO matrix element calculated by the one-loop code, and  $MC$  labels the LO matrix element calculated by the Monte Carlo.

- $\alpha_{IR}$ , which is the coupling used for the photonic corrections.

With these two effective couplings, the Monte Carlo can reproduce the one-loop code's leading order matrix element calculation (with coupling factor  $\alpha_{OLP}^P$ ), and cancel the poles appropriately (using integrated subtraction terms with overall coupling factor  $\alpha_{IR} \alpha_{OLP}^P$ ).

### 2.2.3. Unstable Massive Particles

The study of electroweak processes necessarily involves dealing with unstable massive particles, in particular the gauge bosons  $Z$ ,  $W^+$  and  $W^-$ . The divergence associated with on-shell propagators necessitate at least partial Dyson resummation. The practical result of this resummation is the introduction of a width into the propagator, which regularises the divergence. The resulting propagator has the general form

$$\frac{1}{p^2 - m^2} \rightarrow \frac{1}{p^2 - m^2 + im\Gamma}, \quad (2.5)$$

where  $\Gamma$  is the width.

However, the resummation procedure involves mixing results from all orders in perturbation theory, and therefore must be treated carefully. For instance, the mixture of perturbative orders means that gauge invariance is no longer guaranteed [78–80]. It is imperative that the schemes used for the resonance treatment are consistent between the Monte Carlo and the one-loop provider.

While there have been many attempts to find suitable width schemes for both leading order [80–93], and NLO [82, 84, 85, 91–93] calculations, one scheme has emerged as the best-defined way to self-consistently treat unstable massive particles in NLO electroweak calculations. The complex mass scheme (CMS), as proposed in reference [94], and further

extended to NLO in reference [95], is not only gauge invariant, but is also valid in all regions of phase space. More details of this scheme may be found in reference [96].

For leading order calculations, the CMS is simply implemented by replacing masses with complex terms  $m \rightarrow \sqrt{m^2 - im\Gamma}$  everywhere. In this way, the complex component to the mass is introduced in the couplings, as well as in the propagators. It should also be noted, that the weak mixing angle also acquires a complex component, as defined by

$$\sin^2(\theta_W) = \frac{M_W}{M_Z} \rightarrow \frac{\sqrt{M_W^2 - iM_W\Gamma_W}}{\sqrt{M_Z^2 - iM_Z\Gamma_Z}}. \quad (2.6)$$

In this case, as masses are simply analytically continued in the complex plane, algebraic relationships, such as the Ward Identities, are preserved. Spurious terms are introduced from the newly complex couplings; however these terms are of order  $\mathcal{O}\left(\frac{\Gamma_W}{M_W}\right)$  relative to the lowest order terms.

Extending the CMS to higher order calculations requires complex counterterms [97]. A procedure for such a complex renormalisation scheme was proposed in reference [95]. Under this formalism, the bare Lagrangian remains unchanged. However, the bare masses are separated into complex renormalised masses, and complex mass counterterms. As such, the perturbative expansion is merely rearranged and the underlying theory remains unchanged.

The CMS is fully supported within the SHERPA framework, and is the default choice for all calculations including unstable particles, and in particular the massive electroweak gauge bosons. The CMS is also the recommended scheme for the interface, although other schemes are supported. In general, though, other schemes may require further information from the OLP, such as the gauge choice for the fixed width scheme. The resonance treatment is set during the initialisation phase, using the flag `ResonanceTreatment`.

## 2.3. Sherpa/Rady Interface

RADY [98] is a program for calculating corrections to the processes  $pp \rightarrow l^+l^-$  and  $pp \rightarrow l\nu$  at hadron colliders. As a standalone program, RADY can provide all necessary components of an NLO calculation, including the Born, virtual and real-emission contributions, as well as dipole subtraction terms for the cancellation of divergences

in the real and virtual contributions. However, it may also be linked to SHERPA via the BLHA interface, such that RADY provides the one-loop matrix element for the subprocesses associated with  $pp \rightarrow l^+l^-$ , and SHERPA performs the rest of the computation.

In this section, some of the details of the SHERPA/RADY interface will be examined.

As discussed in the previous section, the order file describes the specific set-up which the Monte Carlo requires. Some of these settings are determined by the options supported by the Monte Carlo, and some may be choices made by the user. Settings are specified by a flag, which labels the option being set. This is followed by white space, before the choice for the setting is specified. Both the flag and setting are case insensitive. It is also possible to add comments to the order file, following a #-character, which makes both the order files and contract files more human-readable, as well as providing important additional information, as required.

For the SHERPA-RADY interface, a typical order file would look like:

```
## example order.dat
## OLP settings
CorrectionType           EW
MatrixElementSquareType  CHSUMMED
CKMInLoops               Unity
ResonanceTreatment       ComplexMassScheme
# IRRregularisation      DimReg
IRRegularisation         MassReg
IRRegulatorMasses        MU, MC, MD, MS, MB, ME, MMU, MTAU
IRsubtraction            None
EWRenScheme               OLPdefined
Power_Alpha               2
Power_Alphas              0
## numerical input parameters (Model file + additional ew. input)
ModelFile                 model_sm.slha
IN_alpha0                 0.0072973525678993
## processes
2 -> 2 1 -1 13 -13
2 -> 2 2 -2 13 -13
```

The interface currently supports the following options:

- **CorrectionType:**
  - **EWincluded:** QCD and EW corrections
  - **QCDonly** or **QCD:** QCD corrections
  - **EW:** EW corrections (QED + weak)
  - **QED:** photonic corrections
  - **Weak:** genuinely weak corrections
  - **BornOnly:** LO only
- **MatrixElementSquareTypeType:** CHSUMMED
- **CKMInLoops:** Unity
- **ModelFile:** Model file in SLHA format
- **IRRegularisation:**
  - **DimReg**
  - **MassReg:** In this case the flag **IRRegulatorMasses** must also be included, followed by a list of masses to be treated as small
- **IRSubtraction:**
  - **DipoleSubtraction:** the endpoints of the integrated dipole subtraction terms are included in the virtual contribution passed back to the MC. This renders the virtual contribution finite, and removes the dependence on the regularisation scheme. However, it introduces a dependence on the conventions chosen for the dipole subtraction, which may vary significantly in different implementations
  - **None:** virtual corrections only
- **ResonanceTreatment:**
  - **ComplexMassScheme**

- FactorizationScheme
- PoleScheme

- EWRenScheme:
  - alpha0:  $\alpha(0)$  everywhere
  - alphaMZ:  $\alpha(M_Z)$  everywhere
  - alphaGF:  $\alpha_{G_\mu}$  everywhere
  - OLPdefined:  $\alpha(0)$  for photon radiation, i.e. the photonic NLO correction to the cross section scales with  $\alpha(0)\alpha_{G_\mu}^2$ , whereas the genuinely weak NLO correction to the cross section is proportional to  $\alpha_{G_\mu}^3$ . For  $\gamma\gamma$  initial states  $\alpha(0)$  is used everywhere.

In addition to these options, the order file is also used to exchange additional parameters, which are not included in the model file, as they are not part of the SUSY Les Houches Accord (SLHA) [99]. In our case the value of  $\alpha(0)$  is not deduced from  $\alpha(M_Z)$  given in the model file, but is set explicitly via the option `IN_alpha0` in the order file. All other model parameters are passed through a SLHA model file. For this purpose RADY uses the SLHALIB [100]. If an essential option for the OLP is missing from the order file, the default for this option is set and added to the contract file.

For the example order file shown above the corresponding contract file returned by the OLP looks like:

```
correctiontype          qcdonly      | 1      # qqcdew = 1, \
qvirt = 1, qewho = 0, qewhel = 0, qsusy = 0
matrixelementsquaretype chsummed    | 1
ckminloops              unity       | 1
resonancetreatment     complexmasssscheme | 1  \
# qwidth = 1
irregularisation        massreg      | 1      # qregscheme = 1
irregulatormasses       mu, mc, md, ms, mb, me, mmu, mtau | \
1      # Small masses are: MU, MC, MD, MS, MB, ME, MMU, MTAU.
irsSubtraction          none        | 1      # qbrem = 0
ewrenscheme              olpdefined | 1      # qalp = 2, \
```

```

qoptimalscheme = 1
power_alpha          2      | 1
power_alphas         0      | 1
modelfile            model_sm.slha | 1
in_alpha0            0.0072973525678993 | 1
2 -> 2 1 -1 13 -13 | 1 2      # proc_label = 2
2 -> 2 2 -2 13 -13 | 1 1      # proc_label = 1
# parameters used by OLP
# NOTE: EWRenScheme = OLPdefined
# alpha is used for LO q\bar{q} \to l^+l^-, i.e. proc_scheme=1,2,4,
# and alphaIR=alpha0 is used for LO \ga\ga \to l^+l^-,\n
# i.e. proc_scheme=8
OUT_alpha            0.7547514055936910E-02
OUT_alphaIR          0.7297352567899300E-02
OUT_MZ               91.15348059999999
OUT_GZ               2.494266380000000
OUT_MW               80.37450950000000
OUT_GW               2.140241340000000
OUT_CW               0.8817404089366329 , 0.3238080343356995E-03
OUT_SW               0.4717354368914205 , -0.6052431220634457E-03

```

where a \ at the end of the line indicates a line break in the contract file. The answers of the OLP follow after |. If the OLP can provide the order, then it returns a 1, followed by the internal options of the OLP, or any further information in the form of additional comments as necessary. Otherwise, if the option is not supported a -1 is returned. For valid subprocesses the OLP returns 1, plus a process label to identify the subprocess during the run-time phase. In addition to the confirmation of the order, the OLP returns all parameters needed to calculate the LO cross section, for the case when OLP and MC do not support the same options, in particular for the treatment of unstable particles. These parameters are labeled with OUT\_ followed by the name of the parameter. The first number after the parameter is the real part, and, if present, the second is the imaginary part. In our case this additional information was not used, since both SHERPA and RADY support the complex mass scheme. Furthermore, OUT\_alpha and OUT\_alphaIR are returned , these are the couplings used by the OLP for the calculation of the LO cross section and genuinely weak corrections, and the photonic corrections respectively. Note that these couplings are equal in all but the OLPdefined scheme.

The interface described in this section is the first practical implementation of the Binoth Les Houches Accord for connecting electroweak one-loop matrix elements to Monte Carlos. The SHERPA side of this interface is fully generic, and may be used to connect the code for computing one-loop matrix elements for any NLO process, provided that the one-loop code supports the interface.

# Chapter 3.

## Dipole Formalism

### 3.1. Introduction

As discussed in Section 1.4, subtraction methods allow the numerical integration of separately divergent real-emission and virtual one-loop contributions to NLO cross sections, by the introduction of local subtraction terms which cancel the divergences. This results in a calculational structure of the form

$$\sigma_{NLO} = \underbrace{\int_m d\sigma_{LO}}_{\mathcal{B}} + \underbrace{\int_m \left[ d\sigma_V + \int_1 d\sigma_A \right]}_{\mathcal{VI}} + \underbrace{\int_{m+1} [d\sigma_R - d\sigma_A]}_{\mathcal{RS}} . \quad (3.1)$$

The phase space integrals in the above equation are finite, and therefore may be computed using Monte Carlo integration.

In this chapter, one particular subtraction formalism will be reviewed, namely Catani-Seymour dipole subtraction.

The dipole subtraction formalism was originally proposed for QCD corrections in reference [56]. The formalism was extended to massive particles [101], to include polarisation effects [102], and to electromagnetic corrections for photons radiated off charged fermions [54]. In reference [103], further photonic dipoles were added, namely those due to photon splitting, in both the initial and final state.

Catani-Seymour dipole subtraction was the first subtraction formalism to be fully automated, for the case of massless QCD partons. This automation in the matrix element generator AMEGIC++ forms the basis of the implementations of extensions of

this formalism to massive partons, coloured supersymmetric particles, and photonic corrections discussed in the following chapters. Therefore, some details of the massless QCD implementation are also reviewed here.

## 3.2. Observables

An important consideration when discussing any cross section is the definition of the observables in question. To be of any use, observables must be both theoretically and experimentally well defined. In relation to NLO calculations in particular, the observables must be defined appropriately for both the real-emission and leading order phase spaces.

In practice, this means that observables must be defined in such a way that the inclusion of an extra final state soft particle, or the splitting of a final state particle into two collinear particles, does not affect the observable. These are known as infrared-safe observables.

For QCD, this is a well-known problem, fixed by the concept of *jet observables*. Jet observables are defined using some jet algorithm, which clusters collections of final state partons or hadrons into jets. If the jet algorithm is infrared-safe, then the jets it defines may be safely used to form observables. For a recent review of the progress in defining suitable jet algorithms, from both a theoretical and experimental perspective, see reference [104].

For NLO electroweak calculations, there is a similar situation. If a final state photon is collinear with a charged particle, it must be recombined, to form a pseudo-particle, which may be observed. A procedure for this recombination is described in more detail in Section 6.6.

However, in certain circumstances this condition may be relaxed slightly, as it is sometimes possible to separately measure a collinear photon and lepton, for instance in a detector where photons are measured in the calorimeters, and muons are detected in the muon chambers. This possibility requires careful treatment of the analytical integration of the subtraction terms, and is described in detail in reference [103]. This is beyond the scope of this thesis.

### 3.3. Soft and Collinear Singularities

The foundation of the dipole subtraction method is the universality of soft and collinear divergences. The regions of phase space in which real-emission matrix elements diverge involve soft (low energy) or collinear external particles. Thus, if these divergences can be parameterised in a process-independent way, then it becomes possible to construct subtraction terms which can cancel the divergences.

It transpires that the singular behaviour of the real-emission matrix element, due to any particular parton becoming soft or collinear, can effectively be factorised out, resulting in a sum of products of singular factors and Born-configuration matrix elements. The singular factors depend only on the momenta and quantum numbers of three of the partons in the real-emission matrix element, (the emitter, the unresolved and the spectator partons), and the reduced Born-configuration matrix elements consist of a process where the soft or collinear parton has been absorbed by the emitter parton, with the spectator parton absorbing the kick-back, allowing both emitter and spectator partons to remain on-shell. This factorisation is not complete, however, with spin correlations required in the reduced Born matrix element for both QCD and photonic corrections, and additionally colour correlations for QCD.

To illustrate the structure of the singularities, it is instructive to look at the soft and collinear limits.

Following the treatment in reference [56], the limit of one massless parton, with momentum  $p_j$ , becoming soft can be parameterised by

$$p_j^\mu = \lambda q^\mu, \quad \lambda \rightarrow 0. \quad (3.2)$$

Neglecting terms less singular than  $\frac{1}{\lambda^2}$ , and rearranging, leads to a factorised form of the real-emission matrix element, which may be written schematically as

$$|\mathcal{M}_{m+1}|^2 \rightarrow -\frac{1}{\lambda^2} 8\pi\mu^{2\epsilon}\alpha \sum_i \frac{1}{p_i q} \sum_{k \neq i} \frac{p_k p_i}{(p_i + p_k)q} m \langle 1, \dots, m+1 | \mathbf{T}_k \cdot \mathbf{T}_i | 1, \dots, m+1 \rangle_m, \quad (3.3)$$

where  $\mu$  is the associated scale, and  $\mathbf{T}_i$  are the Gell-Mann SU(3) colour matrices.

The collinear limit where two final state particles, with momenta  $p_i$  and  $p_j$ , become collinear, may be parameterised by

$$p_i^\mu = zp^\mu + k_\perp^\mu - \frac{k_\perp^2}{z} \frac{n^\mu}{2p\dot{n}} , \quad p_j^\mu = (1-z)p^\mu - k_\perp^\mu - \frac{k_\perp^2}{1-z} \frac{n^\mu}{2p\dot{n}} , \quad (3.4)$$

where  $0 < z < 1$ ,  $k_\perp$  is the transverse momentum component, and  $n$  is auxiliary light-like vector, where  $k_\perp p = k_\perp n = 0$ .

Neglecting terms less singular than  $\frac{1}{k_\perp^2}$  gives

$$|\mathcal{M}_{m+1}|^2 \rightarrow \frac{1}{p_i p_j} 4\pi\mu^{2\epsilon} \alpha_m \langle 1, \dots, m+1 | \hat{P}_{(ij),i}(z, k_\perp; \epsilon) | 1, \dots, m+1 \rangle_m \quad (3.5)$$

where the kernel  $\hat{P}_{(ij),i}$  is the  $d$ -dimensional Altarelli-Parisi splitting function, a matrix acting on spin indices of emitter particle  $ij$ .

Although neither of these formulae can be used directly as factorised subtraction terms, as they are valid only in the strict limits and there is no clear mechanism for the conservation of momentum, the structures apparent in them clearly show the features an appropriate subtraction term must possess. From equation (3.3), the colour correlations required of the subtraction terms can be seen. Also the explicit dependence on not only the radiated parton and emitter momenta, but also the spectator momentum. From equation (3.5), it can be seen that spin correlations are required, as well as the reassuringly familiar Altarelli-Parisi splitting functions, whose relation to collinear splitting is well known.

### 3.4. Collinear Counterterm

For an NLO calculation involving initial state hadrons (or initial state charged particles for photonic corrections), the situation is slightly more complicated. Firstly, of course, initial state hadrons require the introduction of parton distribution functions (PDFs), describing the density of partons within an incoming hadron. As for the leading order case the partonic cross section is convolved with the relevant parton distribution functions,

$$\sigma(p, \bar{p}) = \sum_{a,b} \int_0^1 d\eta f_a(\eta, \mu_F^2) \int_0^1 d\bar{\eta} \bar{f}_b(\bar{\eta}, \mu_F^2) [\sigma_{ab}^{LO}(\eta p, \bar{\eta} \bar{p}) + \sigma_{ab}^{NLO}(\eta p, \bar{\eta} \bar{p}; \mu_F^2)] , \quad (3.6)$$

where  $a$  and  $b$  label the incoming partons,  $f_a$  and  $\bar{f}_b$  denote the parton distribution functions, and  $\mu_F$  is the factorisation scale.

However, at NLO, another term must be included in the cross section. This term is called the collinear counterterm, labelled  $C$  in the notation of reference [56]. This term contributes in the  $m$ -particle phase space:

$$\sigma_{ab}^{LO}(p, \bar{p}) = \int_m d\sigma_{ab}^B(p, \bar{p}), \quad (3.7)$$

$$\sigma_{ab}^{NLO}(p, \bar{p}; \mu_F^2) = \int_{m+1} d\sigma_{ab}^R(p, \bar{p}) + \int_m d\sigma_{ab}^V(p, \bar{p}) + \int_m d\sigma_{ab}^C(p, \bar{p}; \mu_F^2). \quad (3.8)$$

As can be seen from equation (3.8) the collinear counterterm has a dependence on the factorisation scale. It also depends on the factorisation scheme.

The parton distribution functions also depend on the factorisation scheme and scale, and this dependence cancels with that of the collinear subtraction term, at least to the required perturbative order. However, of course, for proper cancellation of factorisation scale and scheme dependence, the parton distribution functions must have consistent NLO scale evolution.

The collinear counterterm also contains (regularised) divergences, which are required for complete cancellation between the divergences of the virtual and real contributions to the cross section. Adopting the dipole subtraction formulation again, this results in a full NLO  $m$ -particle phase space integration of

$$\sigma_{ab}^{V\mathcal{I}} = \int_m \left[ d\sigma_{ab}^V + \int_1 d\sigma_{ab}^A + d\sigma_{ab}^C \right], \quad (3.9)$$

where  $\int_1 d\sigma_{ab}^A$  is the integrated subtraction term, and only the full sum of the three terms is finite.

For the case of dimensional regularisation, the counterterm takes the form

$$\begin{aligned} d\sigma_{ab}^C(p, \bar{p}; \mu_F^2) &= -\frac{\alpha_s}{2\pi} \frac{1}{\Gamma(1-\epsilon)} \sum_{cd} \int_0^1 dz \int_0^1 d\bar{z} \, d\sigma_{cd}^B(zp, \bar{z}\bar{p}) \\ &\cdot \left\{ \delta_{bd} \delta(1-\bar{z}) \left[ -\frac{1}{\epsilon} \left( \frac{4\pi\mu^2}{\mu_F^2} \right)^\epsilon P^{ac}(z) + K_{F.S.}^{ac}(z) \right] \right. \\ &\left. + \delta_{ac} \delta(1-z) \left[ -\frac{1}{\epsilon} \left( \frac{4\pi\mu^2}{\mu_F^2} \right)^\epsilon P^{bd}(\bar{z}) + K_{F.S.}^{bd}(\bar{z}) \right] \right\}, \quad (3.10) \end{aligned}$$

where the  $P^{ab}$  terms are the familiar Altarelli-Parisi splitting functions, and the  $K_{F.S.}$  terms contain the factorisation scheme dependence. For the popular  $\overline{\text{MS}}$  scheme, all  $K_{F.S.}$  terms are zero.

The collinear counterterm may be absorbed into the integrated dipole terms, for simplification of the resultant expressions.

### 3.5. Dipole Splitting Functions

Having established some idea of the structure of functions which would make suitable subtraction terms in Section 3.3, this section will introduce the subtraction terms in detail.

In the dipole formalism the subtraction terms are based on the dipole splitting functions. Each dipole splitting function depends on only the momenta and quantum numbers of three partons from the real-emission phase space. In Section 3.3, it was seen that both the soft and collinear divergences may be fully described as such, if a sum is taken over all possible combinations of partons.

The basic structure of the splitting functions follows the pattern suggested by the structure of the singularities in Section 3.3. The splitting functions are, in general, each composed of a divergent function of the three relevant momenta, multiplying a spin matrix, and, in the case of QCD corrections, a colour matrix. The splitting function is inserted into the reduced Born-level matrix element.

The key to the universality of these subtraction terms, which allows the completely automated implementation suitable for use with any process, is the process-independence of the splitting functions. While the reduced Born-level matrix elements obviously depend on the process considered, the singular factor is universal, depending only on the quantum numbers and momenta of the three relevant particles. The required Born-level matrix element is easily deduced for each individual subtraction term for any given real-emission process.

In the case of final state splittings with final state spectators, the three partons for each splitting are labelled  $i$  for an emitter,  $j$  for an unresolved parton which is, for the purposes of the subtraction term, assumed to have come from a splitting with the emitter, and  $k$  for a spectator.

For each subtraction term, a mapping must be made between the original  $m + 1$ -particle phase space and the  $m$ -particle phase space; this is required for both the calculation of the Born term in the original subtraction terms, and also the isolation of a one-particle phase space for the analytical integration over the single-parton phase space resulting in the soft and collinear divergences. Using the spectator to absorb the kick-back, it is possible to combine the emitter and unresolved parton momenta to an on-shell emitter. This phase space mapping may be formulated in terms of the labels for the partons by replacing the emitter and unresolved partons  $i$  and  $j$  with a single parton  $\tilde{ij}$ , and the spectator parton  $k$  by  $\tilde{k}$ . The quantum numbers of  $\tilde{k}$  are the same as  $k$ , although its momentum will be altered. The quantum numbers of  $\tilde{ij}$  are completely determined by those of  $i$  and  $j$ , and the momenta are shuffled with the momentum of the spectator  $k$  to place parton  $\tilde{ij}$  on mass shell.

The dipole terms may be usefully separated into four classes, based on whether the emitter and spectator are in the initial or final states respectively. These classes of dipole are, rather unimaginatively, named final-final, final-initial, initial-final, and initial-initial, with the first label denoting the state of the emitter, and the second denoting the state of the spectator. Of course, the unresolved parton,  $j$ , must be in the final state for all dipoles.

The momenta mappings, and the dipole splitting functions, are different for each class of dipole.

The full partonic subtraction term may be written symbolically as

$$\begin{aligned}
d\sigma_{ab}^A &= \sum_{\{m+1\}} d\Phi^{(m+1)}(p_a, p_b, p_1, \dots, p_{m+1}) \frac{1}{S_{\{m+1\}}} \\
&\times \left\{ \sum_{\substack{\text{pairs} \\ i,j}} \sum_{k \neq i,j} \mathcal{D}_{ij,k}(p_a, p_b, p_1, \dots, p_{m+1}) F_J^{(m)}(p_a, p_b, p_1, \dots, \tilde{p}_{ij}, \tilde{p}_k, \dots, p_{m+1}) \right. \\
&+ \sum_{\substack{\text{pairs} \\ i,j}} \left[ \mathcal{D}_{ij}^a(p_a, p_b, p_1, \dots, p_{m+1}) F_J^{(m)}(\tilde{p}_a, p_b, p_1, \dots, \tilde{p}_{ij}, \dots, p_{m+1}) + (a \leftrightarrow b) \right] \\
&+ \sum_{i \neq k} \left[ \mathcal{D}_k^{ai}(p_a, p_b, p_1, \dots, p_{m+1}) F_J^{(m)}(\tilde{p}_a, p_b, p_1, \dots, \tilde{p}_k, \dots, p_{m+1}) + (a \leftrightarrow b) \right] \\
&+ \left. \sum_i \left[ \mathcal{D}^{ai,b}(p_a, p_b, p_1, \dots, p_{m+1}) F_J^{(m)}(\tilde{p}_a, p_b, \tilde{p}_1, \dots, \tilde{p}_{m+1}) + (a \leftrightarrow b) \right] \right\}, \tag{3.11}
\end{aligned}$$

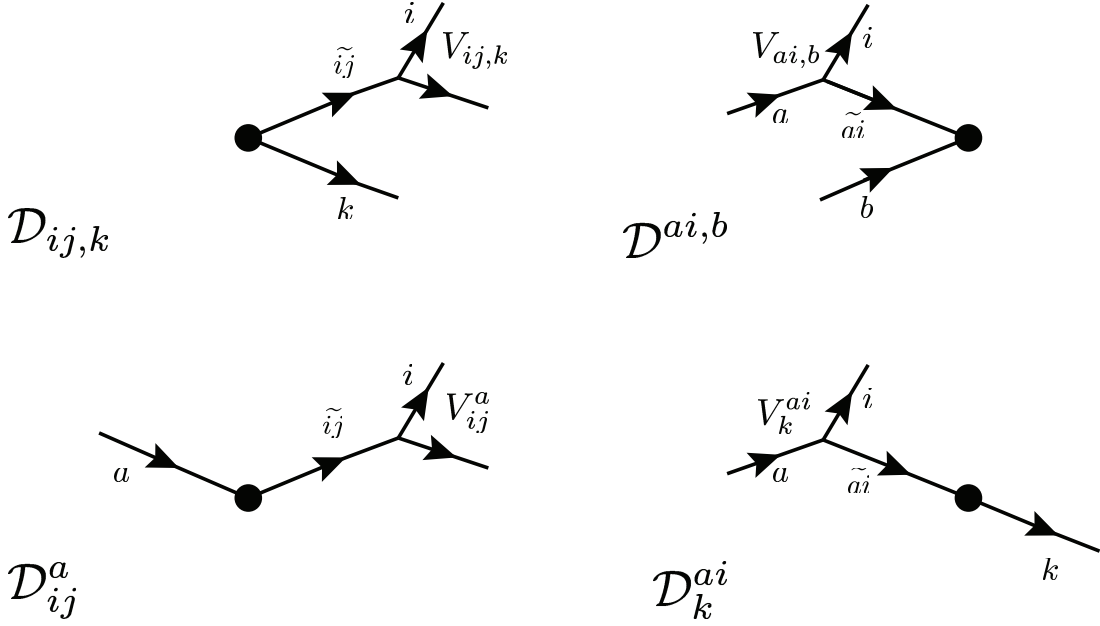


**Figure 3.1.:** Schematic diagrams representing each of the four distinct classes of dipole. The labels  $\mathcal{D}$  represent the subtraction term associated with each splitting, and the labels  $V$  represent each relevant splitting function which forms the basis of the subtraction term. The incoming and outgoing lines represent initial state and final state partons respectively.

where  $\frac{1}{S_{\{m+1\}}}$  is a symmetry factor;  $a$  and  $b$  label the initial state partons;  $\mathcal{D}_{ij,k}$ ,  $\mathcal{D}_{ij}^a$ ,  $\mathcal{D}_k^{ai}$ , and  $\mathcal{D}^{ai,b}$  denote the final-final, final-initial, initial-final, and initial-initial dipole subtraction terms respectively; and the  $F_j^{(m)}$  are the infrared-safe jet observable functions, acting on the reduced  $m$ -particle phase space associated with each dipole. The first sum is over all possible configurations of the  $m+1$  particles,  $d\Phi^{(m+1)}$  denotes the  $m+1$ -particle phase space, and the indices  $i$ ,  $j$ , and  $k$  run over all final state coloured particles (or charged particles, in the case of photonic corrections).

Of course, to produce the complete dipole subtraction term contribution to the cross section, the expression given in equation (3.11) must be augmented by the relevant parton distribution functions for the initial state partons  $a$  and  $b$ , and a sum over all possible combinations of initial state partons must be performed.

### 3.6. Integrated Dipole Terms

The contribution to the cross section from each of the dipole splitting functions must be analytically integrated over a single particle phase space, as explained in Section 1.4.

These integrated dipole terms are then added to the virtual term, cancelling the singularities.

The final structure of the resulting integrated dipole terms (plus the collinear counterterm) may be written schematically as

$$\begin{aligned}
& \sum_{a,b} \int d\eta_1 d\eta_2 f_a(\eta_1, \mu_F^2) f_b(\eta_2, \mu_F^2) \left\{ \int_{m+1} \, d\sigma_{ab}^A(\eta_1 p, \eta_2 \bar{p}) + \int_m \, d\sigma_{ab}^C(\eta_1 p, \eta_2 \bar{p}, \mu_F^2) \right\} \\
&= \sum_{a,b} \int d\eta_1 d\eta_2 f_a(\eta_1, \mu_F^2) f_b(\eta_2, \mu_F^2) \left\{ \int_m \left[ d\sigma_{ab}^B(\eta_1 p, \eta_2 \bar{p}) \times \mathbf{I}(\epsilon) \right] \right. \\
&\quad + \sum_{a'} \int_0^1 dx \int_m \left[ \left( \mathbf{K}^{a,a'}(x) + \mathbf{P}^{a,a'}(x\eta_1 p, x; \mu_F^2) \right) \times d\sigma_{a'b}^B(x\eta_1 p, \eta_2 \bar{p}) \right] \\
&\quad \left. + \sum_{b'} \int_0^1 dx \int_m \left[ \left( \mathbf{K}^{b,b'}(x) + \mathbf{P}^{b,b'}(x\eta_2 \bar{p}, x; \mu_F^2) \right) \times d\sigma_{ab'}^B(\eta_1 p, x\eta_2 \bar{p}) \right] \right\}. \tag{3.12}
\end{aligned}$$

The **I** terms in the above expression contain all of the singular terms, or, in other words, all of the  $\epsilon$ -dependence. The **K** terms result from the convolution over a boost parameter  $x$ , required for dipoles involving initial-state partons, either as spectators or emitters. The **P** terms also have a dependence on the boost parameter, and contain all of the dependence on the factorisation scale,  $\mu_F$ , from the collinear counterterm. The **I**, **K** and **P** terms factorise completely from the reduced cross sections, except for a residual colour correlation. For the case of photonic corrections, the factorisation is complete.

### 3.7. Proliferation of Terms

In order for the Catani-Seymour dipoles to completely cancel the IR divergences associated with the NLO calculation, a sum must be taken over all possible combinations of unresolved parton, emitter and spectator. This will obviously lead to a rapid increase in the number of dipole terms required to cancel the divergences for each subprocess involved in the real-emission as the number of external partons increases. To make matters worse, the reduced matrix element for each dipole term must be calculated separately, as even dipoles mapping to the same leading order reduced process have different kinematics. Therefore, for each real emission phase space point, a matrix element for the leading order process must be calculated for each dipole term.

Subprocess	Diagram	Calculation	Number of Dipoles
$q\bar{q}' \rightarrow Wg$		$2 \times 1$	2
$q\bar{q}' \rightarrow Wgg$		$(3 + 2) \times 2$	10
$q\bar{q}' \rightarrow Wggg$		$(4 + 3 + 2) \times 3$	27
$q\bar{q}' \rightarrow Wgggg$		$(5 + 4 + 3 + 2) \times 4$	56
$q\bar{q}' \rightarrow Wggggg$		$(6 + 5 + 4 + 3 + 2) \times 5$	100

**Table 3.1.:** Number of required dipole subtraction terms for  $W + jets$  NLO corrections. The subprocesses listed are contributions to real-emission corrections for processes with one less light jet (that is,  $q\bar{q}' \rightarrow Wg$  from the table above is a correction to  $pp \rightarrow W$ ). The subprocesses chosen are those with the highest number of dipole terms, for each jet multiplicity.

This is not necessarily a problem when simple, low multiplicity processes are studied: QCD NLO corrections to  $W$ - or  $Z$ -production with no jets, for example, require only a maximum of two dipoles per real-emission subprocess. However, as the multiplicity of the real-emission matrix element increases, and the number of external coloured (or charged in the case of QED) particles increases, the number of required dipoles increases dramatically.

This effect is illustrated in Table 3.1 and 3.2, for subprocesses relevant for the calculation of  $W + jets$  and  $t\bar{t} + jets$  respectively. To take an extreme example, it can be seen from Table 3.1 that the real-emission correction to  $W + 4jets$  involves a single subprocess requiring 100 dipole subtraction terms.

Subprocess	Diagram	Calculation	Number of Dipoles
$gg \rightarrow t\bar{t}g$		$4 \times 3$	12
$gg \rightarrow t\bar{t}gg$		$(5 + 4) \times 4$	36
$gg \rightarrow t\bar{t}ggg$		$(6 + 5 + 4) \times 5$	75
$gg \rightarrow t\bar{t}gggg$		$(7 + 6 + 5 + 4) \times 6$	132

**Table 3.2.:** Number of required dipole subtraction terms for  $t\bar{t} + \text{jets}$  NLO corrections. The subprocesses listed are contributions to real-emission corrections for processes with one less light jet (that is,  $gg \rightarrow t\bar{t}g$  from the table above is a correction to  $pp \rightarrow t\bar{t}$ ). The subprocesses chosen are those with the highest number of dipole terms, for each jet multiplicity.

It should also be noted that as the number of external partons increases, the computational effort required to compute each dipole subtraction term also increases. This is a result of the well-known roughly factorial growth with the number of external legs of the number of Feynman diagrams required to calculate a matrix element. As each of the 100 dipole terms required for the real-emission subprocess  $q\bar{q}' \rightarrow Wggggg$  involves the computation of a  $2 \rightarrow 6$  matrix element, the calculation of these dipole terms is easily the limiting factor of the computation.

It is clear that this proliferation of terms causes the calculation to become impractical at high multiplicities.

### 3.7.1. Phase Space Restriction

A solution to this problem of proliferation of terms is offered by phase space restriction.

Dipole subtraction terms are required in regions of phase space where the real emission matrix element diverges. However, the dipoles as described above also contribute in parts of phase space far from divergences, where the matrix element is finite. This is obviously computationally inefficient, especially in the case of high multiplicity final states.

The problem created by the proliferation of terms can be alleviated by constructing subtraction terms only if necessary. That is, for each phase space point, computing only those dipole terms which are required to cancel divergences in that particular region of phase space. To restrict these dipole contributions to the areas of phase space where they are required, a parameter,  $\alpha$ , was introduced for massless QCD dipoles in references [105, 106].

Following the notation of reference [106], the full subtraction term becomes

$$\begin{aligned}
 d\sigma_{ab}^A &= \sum_{\{m+1\}} d\Phi^{(m+1)}(p_a, p_b, p_1, \dots, p_{m+1}) \frac{1}{S_{\{m+1\}}} \\
 &\times \left\{ \sum_{\substack{\text{pairs} \\ i,j}} \sum_{k \neq i,j} \mathcal{D}_{ij,k}(p_a, p_b, p_1, \dots, p_{m+1}) F_J^{(m)}(p_a, p_b, p_1, \dots, \tilde{p}_{ij}, \tilde{p}_k, \dots, p_{m+1}) \Theta(y_{ij,k} < \alpha y_+) \right. \\
 &+ \sum_{\substack{\text{pairs} \\ i,j}} \left[ \mathcal{D}_{ij}^a(p_a, p_b, p_1, \dots, p_{m+1}) F_J^{(m)}(\tilde{p}_a, p_b, p_1, \dots, \tilde{p}_{ij}, \dots, p_{m+1}) \Theta(1 - x_{ij,a} < \alpha) + (a \leftrightarrow b) \right] \\
 &+ \sum_{i \neq k} \left[ \mathcal{D}_k^{ai}(p_a, p_b, p_1, \dots, p_{m+1}) F_J^{(m)}(\tilde{p}_a, p_b, p_1, \dots, \tilde{p}_k, \dots, p_{m+1}) \Theta(u_i < \alpha) + (a \leftrightarrow b) \right] \\
 &\left. + \sum_i \left[ \mathcal{D}^{ai,b}(p_a, p_b, p_1, \dots, p_{m+1}) F_J^{(m)}(\tilde{p}_a, p_b, \tilde{p}_1, \dots, \tilde{p}_{m+1}) \Theta(\tilde{v}_i < \alpha) + (a \leftrightarrow b) \right] \right\}. \quad (3.13)
 \end{aligned}$$

The  $\alpha$  parameter provides a cut off in a relevant kinematic variable for each dipole, as summarised in Table 3.3. This  $\alpha$  parameter can vary between 0 and 1, with  $\alpha = 1$  equivalent to the original, unrestricted phase space. Of course,  $\alpha$  is an unphysical parameter, so the integrated dipole terms must also have a dependence on the value of  $\alpha$ , such that the full NLO result may be independent of its value. Varying the  $\alpha$  parameter provides a non-trivial test for the correctness of the implementation, see Section 7.1.2.

Dipole Type (emitter-spectator)	Cut Condition	Definition
Final-final	$y_{ij,k} < \alpha y_+$	Eq. (5.12) in [101]
Final-initial	$1 - x_{ij,a} < \alpha$	Eq. (5.42) in [101]
Initial-final	$\tilde{z}_i < \alpha$	Eq. (5.74) in [101]
Initial-initial	$\tilde{v}_i < \alpha$	after Eq. (5.151) in [56]

**Table 3.3.:** Kinematic cuts to restrict dipole phase space, and definitions of the corresponding variables in references [56, 101]. The cuts are sorted by the dipole type, determined by whether the spectator and emitter are in the initial or final states. The cuts given are for massive dipoles, but the massless case is trivially found by setting masses to zero in the definitions referenced above.

Of course, the alpha parameter does create sharp edges in the phase space, where the dipole terms are cut off, and thus the phase space integration, and its optimisation, are more complicated. This, however, has had little effect on the convergence of the integrals tested in SHERPA, and is therefore not worth considering when choosing a value of  $\alpha$  for a particular process.

A consideration which should not be neglected, though, is the size of the resultant subtracted real-emission cross section. As  $\alpha$  decreases, the subtraction terms are calculated over less of the phase space. This is obviously beneficial in the finite regions. However, if  $\alpha$  is set too small, then a significant portion of the divergent peak may be unsubtracted. This results in a large (positive) value for the subtracted real-emission contribution. Obviously, the virtual contribution, consisting of the one-loop term and integrated subtraction terms, becomes large and negative to cancel this large positive contribution. However, this results again in the numerically undesirable subtraction of two large numbers. This potential problem with very small values of  $\alpha$  is discussed further, and illustrated with results, in Section 7.1.2.

It is worth noting that in addition to this *algorithmic* phase space cut, there is typically also a *technical* cut, which in this implementation is chosen in the same kinematical variables. While the former serves to alleviate the calculational burden, the latter protects the double-precision numerics against instabilities. Practically speaking, if the phase space distance between two particles is smaller than this  $\alpha_{\text{tech.}}$ , the real and subtraction term may reasonably be supposed to be exactly identical and do not need to be evaluated at all. Again, the results should be independent of this  $\alpha_{\text{tech.}}$ , see Section 7.1.1.

## 3.8. General Structure of the Calculation

From a computational point of view, straight NLO calculations using dipole subtraction may be split into two completely separate parts. Of course, these two parts are only physically meaningful when combined, but for all intents and purposes their Monte Carlo integrations may be considered separately. The first part, labelled  $\mathcal{RS}$ , are the terms which live on the  $m + 1$ -particle phase space, namely the *Real-emission* contribution, and the dipole *Subtraction* terms.

The second part is the NLO correction which lives on the same phase space as the leading order term. This part is labelled  $\mathcal{VI}$ , and consists of the *Virtual* term and the *Integrated* dipole terms. It should be understood that the integrated dipole terms have also absorbed the collinear counterterm (see Section 3.4), for simplification of the notation.

The  $\mathcal{RS}$  part, is computationally relatively straightforward, from a Monte Carlo point of view. An  $m + 1$ -particle phase space point is generated. The real-emission matrix element is calculated using these momenta. For each of the subtraction terms, the  $m + 1$  momenta are mapped onto  $m$  momenta, following the prescriptions detailed in references [56, 101]. The subtraction terms are calculated, using the Born matrix elements computed with these mapped momenta. The subtlety in this procedure is the implementation of cuts: while cuts (or histogram binnings) are applied to the  $m + 1$ -particle phase space for the real-emission term, they are applied to the reduced mapped  $m$ -particle phase space for each of the subtraction terms, as shown schematically by the  $F_j^{(m)}$  functions in equation (3.11). This can result in so-called *missed binning*, where at least some of the subtraction terms contribute to different histogram bins from the associated real-emission term. It is clear that this is only a problem if the phase space point in question is close to a divergence cancelled by the mis-binned subtraction term. However, as the phase space point approaches the divergence, the chance of missed binning is reduced. This is ensured by the necessary introduction of infra-red safe observables, as described in Section 3.2. For infra-red safe observables two collinear partons are clustered to produce a pseudo-particle, referred to as a *jet* in QCD. Thus the mapped momenta of the subtraction term, where the emitter and emitted partons are combined, is closely related to the real-emission momenta, after the use of an infra-red safe jet algorithm, for phase space points close to the divergence. For the case of photonic corrections, a similar procedure may be applied, as detailed in Section 6.6.

The  $\mathcal{VI}$  part of the NLO calculation benefits from some more detailed consideration before implementation. A relatively simple reorganisation of the contributing terms, as detailed in reference [66], can result in far more efficient code.

As stated in Section 3.6, the integrated dipole terms may be written schematically as

$$\begin{aligned}
& \sum_{a,b} \int d\eta_1 d\eta_2 f_a(\eta_1, \mu_F^2) f_b(\eta_2, \mu_F^2) \left\{ \int_{m+1} \mathrm{d}\sigma_{ab}^A(\eta_1 p, \eta_2 \bar{p}) + \int_m \mathrm{d}\sigma_{ab}^C(\eta_1 p, \eta_2 \bar{p}, \mu_F^2) \right\} \\
&= \sum_{a,b} \int d\eta_1 d\eta_2 f_a(\eta_1, \mu_F^2) f_b(\eta_2, \mu_F^2) \left\{ \int_m [\mathrm{d}\sigma_{ab}^B(\eta_1 p, \eta_2 \bar{p}) \times \mathbf{I}(\epsilon)] \right. \\
&\quad + \sum_{a'} \int_0^1 dx \int_m \left[ (\mathbf{K}^{a,a'}(x) + \mathbf{P}^{a,a'}(x\eta_1 p, x; \mu_F^2)) \times \mathrm{d}\sigma_{a'b}^B(x\eta_1 p, \eta_2 \bar{p}) \right] \\
&\quad \left. + \sum_{b'} \int_0^1 dx \int_m \left[ (\mathbf{K}^{b,b'}(x) + \mathbf{P}^{b,b'}(x\eta_2 \bar{p}, x; \mu_F^2)) \times \mathrm{d}\sigma_{ab'}^B(\eta_1 p, x\eta_2 \bar{p}) \right] \right\}. \tag{3.14}
\end{aligned}$$

Following the construction of reference [66], the calculation of these terms may be rearranged for optimisation.

The  $x$ -dependence of the  $\mathbf{K}$  and  $\mathbf{P}$  terms may be expressed as distributions of the form

$$(g(x))_+ + \delta(1-x)h(x) + k(x), \tag{3.15}$$

where  $h$  and  $k$  are regular functions of  $x$ , and the ‘+’-distribution is defined by its action on a generic test function

$$\int_0^1 dx a(x) (g(x))_+ = \int_0^1 dx [a(x) - a(1)] g(x). \tag{3.16}$$

In this notation, the factorisation scale dependence has been suppressed to keep expressions succinct.

The schematic form for the integrated dipole term becomes

$$\begin{aligned}
& \sum_{a,b} \int d\eta_1 d\eta_2 f_a(\eta_1, \mu_F^2) f_b(\eta_2, \mu_F^2) \\
& \int_m \left\{ \mathbf{I}(\epsilon) d\sigma_{ab}^B(\eta_1 p, \eta_2 \bar{p}) \right. \\
& + \sum_{a'} \left[ \int_0^1 dx \left( g^{a,a'}(x) [d\sigma_{a'b}^B(x\eta_1 p, \eta_2 \bar{p}) - d\sigma_{a'b}^B(\eta_1 p, \eta_2 \bar{p})] + k^{a,a'}(x) d\sigma_{a'b}^B(x\eta_1 p, \eta_2 \bar{p}) \right) \right. \\
& \quad \left. \left. + h^{a,a'}(1) d\sigma_{a'b}^B(\eta_1 p, \eta_2 \bar{p}) \right] \right. \\
& + \sum_{b'} \left[ \int_0^1 dx \left( g^{b,b'}(x) [d\sigma_{ab'}^B(\eta_1 p, x\eta_2 \bar{p}) - d\sigma_{ab'}^B(\eta_1 p, \eta_2 \bar{p})] + k^{b,b'}(x) d\sigma_{ab'}^B(\eta_1 p, x\eta_2 \bar{p}) \right) \right. \\
& \quad \left. \left. + h^{b,b'}(1) d\sigma_{ab'}^B(\eta_1 p, \eta_2 \bar{p}) \right] \right\}, \tag{3.17}
\end{aligned}$$

where the ‘+’ distributions have been expanded into a practically implementable form.

It may be seen from the expression above, that for each partonic configuration (labelled by the sums over  $a$ ,  $b$ ,  $a'$  and  $b'$ ), and for each phase space point (represented by the integrals over  $\eta_1$ ,  $\eta_2$  and the  $m$ -particle phase space), the reduced Born cross section must be evaluated more than once. That is, each reduced Born cross section must be evaluated for both the original and the  $x$ -boosted momenta. As the number of external legs increases, the evaluation of the matrix elements becomes computationally expensive. This is due to the typically factorial growth in the number of Feynman diagrams associated with a given process. Therefore, for an optimal implementation, the calculation should be rearranged such that the Born cross section is only calculated once.

This may be accomplished by changing the integration variable for the terms with the  $x$ -boosted momenta, such that  $\eta'/x$  is substituted for the integration variable  $\eta$ . Relabelling  $\eta' \rightarrow \eta$ , and rearranging the resulting terms allows factorisation of the Born

cross section. The expression for the integrated dipole terms now has the form

$$\begin{aligned}
 & \sum_{a,b} \int d\eta_1 d\eta_2 f_a(\eta_1, \mu_F^2) f_b(\eta_2, \mu_F^2) \int_m d\sigma_{ab}^B(\eta_1 p, \eta_2 \bar{p}) \times \left\{ \mathbf{I}(\epsilon) \right. \\
 & + \sum_{a'} \int_{\eta_1}^1 dx \left[ \frac{f_{a'}(\eta_1/x, \mu_F^2)}{x f_a(\eta_1, \mu_F^2)} \left( g^{a',a}(x) + k^{a',a}(x) \right) - \frac{f_{a'}(\eta_1, \mu_F^2)}{f_a(\eta_1, \mu_F^2)} g^{a',a}(x) \right] \\
 & + \sum_{a'} \frac{f_{a'}(\eta_1, \mu_F^2)}{f_a(\eta_1, \mu_F^2)} \left( h^{a',a} - G^{a',a}(\eta_1) \right) \\
 & + \sum_{b'} \int_{\eta_2}^1 dx \left[ \frac{f_{b'}(\eta_2/x, \mu_F^2)}{x f_b(\eta_2, \mu_F^2)} \left( g^{b',b}(x) + k^{b',b}(x) \right) - \frac{f_{b'}(\eta_2, \mu_F^2)}{f_b(\eta_2, \mu_F^2)} g^{b',b}(x) \right] \\
 & \left. + \sum_{b'} \frac{f_{b'}(\eta_2, \mu_F^2)}{f_b(\eta_2, \mu_F^2)} \left( h^{b',b} - G^{b',b}(\eta_2) \right) \right\}, \tag{3.18}
 \end{aligned}$$

where  $G^{a,b}(\eta) = \int_0^\eta dx g^{a,b}(x)$  are analytically calculated.

### 3.9. Summary

In this chapter the Catani-Seymour dipole subtraction formalism has been reviewed. Also extensions and improvements to the basic theory designed to increase efficiency have been covered, including phase space restriction to reduce the number of dipoles calculated for each real-emission phase space point, and a reorganisation of the integrated dipole terms to factorise out the Born matrix element.

# Chapter 4.

## Massive QCD Dipoles

Quarks are massive particles. However, at the typical energies explored by particle collider experiments, it is often an extremely good approximation to treat at least some of them as massless. This is certainly true of the up and down quarks, with masses of only a few MeV; and at modern colliders the same may generally be said of strange and charm quarks, with masses of order 100 MeV and 1 GeV respectively. The bottom quark is an interesting case which falls on the borderline. With a mass of approximately 5 GeV, it is, in some cases, convenient to treat it as massless, while for some processes the mass effects are sufficiently large that an accurate treatment requires a massive bottom quark. This ambiguous status necessarily leads to the existence of different schemes for the treatment of the bottom quark, commonly known as 4- and 5-flavour schemes, referring to the total number of quarks involved in the PDF evolution. A summary of the different schemes, and a comparison of results using 4- and 5-flavour schemes is given in reference [107].

One case which is not ambiguous, however, is the top quark. With a mass of approximately 175 GeV, it is not only about 100,000 times more massive than the lightest quarks, it is also the most massive of all Standard Model particles.<sup>1</sup> As such, the top quark must always be treated as massive.

Top physics is also an important area for investigation at the LHC. With the higher energies and luminosity available there, tops will be produced in higher numbers, and studied with greater accuracy than ever before. Precision measurements of top

---

<sup>1</sup>It should be noted that the definition of a quark mass is not unambiguous. Any quoted value for a quark mass must be accompanied by a description of the theoretical framework used to define it, in order to be meaningful. However, the values quoted here are order of magnitude estimates for the purpose of illustration, and therefore, at this level of (im)precision, scheme dependence is effectively irrelevant.

quarks will provide valuable insight into the interactions of quarks: top quarks are the only quarks that decay before hadronisation, allowing measurements of “free quark” properties, such as direct measurements of the CKM matrix element  $V_{tb}$ , or spin correlations of decay products, which are not possible with the light quarks.

The study of the top sector is also important in the search for new physics. Precision tests of Standard Model predictions may indicate where to find new physics, or may constrain or rule out BSM models.

However, for theoretical predictions to match the experimental precision expected from the LHC measurements, NLO corrections must be taken into account. Therefore, to be truly flexible, an NLO framework must allow for the possibility of massive quarks in the final state.

Moreover, it is not just heavy Standard Model quarks which would benefit from a framework for treating massive particles at NLO, but also any BSM theories with additional coloured particles. An example of such a theory is discussed in Chapter 5.

The structure of divergences in NLO cross sections, as discussed in Section 3.3, is universal for massless QCD, allowing the construction of process-independent subtraction terms.

However the universality of the divergent structure is not limited to the massless theory [108], and the dipole subtraction terms may be extended to include the dipoles relevant for massive final state partons [101].

Much of the theory behind the derivation of these dipole terms is identical to the massless case described in Chapter 3; due to the finite parton mass, the kinematics of the dipole terms and the necessary analytic integrals are more complicated, but the underlying philosophy of the subtraction formalism is the same.

## 4.1. Quasi-collinear Limit

In direct analogy with the massless case, there are the infrared poles, of the form  $\frac{1}{\epsilon}$  when using dimensional regularisation, which must cancel for a finite calculation. However, in the massive case, these poles are created only in the soft limit, while in the massless case poles also arise from the limit in which final state particles become collinear. When the partons are given a finite mass, the collinear singularity is screened, and these previously

singular terms become terms proportional to  $\log \frac{M^2}{Q^2}$ , where  $M$  is the mass of the parton, and  $Q$  is a typical scale of the process. These logarithms in the real contribution are compensated by similar terms in the virtual contribution.

It is clear that these terms are finite as  $\epsilon \rightarrow 0$ , but they may still cause numerical problems for the calculation: for processes with  $Q^2 \gg M^2$ , these logarithms become large. Thus the calculation relies on the subtraction of two large numbers (given by the real and virtual contributions respectively), which is a numerically unstable procedure.

Therefore, ideally, our subtraction terms should not only cancel the divergences appearing as  $\epsilon$ -poles in the virtual contribution, but also compensate the potentially large logarithms of the form  $\log \frac{M^2}{Q^2}$ , resulting from the quasi-collinear limit.

To achieve this aim, subtraction terms have been derived in reference [101] which have the property

$$\lim_{M \rightarrow 0} \int_{m+1} \left[ (\mathrm{d}\sigma^R(M))_{\epsilon=0} - (\mathrm{d}\sigma^A(M))_{\epsilon=0} \right] = \int_{m+1} \left[ (\mathrm{d}\sigma^R(M=0))_{\epsilon=0} - (\mathrm{d}\sigma^A(M=0))_{\epsilon=0} \right]. \quad (4.1)$$

This condition ensures that both the  $\mathcal{RS}$  contribution (from the  $m+1$ -particle phase space), and the  $\mathcal{VI}$  contribution (from the  $m$ -particle phase space) are separately finite in the massless limit. This smooth behaviour in the limit of  $\frac{M}{Q} \rightarrow 0$  allows stable numerical calculation of the cross section in all kinematical regimes.

## 4.2. Organisation of the Calculation

The dipole terms involving massive partons are very similar in structure to those for massless partons.

The main differences are seen in the integrated dipole terms. There are two structural differences which require careful treatment, particularly in the reorganisation of terms, in analogy with Section 3.8, to optimise the calculation.

Firstly, the extension to finite parton masses results in terms with an additional dependence on a kinematic variable. This variable appears in the  $\mathbf{K}$ -terms of the dipoles, which are involved in the additional convolution over a longitudinal momentum

parameter  $x$ . Thus, when changing integration variables during optimisation, care must be taken for the correct treatment of this variable.

The other main difference is due to the kinematical restraints placed on the integration limits, particularly for the case of a gluon splitting to a massive quark-antiquark pair with an initial state spectator. Once again, the affected terms belong to the  $\mathbf{K}$ -terms, and the complications arise in the  $x$ -convolution. The modified endpoint of this integration introduces terms of the form

$$\left(g^{x_+^F}(x)\right)_{x_+^F} + \delta(x_+^F - x)h^{x_+^F}, \quad (4.2)$$

where the endpoint of the  $x$  integration is denoted as  $x_+$ , and is defined as

$$x_+ = 1 - \frac{4m_F^2}{2p_a \tilde{p}_{ij}}. \quad (4.3)$$

The  $h^{x_+^F}$  term is, in analogy with the massless case, a constant in  $x$ . The distribution  $\left(g^{x_+^F}(x)\right)_{x_+^F}$  is defined by its action on a test function, in analogy to equation (3.16),

$$\int_0^1 dx a(x) (g(x, \hat{s}(\eta)))_{x_+} = \int_0^1 dx \Theta(x_+ - x) [a(x) - a(x_+)] g(x, \hat{s}(\eta)). \quad (4.4)$$

A detailed account of the treatment of these complications in the reorganisation of the integrated dipole terms is given in Appendix A.5. The reorganisation of terms results

in a final structure to the calculation of the form

$$\begin{aligned}
& \sum_{a,b} \int d\eta_1 d\eta_2 f_a(\eta_1, \mu_F^2) f_b(\eta_2, \mu_F^2) \int_m d\sigma_{ab}^B(\eta_1 p, \eta_2 \bar{p}) \times \left\{ \mathbf{I}(\epsilon) \right. \\
& + \sum_{a'} \int_{\eta_1}^1 dx \left[ \frac{f_{a'}(\eta_1/x, \mu_F^2)}{x f_a(\eta_1, \mu_F^2)} \left( g^{a',a}(x, \hat{s}(\eta_1/x)) + k^{a',a}(x) + \delta^{a',a} \sum_F^{N_F} g^{x_+^F}(x) \right) \right. \\
& \left. - \frac{f_{a'}(\eta_1, \mu_F^2)}{f_a(\eta_1, \mu_F^2)} \left( g^{a',a}(x, \hat{s}(\eta_1)) \right) \right] \\
& + \sum_{a'} \frac{f_{a'}(\eta_1, \mu_F^2)}{f_a(\eta_1, \mu_F^2)} \left( h^{a',a} - G^{a',a}(\eta_1) \right) \\
& - \sum_F^{N_F} \Theta(x_+^F - \eta_1) \frac{f_a(\eta_1/x_+^F, \mu_F^2)}{f_a(\eta_1, \mu_F^2)} \left[ \int_{\eta_1}^1 dx g^{x_+^F}(x) \Theta(x_+^F - x) + G^{x_+^F}(\eta_1) - h^{x_+^F} \right] \\
& \left. + \langle 1 \rightarrow 2, a \rightarrow b, a' \rightarrow b' \rangle \right\}, \tag{4.5}
\end{aligned}$$

where  $G(\eta) = \int_0^\eta dx g(x, \hat{s}(\eta/x))$  and  $G^{x_+^F}(\eta) = \int_0^\eta dx g^{x_+^F}(x, \hat{s}(\eta/x_+^F)) \Theta(x_+^F - x)$ , and  $G(\eta)$  and  $G^{x_+^F}(\eta)$  are calculated analytically.

### 4.3. Phase Space Restriction

The modifications to the massive Catani-Seymour dipoles due to the restriction of the phase space described in Section 3.7.1 are detailed in references [69, 109–111], and the modifications for the necessary massless dipoles are detailed in references [105, 106].

Unlike the massless dipole implementation, the phase space restriction for massive processes is implemented in SHERPA separately for each dipole type, as shown in Table 3.3, which allows the four different  $\alpha$  parameters to be varied independently.

# Chapter 5.

## Supersymmetry: Dipoles and On-Shell Subtraction

The introduction of dipoles for massive final states, as discussed in Chapter 4, opens the door for the NLO treatment of additional coloured particles in Beyond the Standard Model theories. Any BSM coloured states must not only be massive, their masses must be so large that their discovery was beyond the experimental reach of previous colliders.

An example of such a BSM theory with additional massive coloured states is supersymmetry. In this chapter the implementation of Catani-Seymour dipole subtraction is extended to include this BSM example. For this example, massive coloured scalar particles, namely squarks, must be considered. With the inclusion of the scalar dipole functions, the implementation may now be trivially extended to BSM theories with any coloured spin-0 scalars, and spin- $\frac{1}{2}$  fermions.

### 5.1. Introduction to Supersymmetry

One popular possible extension to the Standard Model is supersymmetry, commonly abbreviated to SUSY. In supersymmetric theories, fermionic and bosonic degrees of freedom are related. A practical consequence of this is the introduction of so-called *superpartners* for Standard Model fields: new bosons and fermions, with identical mass and quantum numbers to their SM counterparts, only differing in spin by 1/2.

Supersymmetry has been well studied over the past 40 years, and there is extensive literature available on the subject. In particular, there are several reviews

providing pedagogical introductions, and highlighting key aspects of the theory, such as references [112–117].

Supersymmetry is a natural extension to the Standard Model. It is already known that nature respects a variety of symmetries, and as such physical fundamental theories must be invariant under Poincaré transformations. The Poincaré group includes both Lorentz transformations (rotations and boosts) and translations. The Poincaré group can be extended trivially, through the direct product with another internal symmetry of a theory, such as a gauge symmetry. However, as a result of the Coleman-Mandula no-go theorem [118] and the Haag-Lopuszanski-Sohnius theorem [119], the only *non-trivial* extension to the Poincaré symmetry group consistent with interacting relativistic quantum field theories involve *fermionic* generators, which change the spin of a state by 1/2. This extension of the symmetry group is the theoretical basis of supersymmetry. Given that we are already aware of the important role that symmetries play in nature, and in particular the Poincaré group, it would perhaps be natural and intuitive for the extension to the Standard Model to arise as a direct consequence of the *only possible* non-trivial extension to the Poincaré group.

Moreover, there are several theoretically pleasing practical qualities to SUSY. Firstly, supersymmetry provides an elegant solution to the hierarchy problem [120–124]. The hierarchy problem arises from the self-energy corrections to the Higgs boson mass: without some arguably unnatural fine-tuning, Standard Model quantum corrections cause the mass of the Higgs to increase to such a scale that the consistency of the theory is compromised. To exasperate the situation further, any as yet unknown high-mass Beyond the Standard Model particles which might exist above the current experimental reach, would contribute to this problem, whether or not they couple directly to the Higgs. However, the loop corrections due to fermions and bosons contribute with opposite signs, therefore, with the inclusion of superpartners to all Standard Model fields, the corrections naturally cancel to all orders [125–130].

Supersymmetry also provides a candidate for dark matter, in the case where R-parity is conserved. In this case, the lightest supersymmetric particle is stable, having no possible decay modes, and thus may account for currently unexplained cosmological observations of an apparently new, massive, weakly interacting substance, referred to as cold dark matter [131, 132].

Another enticing characteristic of supersymmetric theories is the possibility of unifying the fundamental forces [133]. Gravity may be incorporated into SUSY theories,

resulting in so-called supergravity theory [134]. SUSY is also a necessary component of many string theories.

However, there is one problem with supersymmetric theories: there is absolutely no experimental evidence to support them. If there were indeed superpartners to Standard Model fields, existing with the same masses and interacting with the same couplings, they would have been discovered many years ago. Thus, if supersymmetry exists, it must be broken, such that the masses of the superpartners are considerably higher than their Standard Model counterparts, and lie outwith the experimental reach of previous colliders. However, it should be noted that the masses of the supersymmetric particles must not be too large if they are to solve the hierarchy problem, and thus supersymmetry, if it exists, should be detectable at the LHC.

## 5.2. QCD Dipoles for SUSY Processes

In the minimal supersymmetric Standard Model, the QCD sector is extended to include the superpartners of quarks and gluons, namely squarks and gluinos. As discussed above, the masses of squarks and gluinos must be considerably higher than those of Standard Model particles, in order to be consistent with experimental data. The practical consequence of these higher masses, in relation to dipole subtraction, is that it is sufficient to include dipoles for final state squarks and gluinos emitting a gluon, and to neglect dipoles associated with squark or gluino production from a gluon splitting.

The dipoles for emitters belonging to the Standard Model are unchanged by the inclusion of SUSY particles, as the dipoles depend on neither the flavour nor the spin of the spectator particle.

The colour charges associated with the SUSY particles are the same as their Standard Model partners, but the spin of the superpartners is reduced by  $1/2$ , resulting in scalar squarks, and majorana fermion gluinos.

As such, the kinematics for gluino dipoles are identical to those for massive quarks and the dipoles are trivially related, with only the colour factor  $C_F$  replaced with  $C_A$ .

The dipoles for squarks require kinematics for scalar emitters, and the dipole terms are listed in reference [101].

### 5.2.1. Phase space restriction

The extension of the dipoles to include the phase restriction parameter  $\alpha$ , as described in Section 3.7.1, is again trivial for the case of gluinos, where the dipoles are related to the massive quark dipoles by a simple change of colour factor.

In the case of squarks, the modifications to the integrated dipole terms due to the inclusion of the restriction  $\alpha$  have been derived in Appendix B.

## 5.3. On-Shell Subtraction

For NLO calculations involving SUSY particles, there may be additional complications. For many processes, as well as the IR divergences cancelled by the Catani-Seymour dipoles, extra divergences appear in the real emission contribution due to on-shell intermediate states. To take a specific example, this may be seen clearly in  $2 \rightarrow 2$  squark-gluino production at a hadron collider. At leading order, SUSY intermediate states are only seen in the t-channel. However, when an extra QCD parton is added at NLO, there are contributions from diagrams with intermediate massive SUSY states which may go on-shell. In the following, these diagrams shall be called the *resonant diagrams*, and the diagrams without intermediate SUSY states which may go on-shell shall be called the *non-resonant diagrams*. From the resonant diagrams there is a divergence when the propagator of the intermediate state goes on-shell. It is well known that this divergence is simply regularised by introducing a finite width into the propagator. With this addition,

$$\frac{1}{(p^2 - m^2)} \rightarrow \frac{1}{(p^2 - m^2) + im\Gamma} , \quad (5.1)$$

the matrix element no longer diverges.

However, there is another, more serious, complication. The contribution to the cross section from the resonant diagrams when the intermediate state is on-shell, is also counted as a contribution to a leading order  $2 \rightarrow 2$  process. In the above example, when, for instance, there is an intermediate gluino (and the gluino mass is greater than the squark mass), the contribution is also included as part of the gluino-pair production cross section, with a leading order decay to a squark and a quark. Thus, if these calculations are performed naively, this will result in double counting.

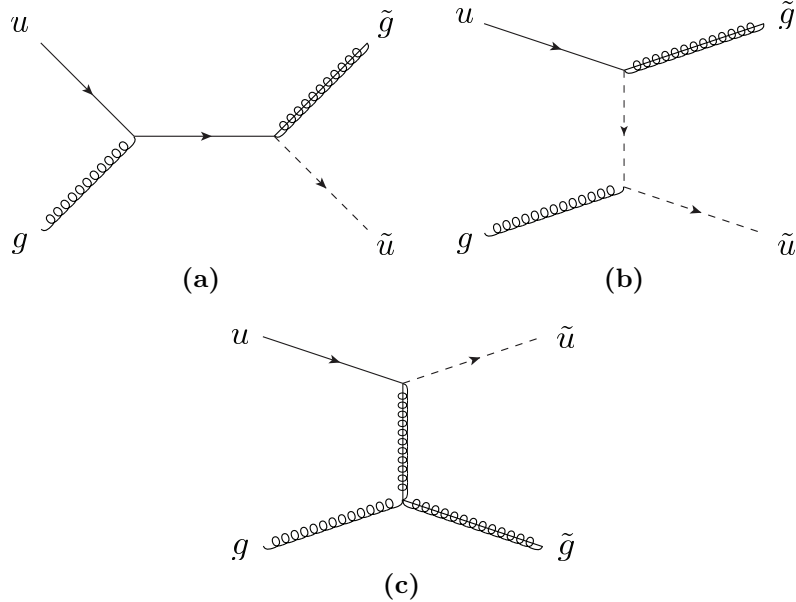


**Figure 5.1.:** Feynman diagrams for LO contributions to squark-gluino production.

There have been several suggestions of how to tackle this problem [111, 135–138]. One possibility is simply to completely remove diagrams with a resonant intermediate state from the NLO real-emission amplitude. However, this technique results in the loss of the interference terms, between the resonant diagrams and the non-resonant diagrams. This may be seen schematically, by separating the real-emission amplitude into two contributions,

$$\mathcal{A}_{n+1} = \mathcal{A}_{n+1}^N + \mathcal{A}_{n+1}^R, \quad (5.2)$$

where the label  $N$  denotes the contribution due to non-resonant diagrams, and  $R$  labels the resonant diagrams. Thus the real-emission contribution to the cross section takes the form,

$$|\mathcal{A}_{n+1}|^2 = \underbrace{|\mathcal{A}_{n+1}^N|^2}_{\mathcal{N}} + \underbrace{2\Re \{ \mathcal{A}_{n+1}^N (\mathcal{A}_{n+1}^R)^* \}}_{\mathcal{I}} + \underbrace{|\mathcal{A}_{n+1}^R|^2}_{\mathcal{R}}$$

If the resonant diagrams are removed completely from equation (5.2), then only the first term on the right hand side of equation (5.3) survives. However, it is only the  $\mathcal{R}$  which is double counted, so it would be better to remove only this term.

Another possibility is to construct a local subtraction term. This technique was developed in PROSPINO [139, 140], and since used for various other pro-

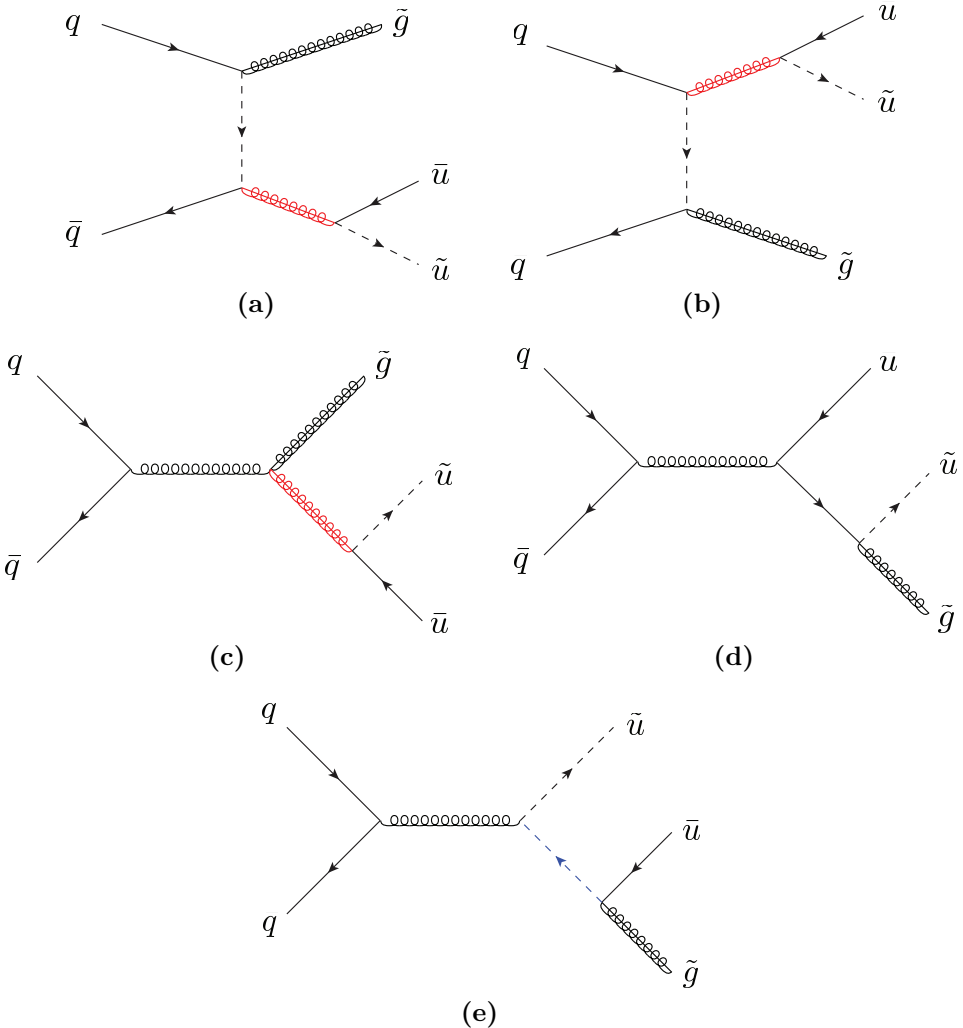


**Figure 5.2.:** Feynman diagrams for NLO real-emission contributions to squark-gluino production. The propagators requiring on-shell subtraction depend on the SUSY scenario under consideration: highlighted in red are those propagators which may go on-shell, if gluinos are more massive than squarks; highlighted in blue is the propagator which may go on-shell if squarks are heavier than gluinos.

cesses [135–138, 141–144]. Ideally, this counterterm should be gauge invariant, so it is not possible to simply subtract  $\mathcal{R}$ . However,  $\mathcal{R} - \mathcal{R}_s$ , where  $\mathcal{R}_s$  is the on-shell subtraction term, should be as close to zero as possible.

This can be achieved by reshuffling the momenta of the decay products for each phase space point, such that the resonant state is on-shell. The subtraction term can then be written as

$$\mathcal{R}_s = \frac{m^2 \Gamma^2}{(p^2 - m^2)^2 + m^2 \Gamma^2} \left| \tilde{\mathcal{A}}_{n+1}^R \right|^2, \quad (5.3)$$

where  $m$  and  $\Gamma$  are the mass and width, respectively, of the resonant state,  $p$  is the (unshuffled) sum of the decay product momenta, and  $|\tilde{\mathcal{A}}_{n+1}^R|^2$  is the contribution of the resonant diagrams, calculated with the reshuffled momenta.

This choice of subtraction term is not only gauge invariant, it also includes the spin correlations of the decay products.

In SHERPA, on-shell subtraction has been fully automated for all SUSY-QCD NLO processes. For processes with more than one possible on-shell resonance, a subtraction term is included for each resonance.

### 5.3.1. Width as a Regulator

The width,  $\Gamma$ , introduced in equation (5.1), is treated simply as a regulatory parameter, shielding the divergence of the on-shell propagator, rather than a physical quantity; while there is obviously a physical width associated with the unstable particle whose decay is subtracted, it is not necessary, nor even advised, to use this width in the on-shell subtraction.

The subtraction is made in the narrow-width approximation, where the momenta for the subtraction term are reshuffled to place the decaying resonance on-shell. This is then smeared over a Breit-Wigner-type distribution in the invariant mass of the decay products before reshuffling, to match the shape of the full distribution and suppress contributions to the subtraction term from points far from the resonant peak.

The further the points are from the resonant peak, the more reshuffling is required to place the resonance on-shell, and the further the reshuffled momenta are in phase space from the original momenta. This can easily result in missed binning, where the subtraction term is placed in a different histogram bin from the main cross section contribution at the original phase space point. Reducing the width parameter results in a higher, narrower peak in the invariant mass distribution of the decay products for both the subtraction term, and the full distribution. This reduces the effects of missed binning, as phase space points far from the resonant peak are heavily suppressed by the Breit-Wigner smearing prefactor.

Also, in many of the cases where on-shell subtraction is required, we do not want to consistently treat the decaying particle as unstable. This can be seen clearly in the example of squark-gluino production mentioned previously. For instance, for the case

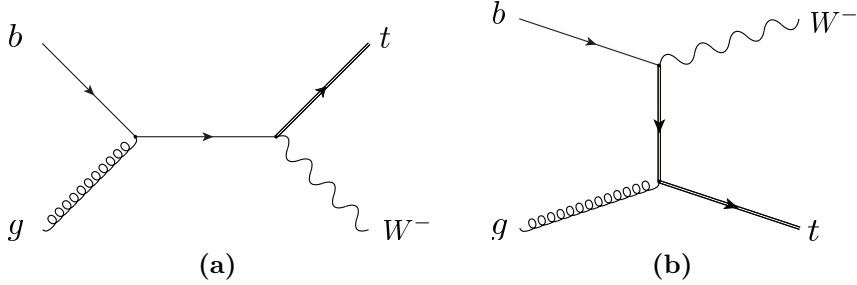


**Figure 5.3.:** Feynman diagrams for LO contributions to  $Wt$  production.

where the gluino is more massive than the squark, then processes with gluino decays to a squark and antiquark are subtracted. However, an undecayed gluino is also a final state particle in this process. If gluinos are treated consistently as unstable, with a large (physical) width, then not only is the evaluation of the matrix elements ill-defined, as unstable particles cannot be asymptotic states, leading to, for instance, possible gauge dependence or unitarity violation, but also the cancellation of IR singularities by the dipole subtraction terms may be compromised.

In the AMEGIC++ matrix element generator, it is not possible to introduce the width solely in the relevant propagator, it must be included everywhere in the particular subprocess. However, by reducing the relative size of the width, the effects due the inclusion of this parameter may be reduced, and a study of the change in cross section with the variation of the width parameter may confirm that these effects are negligible for suitable choices of the width parameter (see Section 7.2).

### 5.3.2. A Standard Model Example

There are many examples of SUSY processes which require on-shell subtraction at NLO to avoid double counting, due to the natural abundance of heavy, unstable states in SUSY theories. However, on-shell subtraction is also needed in certain cases in the Standard Model. A common example of such a case is in the isolation of the NLO corrections to single top with associated  $W$ -production from leading order top-pair production, with a leading order decay of the antitop.

At leading order, there is only one channel for single top with associated  $W$ -production,  $gb \rightarrow Wt$ , with two Feynman diagrams, shown in Figure 5.3. This is a well defined process at this order.

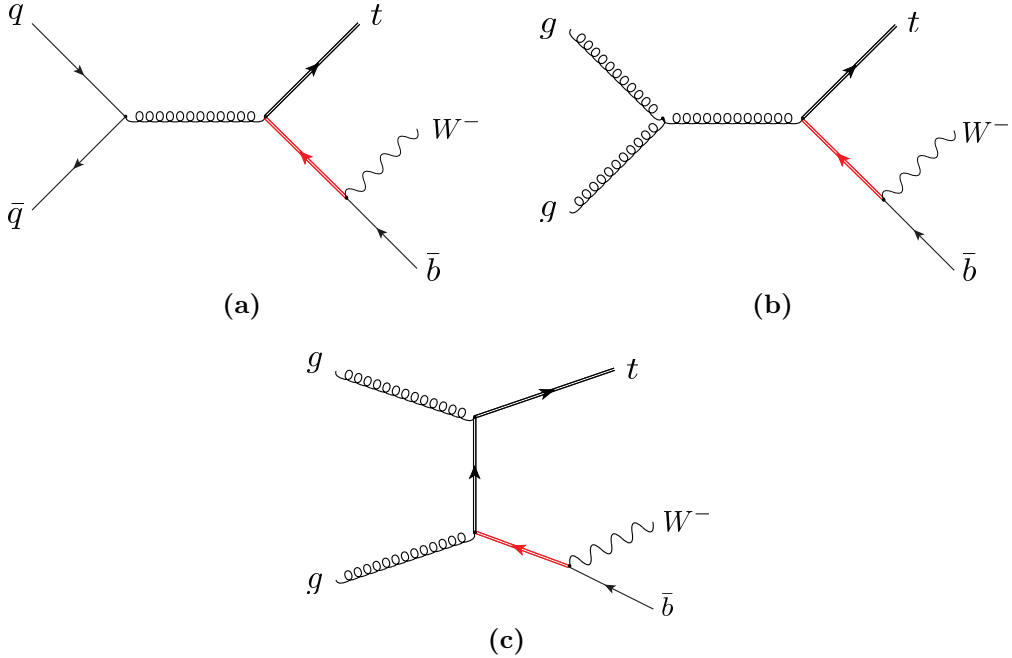


**Figure 5.4.:** Selected Feynman diagrams for NLO real-emission contributions to  $Wt$  production. Highlighted in red are those propagators which may go on-shell.

However if we look at the diagrams associated with this process at NLO, we can see that there are several which may result in an on-shell intermediate antitop, which decays into a  $W$  boson and bottom quark. The subset of the NLO diagrams with this resonance are shown in Figure 5.4.

In an identical way to the SUSY case described above, the NLO corrections to single-top production may be separated from LO top-pair production by the use of an on-shell subtraction term [135–138, 141, 145].

# Chapter 6.

## Photonic Corrections

The previous chapters on dipole subtraction have dealt with NLO corrections under QCD interactions. These corrections are extremely important, because they have significant effects, and all interactions at a hadron collider, such as the LHC, involve QCD partons.

There are, however, another set of NLO corrections which may be considered. Electroweak NLO corrections, while generally smaller than the QCD equivalents, may also be significant for some processes at the LHC. This is particularly true of processes with leptonic final states, such as neutral- and charged-current Drell-Yan, where there are clean experimental signatures and high statistics which will result in very high precision measurements.

Electroweak interactions involve the electroweak gauge bosons, the photon ( $\gamma$ ), and the three massive bosons ( $Z$ ,  $W^+$  and  $W^-$ ), and NLO electroweak corrections involve corrections due to all four of these bosons.

However, from a computational point of view, it is only the photonic corrections which present technical difficulties similar to the QCD case: as the other electroweak bosons are massive, their interactions do not produce soft and collinear divergences in the real and virtual NLO contributions. Therefore, there is no need to perform dipole subtraction to cancel these divergences.

The photonic corrections, on the other hand, behave in a very similar way to the QCD corrections discussed before. In this chapter, the extension of the Catani-Seymour dipole subtraction formalism to the case of photonic corrections and its implementation in SHERPA will be discussed.

## 6.1. Real Subtraction Terms

For photons radiated from charged fermions, the real subtraction terms are trivially related to the QCD case, and can be found in reference [54]. The kinematics of the photon emission dipole splitting functions are the same as the QCD equivalents, the only difference is in the treatment of colour and charge: the reduced Born amplitudes for the QCD case require colour connections, but the photonic subtraction terms simply have a scalar charge factor. There is only one splitting for which the kinematics of a subtraction term given in reference [54] are not precisely equal to the equivalent subtraction term from reference [56]: in Eq. (3.1) of the former, a purely conventional extra factor of  $\frac{1}{(1-y_{ij})}$  is included, which only affects the non-singular terms. For this splitting the SHERPA implementation follows the Catani-Seymour convention.

The subtraction terms involving the splitting of photons into fermions are given in reference [103], and contain more fundamental differences to the QCD dipoles. In general, the splitting of a vector boson into fermions gives rise to collinear divergences only, with no soft divergences being present. In practice this means that for photon splitting a summation over all possible spectator particles is not necessary <sup>1</sup>. However, the dipole formalism, as with every other local subtraction algorithm, relies on a direct correspondence between real emission contributions and underlying Born terms, and this requires a way to deal with the recoil emerging from recombining a splitting. In the dipole formalism this is achieved through a spectator particle absorbing the recoil in a well-defined manner. This procedure guarantees momentum conservation and allows all external particles to always remain on their mass-shell when momenta are mapped from an  $m+1$ -particle real emission phase space to an  $m$ -particle Born phase space. In QCD the spectator is colour-connected to the splitter, but in QED, due to the absence of colours, there is some freedom in defining the spectator in cases where there are no soft divergences. In particular, in photon splitting to fermions, the charge factor associated with the dipole is unambiguously taken as the square of the charge of the emitted fermion, and therefore the spectator does not even need to be charged.

The default choice for spectators for photon splitting to fermions are taken to be a final state spectator for final state emitters, and an initial state spectator for initial

---

<sup>1</sup>In the case of a gluon splitting to quarks, a summation over all spectators allows the incorporation in a transparent way of all possible colour correlations, which may be cumbersome to trace otherwise, and which, of course, are absent in QED.

state emitters. Various choices of spectators were tested, but the differences in overall convergence of the integrals were found to be insignificant.

## 6.2. Integrated Subtraction Terms

In the two publications dealing with the electromagnetic dipoles (references [54, 103]), a mass regularisation scheme has been used, where divergences are regularised by (infinitesimally) small photon and fermion masses. The default dipole formulae used in this implementation based on the SHERPA framework are trivial combinations of the various expressions presented in references [54, 56, 103]: they represent dipole terms for electromagnetic corrections using dimensional rather than mass regularisation. A summary of the integrated subtraction terms for photonic dipoles using dimensional regularisation can be found in Appendix D.

There are several differences with respect to the QCD case: firstly, there is the simplification due to the lack of colour correlations; these have been replaced by scalar charge factors. Other differences in the form of the integrated subtraction terms result from the lack of a sum over spectators for some dipole terms, as discussed above. However, the integrated terms are still easily arranged into an  $\mathbf{I}$  term, which contains all IR divergences, and finite  $\mathbf{K}$  and  $\mathbf{P}$  terms, in analogy with reference [56].

## 6.3. Renormalisation Scheme

As described in Section 2.2.2, there must be flexibility in the possible definitions of the electroweak renormalisation scheme, to allow for the options provided by different one-loop codes. For the dipole terms, the practical consequence of this flexibility is that a different value of the coupling  $\alpha$  may be used for the photonic corrections, independent of the value used in the rest of the calculation.

To take a solid example, when considering the corrections to  $pp \rightarrow l^+ \nu_l$ , one may want to use  $\alpha_{G_\mu}$  in the couplings of the  $W$ -boson, but  $\alpha(0)$  for the extra photon coupling in the corrections.

To allow for complete flexibility, two parameters are defined:

- $\alpha_{OLP}$ , which is the effective coupling used by the one-loop code in the calculation of the leading order matrix element. It is defined as

$$\alpha_{OLP} = \alpha(0) \left( \frac{|\mathcal{A}_{LO}^{OLP}|^2}{|\mathcal{A}_{LO}^{MC}|^2} \right)^{1/P} \quad (6.1)$$

where  $P$  is the leading order power of alpha,  $OLP$  labels the LO matrix element calculated by the one-loop code, and  $MC$  labels the LO matrix element calculated by the Monte Carlo.

- $\alpha_{IR}$ , which is the coupling used for the photonic corrections.

For the poles to cancel between the one-loop result and the integrated dipole terms, both of these couplings must be used, resulting in an expression with an overall coupling factor given by  $\alpha_{OLP}^P \alpha_{IR}$ .

In theory, the definitions of  $\alpha_{OLP}$  and  $\alpha_{IR}$  may be arbitrarily complicated, and even phase space dependent, but, as these couplings are returned from the one-loop code for each phase space point, it is possible to simply reweight the Born and integrated subtraction terms by the appropriate factors for each phase space point.

Unfortunately, if these factors are phase space dependent, then it may not be simple, or possible, to apply the same couplings to the real-emission terms. However, it is technically sufficient to use a constant coupling for the real correction terms, as the difference is formally of a higher order than the NLO calculation.

## 6.4. Regularisation Scheme

The result of any NLO calculation must be independent of the regularisation scheme chosen; the same regularisation scheme must be used for the virtual corrections and the integrated subtraction terms, in order for the singularities (and regularisation scheme dependence) to cancel.

Dimensional regularisation, as used in reference [56], is preferred as the default for the Binoth Les Houches Interface, and this is SHERPA's default regularisation scheme for the subtraction terms. However, many electroweak one-loop providers prefer to use mass regularisation, where singularities are parameterised by introducing a (formally infinitesimally) small regulator mass for the fermions and the photon. In this scheme,

singularities manifest themselves as logarithms of the regulator mass. To convert the integrated dipole terms from one scheme to another, only the  $\mathbf{I}$  term (equation (D.3)), which contains all of the divergences, must change. The relevant logarithms for the mass regularised  $\mathbf{I}$  terms as implemented in SHERPA can be found in references [54, 103].

## 6.5. Factorisation Scheme

As discussed in Section 3.4, a collinear counterterm must be included in NLO calculations to cancel collinear divergences in the PDFs. The collinear counterterm takes the form

$$d\sigma_a^C(p; \mu_F^2) = -\frac{\alpha}{2\pi} \frac{1}{\Gamma(1-\epsilon)} \sum_b \int_0^1 dz \left[ -\frac{1}{\epsilon} \left( \frac{4\pi\mu^2}{\mu_F^2} \right)^\epsilon P^{ab}(z) + K_{\text{F.S.}}^{ab}(z) \right] d\sigma_b^B(zp) , \quad (6.2)$$

where  $K_{\text{F.S.}}^{ab}(z)$  defines the factorisation scheme. The most popular factorisation scheme for QCD is  $\overline{\text{MS}}$ , in which, by definition,  $K_{\text{F.S.}}^{ab}(z) = 0$ . However, as discussed in reference [146], DIS factorisation is most consistent with the MRST2004qed PDF [147], which is currently the only PDF set to include QED effects<sup>2</sup>.

## 6.6. Recombination and Cuts on Real-emission Phase Space

For the dipole formalism as implemented in AMEGIC++, observables must be defined in an infrared-safe, and, in particular, in a collinear-safe way. That is, the emission of a soft or collinear photon from a charged external particle must not change the observable, in agreement with the KLN and BN theorems underpinning the mutual cancellation of infrared divergences in real and virtual corrections. On a more practical level, this condition is necessary for cuts to be performed on the observables in a consistent way. In QCD, this is typically achieved through the inclusion of a suitable jet definition - triggering the combination of partons into the jets. For photonic corrections, the same effect can be achieved through a recombination prescription: if a photon is sufficiently

---

<sup>2</sup> Therefore, SHERPA offers both  $\overline{\text{MS}}$  and DIS factorisation for EW NLO, and the factorisation scheme can be chosen using the FACSCHEME tag.

collinear to a charged fermion ( $\Delta R = \sqrt{(y_f - y_\gamma)^2 + \Delta\phi_{f\gamma}^2}$  less than 0.1, for instance), then the two are recombined into one pseudo-particle<sup>3</sup>.

To deal with this issue, the following algorithm emerges:

- A real-emission phase space point is generated. No cuts are applied at this stage.
- The mapped LO phase space points are calculated for each dipole individually. If the LO phase space passes the cuts, then the dipole's contribution is calculated and included.
- The real-emission phase space point is checked to see if any of the photons do not pass the isolation cuts and must be recombined with charged particles. If so, the photon and charged particle's momenta are added. If this new LO phase space point passes the cuts, then the real emission matrix element contribution is included.
- If there is no recombination to take place, the cuts are applied to the real-emission phase space point, and if the point passes, then the contribution is included.

Similar recombination procedures are employed in, for example, references [98, 148] for Z and W hadroproduction.

---

<sup>3</sup> This is performed automatically in SHERPA before cuts are applied to the phase space for the real emission process, according to the algorithm below. To change the cut value in  $\Delta R$ ,  $\Delta R_{\text{cut}}$  from its default value of 0.1, the RECOMBR-tag can be used in the ME section of the run card.

# Chapter 7.

## Tests of the Implementation

The implementation of the schemes described in the previous chapters has been extensively tested. In this chapter some of the internal tests performed will be reviewed; the first section covers checks of the dipole subtraction, the second section details some consistency checks for the on-shell subtraction, and the final section documents some of the first physical applications of the NLO framework, including cross checks with previous results or existing code where possible.

### 7.1. Internal Tests of Dipole Subtraction

#### 7.1.1. Technical Cut-off Parameter Variation

In the dipole subtraction method, phase space points close to a singular region of phase space do not contribute significantly, as the subtraction term exactly matches the singular behaviour of the real emission contribution. However, it is clear that for phase space points very close to the singularity the subtraction procedure necessarily involves the subtraction of almost identical very large numbers. This is a numerically unstable procedure. Therefore, a technical cut off,  $\alpha_{tech}$ , must be included, which specifies a region very close to the singularity for which it is assumed that the real emission contribution and the subtraction term exactly cancel (to numerical accuracy), and their difference does not actually need to be calculated.

The technical cut off is applied to a kinematic variable for each dipole. The kinematic variables chosen are the same variables used for the phase space restriction described in Section 3.7.1. The variables and references to their definitions are listed in Table 3.3.

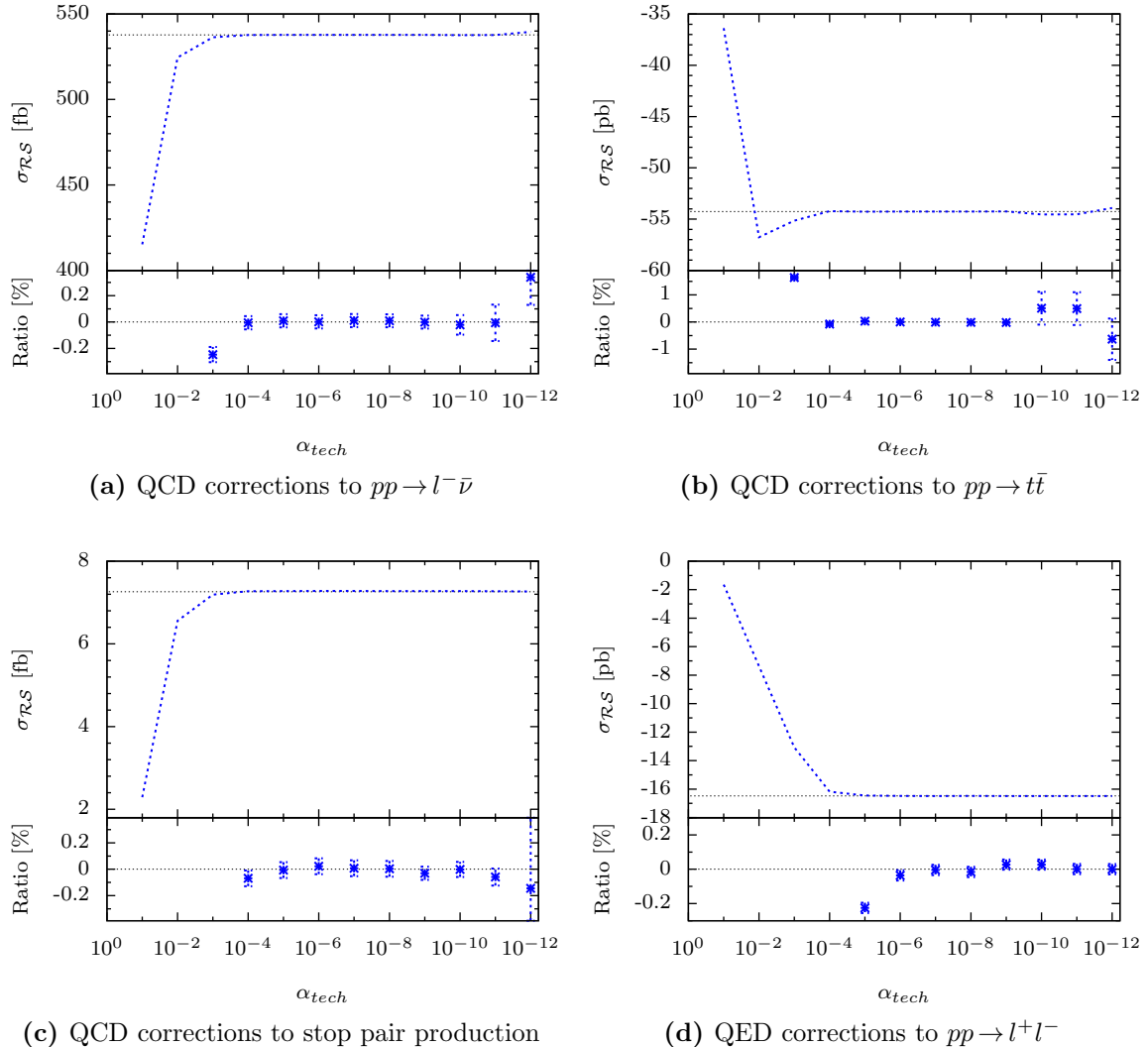


**Figure 7.1.:** Plot of subtracted real NLO contributions to various processes as a function of the unphysical technical cut-off parameter  $\alpha_{tech}$ . It can be seen that the subtracted real contribution is effectively constant, within statistical errors, in the range  $10^{-12} \lesssim \alpha_{tech} \lesssim 10^{-6}$ , although statistical errors may increase at the smaller end of this range, indicative of slower convergence. The SHERPA default for  $\alpha_{tech}$  is  $10^{-8}$ .

To generalise the notation for all dipoles, we shall call the parameter in which the  $\alpha$  cuts are made  $y_i$ , where  $i$  runs over all dipoles, 1 to  $n$ . This parameter depends on both the dipole-type (final-final, final-initial, initial-final or initial-initial), and the kinematics of the three relevant partons (the emitter, the spectator and the unresolved parton), and can vary from 0 to 1. As  $y_i$  approaches 0 for any given dipole, the phase space point approaches the relevant singularity for that dipole.

Another parameter,  $y_{min}$  is defined as the minimum value of any of the individual  $y_i$  for a given phase space point,

$$y_{min} = \min\{y_i\} , \quad (7.1)$$

and thus the technical cut off may be neatly expressed as

$$\int_{m+1} [d\sigma_R - d\sigma_A] \Theta(y_{min} - \alpha_{tech}) . \quad (7.2)$$

The parameter  $y_{min}$  parameterises how close a phase space point is to a singularity, and the technical cut off determines how close one should be to the singularity before the point is ignored. Obviously, the technical cut off parameter is unphysical, and the result must be independent of its exact value. However, if this parameter is set too high, then significant finite contributions may be omitted, as the cut-off is not sufficiently close to the singularity for the subtraction term to adequately cancel the real emission contribution. If this parameter is set too low, the instability associated with subtracting very large numbers becomes apparent.

Plots of the result for the subtracted real-emission contribution to the cross section ( $\mathcal{RS}$ ) over several orders of magnitude of  $\alpha_{tech}$  are discussed below for massive QCD dipoles, and photonic dipoles.

Figure 7.1 shows the subtracted real-emission QCD or QED NLO corrections for various processes, as a function of the technical cut-off parameter  $\alpha_{tech}$ . From these plots it can be seen that values of  $\alpha_{tech}$  above approximately  $10^{-6}$  cause a significant change in the value of the subtracted real contributions. Also values of  $\alpha_{tech}$  below approximately  $10^{-10}$  show larger errors, indicative of lack of convergence due to the numerical instabilities.

From these plots, it may be gathered that the size of the contributions to the cross section which are missed by imposing a technical cut-off are small, as varying the cut-off

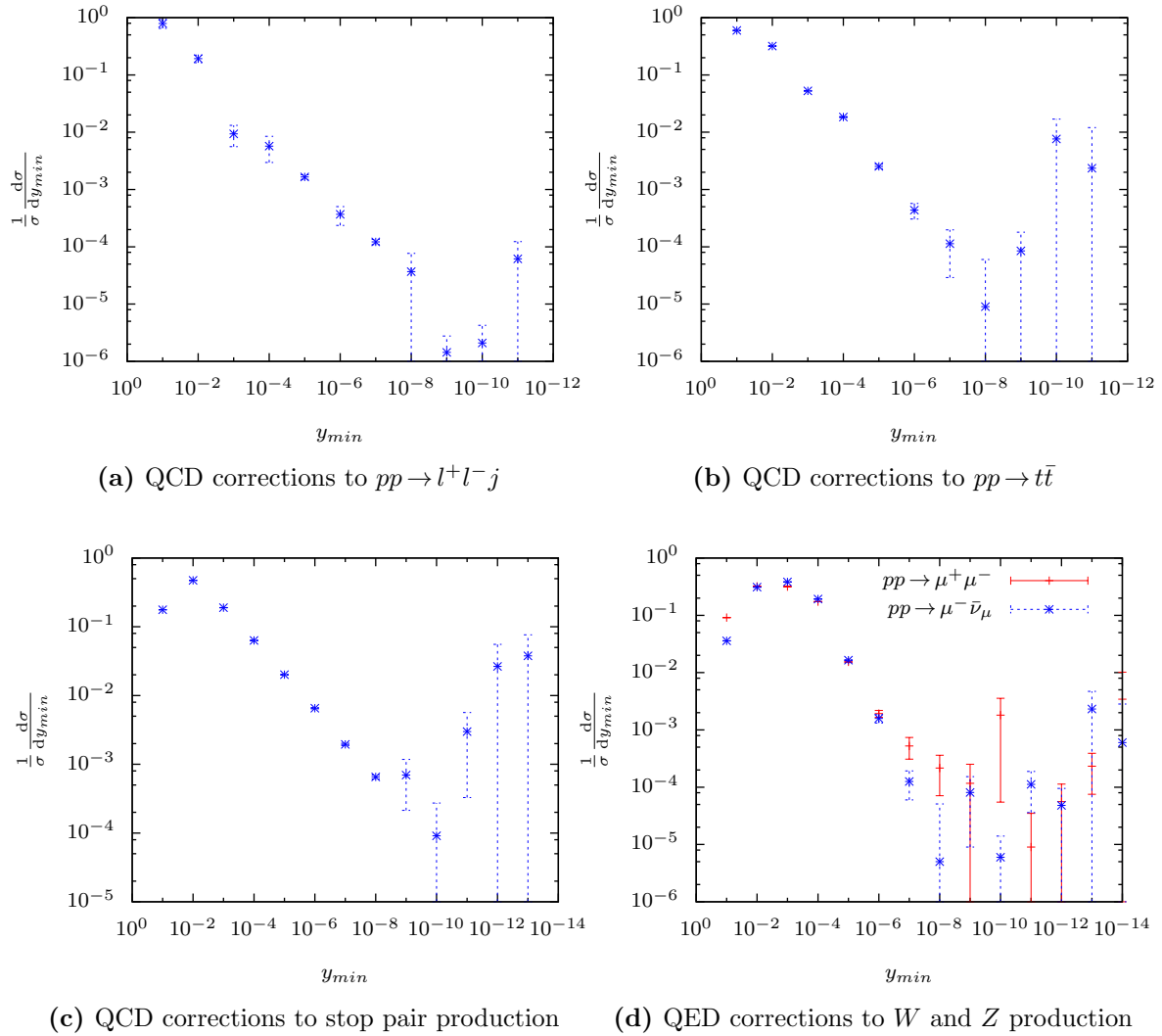


**Figure 7.2.:** Subtracted real-emission contribution to various processes, in bins of  $y_{min}$ .  $y_{min}$  effectively parameterises how close a phase space point is to a divergence, with  $y_{min} \rightarrow 1$  equivalent to finite regions, and  $y_{min} \rightarrow 0$  equivalent to divergent regions.

over several orders of magnitude does not significantly alter the cross section result. Another way to quantify the relative importance of these ignored terms is to plot the normalised subtracted real emission cross section contribution in bins of  $y_{min}$ . These plots also clearly show the numerical problems created by calculating contributions too close to the singularity.

Figure 7.2 shows normalised subtracted real contributions in bins of  $y_{min}$  for massive QCD, SUSY-QCD and photonic corrections. In all of the plots, it can be seen that the largest contribution to the subtracted cross section comes from the regions of phase space far from the singularities, where  $y_{min}$  is relatively close to 1 ( $y_{min} \gtrsim 10^{-4}$ ). As the value of  $y_{min}$  decreases, the total contribution to the real correction decreases. This effect is due to the subtraction term: as the phase space points get closer to the singularity, the subtraction term matches the singular behaviour, giving a small overall contribution. However, when  $y_{min}$  is below about  $10^{-9}$ , the contributions begin to grow again, with large error bars. This increase is the result of the numerical instability, and should be removed using an appropriately chosen  $\alpha_{tech}$  cut off.

The default value for  $\alpha_{tech}$  in SHERPA is  $10^{-8}$ .

The numerical stability of the subtracted cross section with respect to the variation of the technical cut off provides both a test of the robustness of the subtraction procedure, and a test of this specific implementation.

### 7.1.2. Phase Space Restriction Parameter

As described in Section 3.7.1, each dipole term may be restricted such that it contributes only in regions of phase space close to the relevant singularities. The parameter introduced to control the extent of this phase space restriction is labelled  $\alpha$ .

The advantage of introducing this phase space restriction is the reduction of the number of subtraction terms required for each phase space point, resulting in an increase in efficiency. The dependence of the mean number of subtraction terms required per phase space point for a number of processes, may be seen in Figure 7.3, 7.4, and 7.5 for massless QCD, massive QCD and photonic dipole terms respectively.

The number of dipole terms per phase space point increases with the number of external coloured (or charged) particles, but this effect may be neutralised by decreasing the  $\alpha$  parameter, which reduces the number of required dipole terms dramatically.

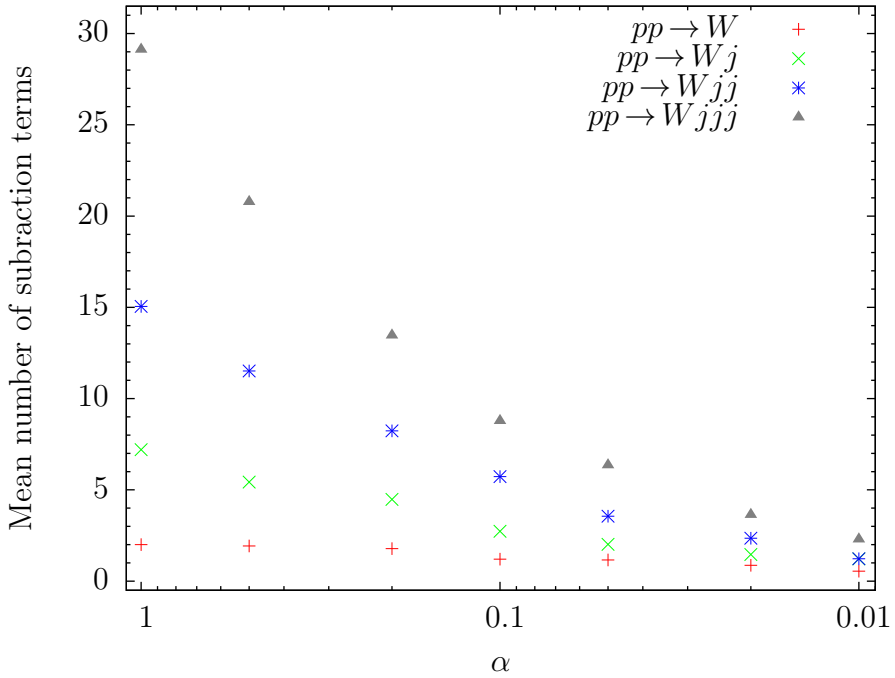


**Figure 7.3.:** Plot of mean number of valid QCD real subtraction terms per phase space point, for QCD corrections to  $W$ +jets as a function of the unphysical phase space restriction parameter  $\alpha$ . As expected, the mean number of subtraction terms drops quickly as  $\alpha$  decreases.

Both the subtraction terms and their integrated counterparts independently depend on the value of  $\alpha$ . However, the phase space restriction parameter is an unphysical, free parameter, and as such the full NLO result must be independent of its value. Thus, varying  $\alpha$  provides a non-trivial check of the dipole implementation.

Figures 7.6, 7.7 and 7.8 show the QCD or QED NLO corrections to various processes as a function of the phase space restriction parameter  $\alpha$ .

The total cross section corrections plotted in these figures are constant with varying  $\alpha$ , within statistical errors, as expected.

However, an important feature of the numerical calculation is also apparent in these figures. In all of these plots, the real-emission contribution increases with decreasing  $\alpha$ . This is expected, as the subtraction terms contribute over less of the phase space. However, for several of these processes, this growth in the real-emission contribution is already a problem for  $\alpha \lesssim 0.1$ : the statistical errors for the total cross section are significantly larger in this region. This is not due to any difference in the convergence of the integral (in fact, the percentage errors on these real contributions are less than for larger values of  $\alpha$ ), but simply due to the fact that higher precision is required in each

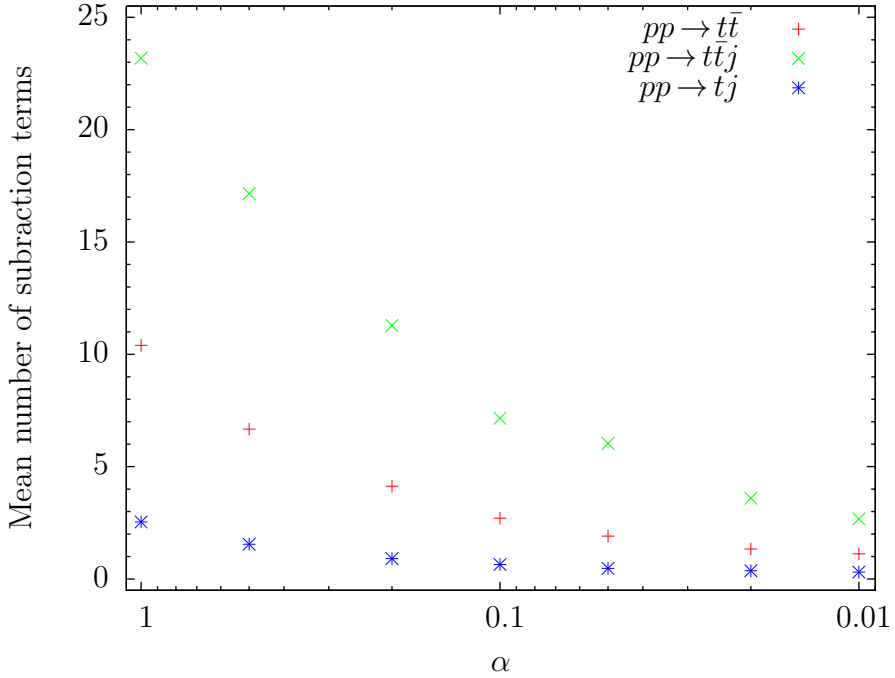


**Figure 7.4.:** Plot of mean number of valid QCD real subtraction terms per phase space point, for  $pp \rightarrow t\bar{t}$ ,  $pp \rightarrow t\bar{t}j$  and  $pp \rightarrow tj$  as a function of the unphysical phase space restriction parameter  $\alpha$ . As expected, the mean number of subtraction terms drops quickly as  $\alpha$  decreases.

of the real and virtual contributions to achieve the same accuracy in the sum, due to large cancellations between these two elements. Therefore, the absolute value of each of the two contributions should be a consideration when choosing the most efficient value of the phase space restriction parameter, and large cancellations between them should be avoided.

## 7.2. Internal Tests of On-shell Subtraction

The subtraction procedure, as described in Section 5.3, involves a reshuffling of momenta, to place the resonance on-shell. As momenta and energy are conserved, and all final state particles remain on-shell, there must be at least one extra particle involved in this reshuffling procedure, other than the decay products, whose momentum absorbs the kick-back. This particle is called the spectator.

There is obviously some freedom in the exact prescription used for the reshuffling. There are two main choices to be made: one choice is which particle to choose as the spectator; the other choice is the exact algorithm used for the reshuffling. A description

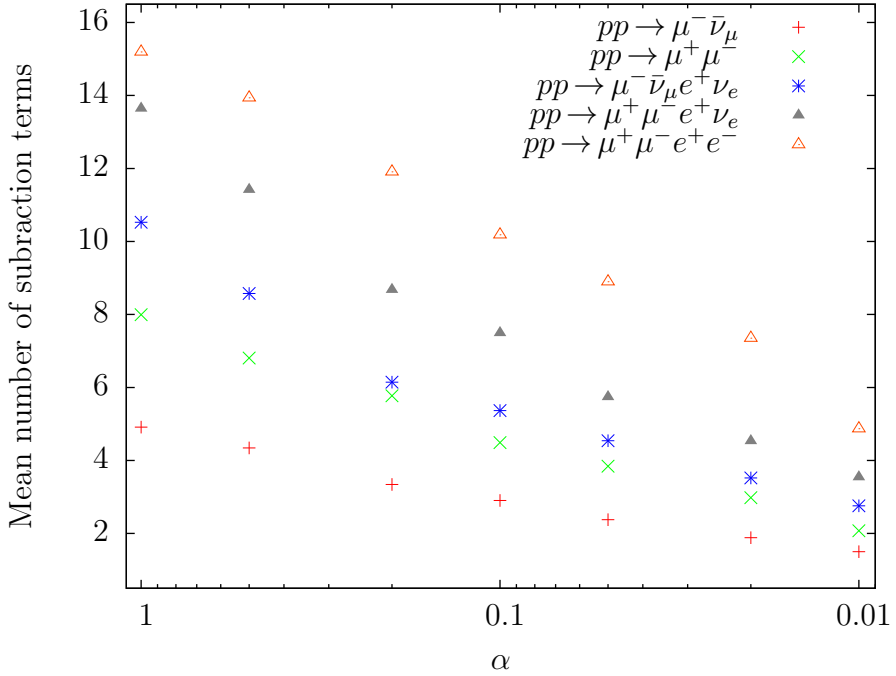


**Figure 7.5.:** Plot of mean number of valid photonic real subtraction terms per phase space point, for  $W$ ,  $Z$ ,  $WW$ ,  $WZ$ , and  $ZZ$  production processes as a function of the unphysical phase space restriction parameter  $\alpha$ . As expected, the mean number of subtraction terms drops quickly as  $\alpha$  decreases.

of the options provided by the implementation in SHERPA for both of these choices is given in Appendix C.

The choices of spectator or reshuffling algorithm are not fundamental to the procedure, and therefore it is expected that the precise details are irrelevant, and different choices should yield the same results.

**Spectator Choice** The choice of spectator only becomes relevant in the case of four or more final state particles in the real-emission contribution. Figure 7.9 shows a comparison of real-emission cross sections for six different definitions of the spectator choice (detailed in Appendix C) for a single subprocess.

**Reshuffling Procedure** The choice of reshuffling procedure is relevant regardless of the final state multiplicity. Figure 7.10 shows a comparison of real-emission cross sections for six different reshuffling algorithms (detailed in Appendix C) for a single subprocess. Figure 7.11 shows a comparison of the reshuffling algorithms for the squark transverse momentum distribution in NLO squark-gluino production.

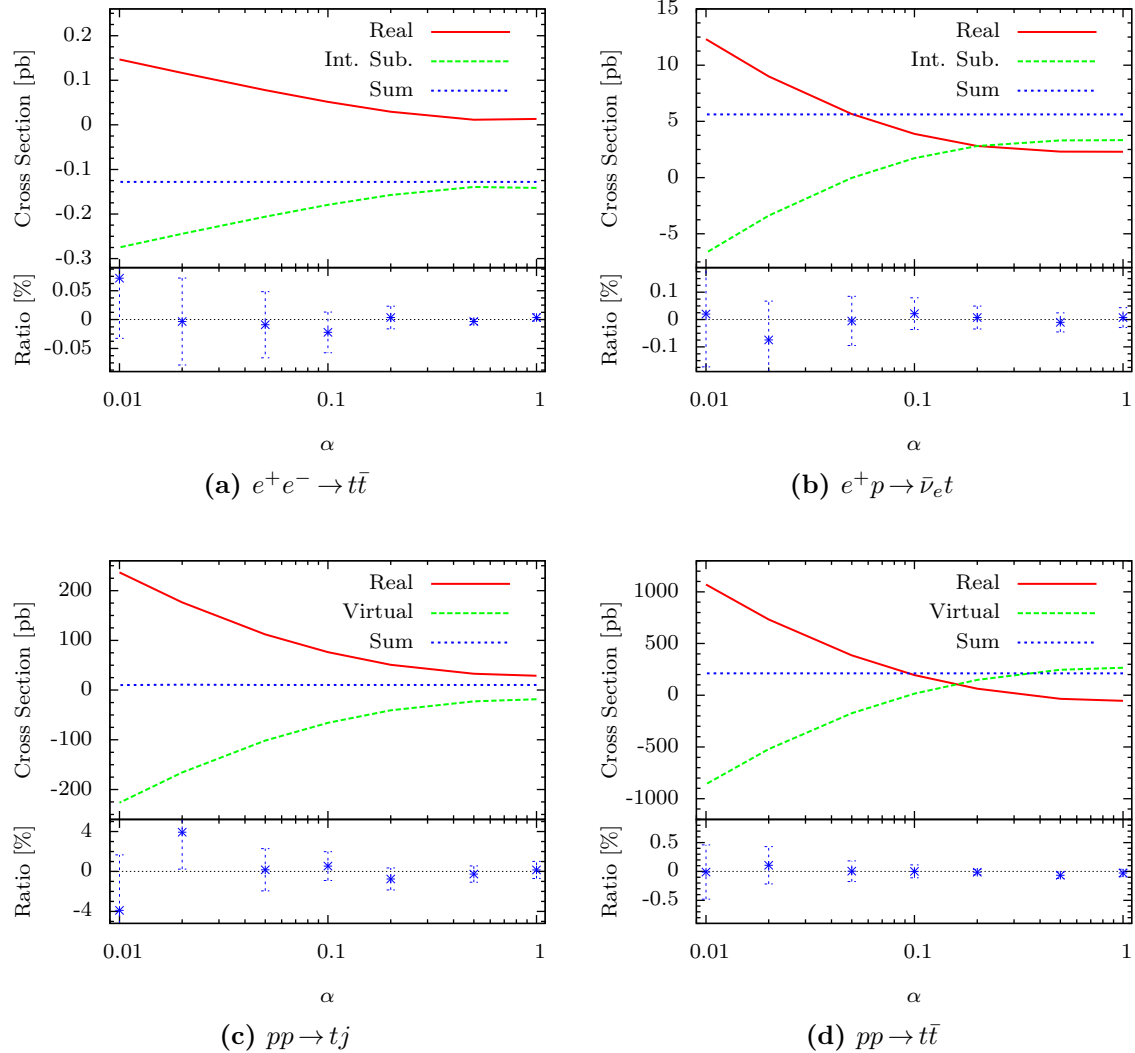


**Figure 7.6.:** Plot of real and virtual QCD NLO contributions various processes involving massive partons as a function of the unphysical phase space restriction parameter  $\alpha$ . The ratio is over the mean value for the sum of the two contributions. The results shown are from calculating 1,000,000 phase space points of the real contribution, which dominates the total statistical error. The full NLO correction is shown for the processes for which the loop matrix element was available in SHERPA through an interface to MCFM (Figures 7.6c and 7.6d), while the remaining plots show only the subtracted real contribution and the finite part of the integrated dipole terms.

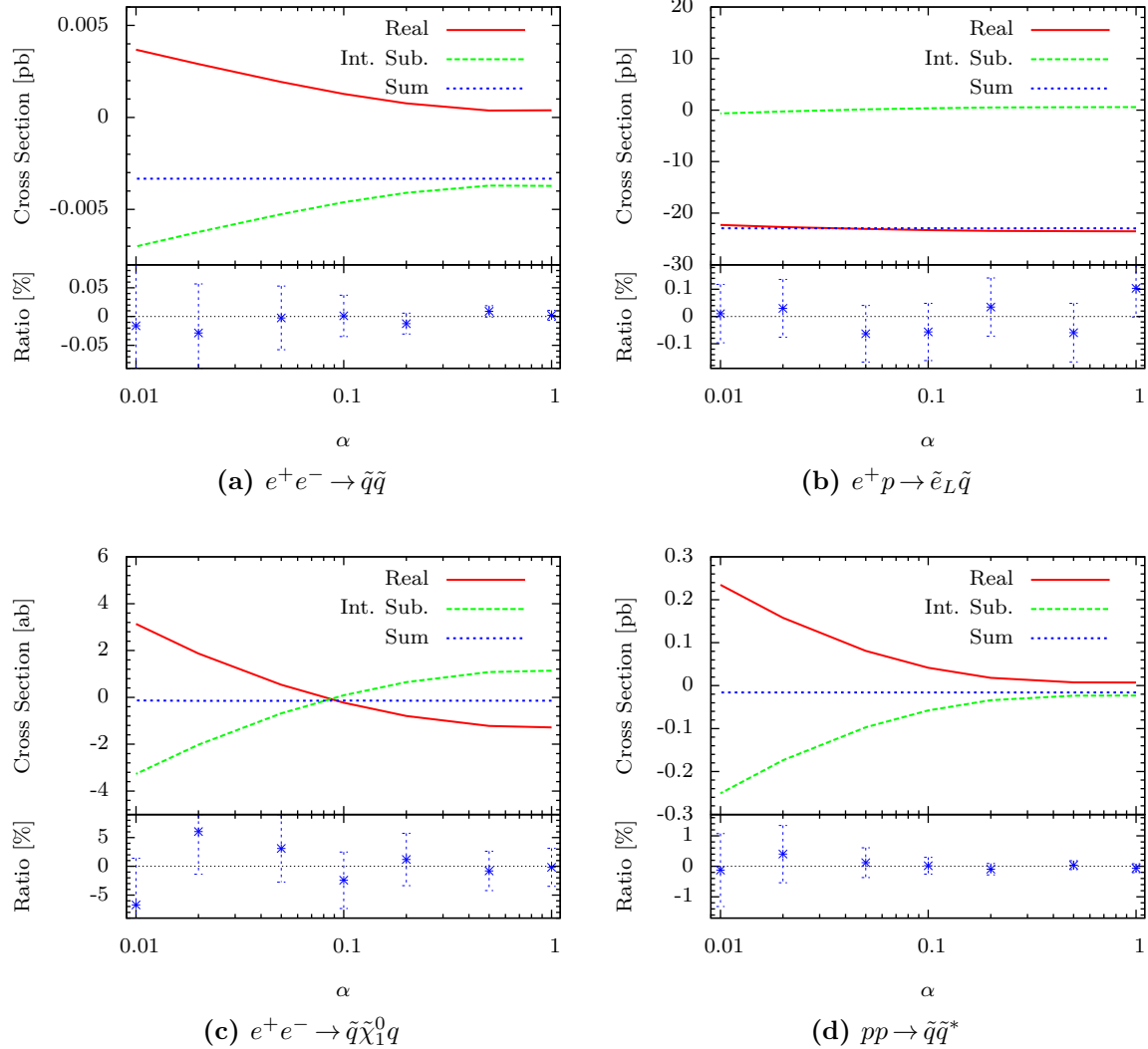


**Figure 7.7.:** Plot of real and virtual QCD NLO contributions for various SUSY processes as a function of the unphysical phase space restriction parameter  $\alpha$ . The ratio is over the mean value for the sum of the two contributions. The results shown are from calculating 1,000,000 phase space points of the real contribution, which dominates the total statistical error. The plots show only the subtracted real contribution and the finite part of the integrated dipole terms; the one-loop matrix elements are not included.

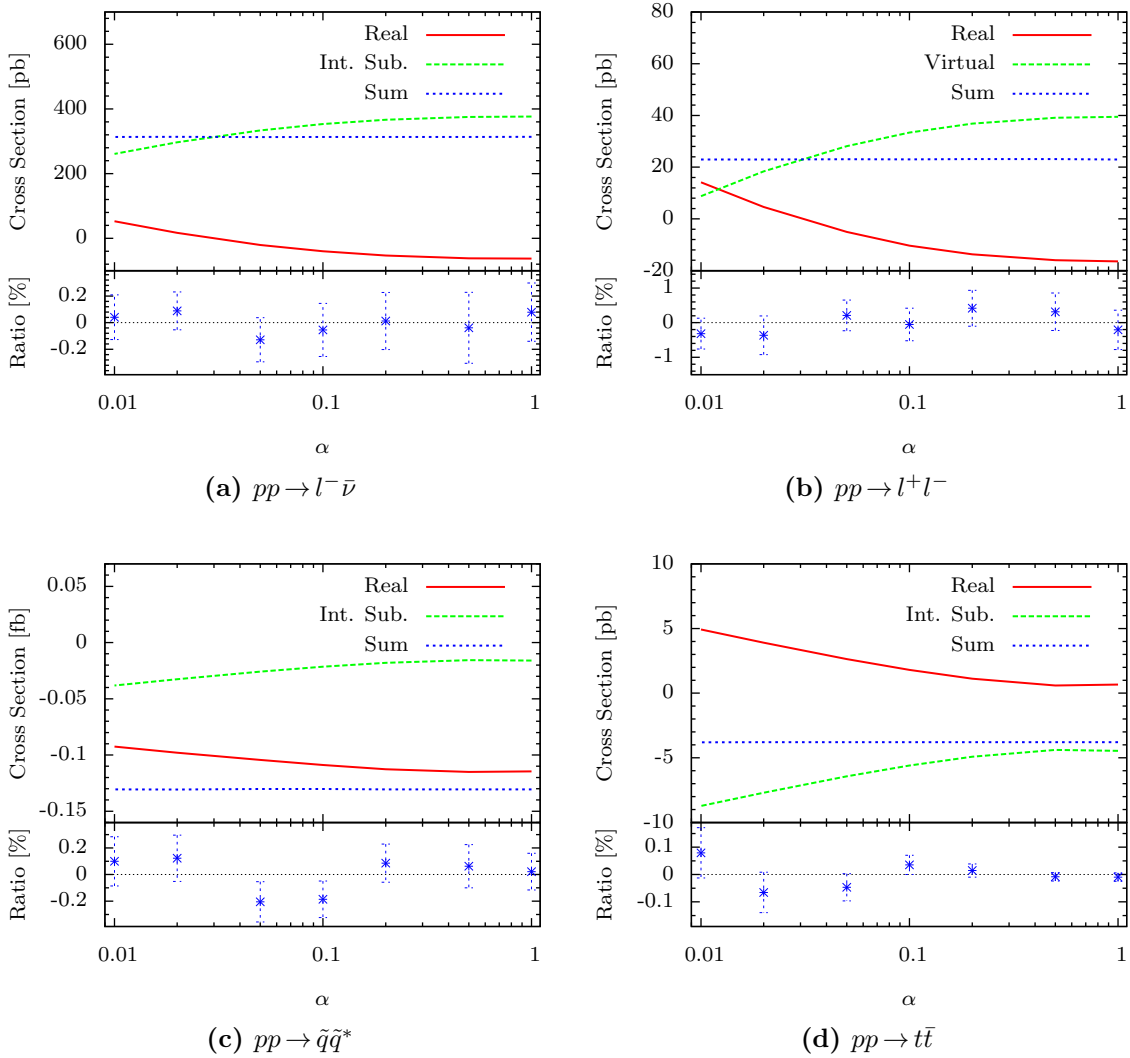


**Figure 7.8.:** Plot of real and virtual QED NLO contributions for various processes as a function of the unphysical phase space restriction parameter  $\alpha$ . The ratio is over the mean value for the sum of the two contributions. The results shown are from calculating 1,000,000 phase space points of the real contribution, which dominates the total statistical error. The full NLO correction is shown for the processes for which the loop matrix element was available through an interface to RADY (Figure 7.8b), while the remaining plots show only the subtracted real contribution and the finite part of the integrated dipole terms.

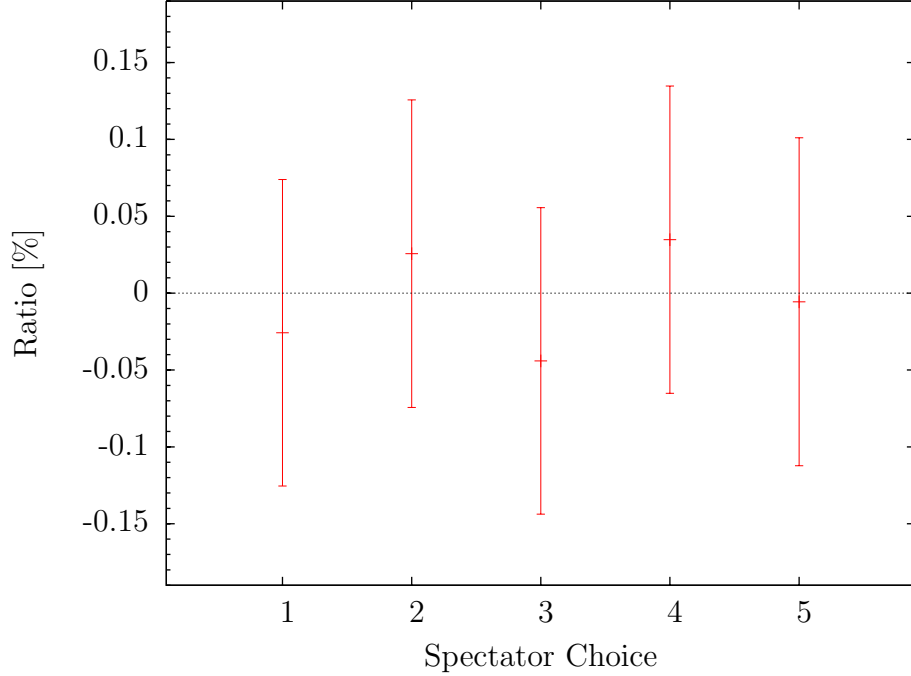


**Figure 7.9.:** Comparison of various on-shell reshuffling algorithms for the example case of  $q\bar{q} \rightarrow \tilde{u}_L \tilde{g} \tilde{u}\gamma$ , with  $m_{\tilde{g}} > m_{\tilde{u}_L}$ . The ratio is given by  $\frac{\sigma^{RS} - \bar{\sigma}^{RS}}{\bar{\sigma}^{RS}}$ , where  $\bar{\sigma}^{RS}$  is the average of the range of results.

It can be seen from Figures 7.9, 7.10 and 7.11 that the subtracted result is independent of both the reshuffling algorithm and the choice of spectator.

### 7.2.1. Width Variation

As described in Section 5.3.1, the width used for on-shell subtraction is not the physical width, but rather an unphysical regularisation parameter. As such, the cross section results should be independent of the exact value of this parameter. Figure 7.12 shows the real-emission contribution to the subprocess  $q\bar{q} \rightarrow \tilde{g}\tilde{c}\bar{c}$  as a function of the on-shell width parameter over the gluino mass. Finite width effects are seen for  $\Gamma \gtrsim 0.001m_{\tilde{g}}$ , including for the physical width  $\Gamma \sim 0.01m_{\tilde{g}}$ . For widths below  $0.001m_{\tilde{g}}$ , the subtracted cross section is constant, within statistical errors, as expected. For  $\Gamma \lesssim 10^{-8}m_{\tilde{g}}$  there are numerical problems which limit convergence.

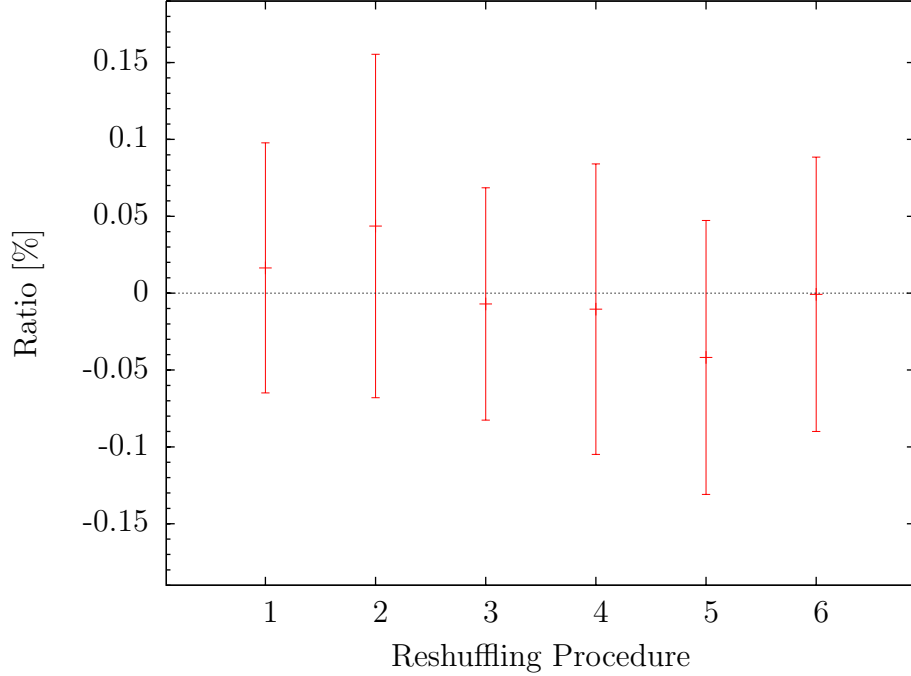


**Figure 7.10.:** Comparison of on-shell reshuffling algorithms for the example case of  $q\bar{q} \rightarrow \tilde{u}_L \tilde{g} \tilde{u}$ , with  $m_{\tilde{g}} > m_{\tilde{u}_L}$ . The ratio is given by  $\frac{\sigma^{RS} - \bar{\sigma}^{RS}}{\bar{\sigma}^{RS}}$ , where  $\bar{\sigma}^{RS}$  is the average of the range of results.

### 7.2.2. On-shell Cancellation

Of course, the point of on-shell subtraction is to remove the contribution from a production-and-decay process from the NLO real-emission contribution. For processes with internal propagators which may go on-shell, this is often the dominant contribution. This may be seen naively by power counting: for instance in  $tW$ -production, the contribution from on-shell top-pair production with a decay takes the form of a two-to-two production cross section with couplings  $\alpha_s^2$ , multiplied by a branching ratio of approximately unity, which one would expect to be larger than the standard real-emission corrections (couplings  $\alpha\alpha_s^2$ ), and even larger than leading order  $tW$ -production (couplings  $\alpha\alpha_s$ ). Therefore, a further test of the on-shell subtraction is afforded by checking if the artificially inflated on-shell real-emission corrections are neutralised by subtraction. Figure 7.13 shows a selection of distributions of sums of transverse energies ( $H_t$ ) from subprocesses which contribute to the real-emission correction to  $tW$  production, scaled by the leading order cross section. The top subprocess,  $gb \rightarrow tW^- g$ , does not contain a potentially on-shell propagator. The other subprocesses,  $gg \rightarrow tW^- \bar{b}$ ,  $dd \rightarrow tW^- \bar{b}$  and  $uu \rightarrow tW^- \bar{b}$  contain  $\bar{t}$  propagators which may go on-shell. It can be seen that the unsubtracted contributions from these subprocesses are significantly larger

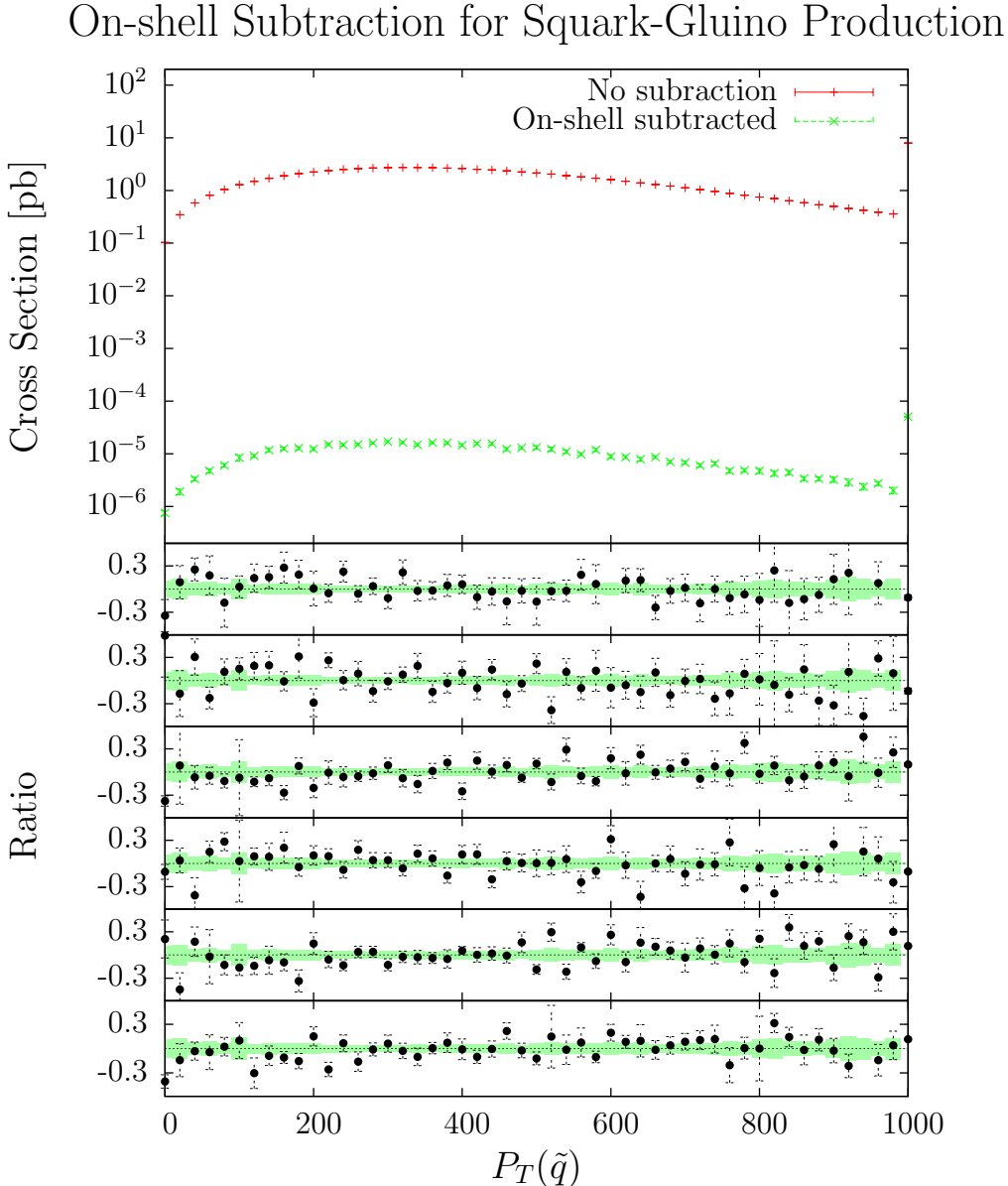


**Figure 7.11.:** QCD real emission contribution to the leading order process  $pp \rightarrow \tilde{g}\tilde{q}$  from the subprocess  $q'\bar{q}' \rightarrow \tilde{g}\tilde{q}\bar{q}$  as a function of the transverse momentum of the squark. The set of Feynman diagrams for this process include those with internal squark propagators which may go on-shell, requiring on-shell subtraction. The unsubtracted and subtracted contributions are plotted, for  $\Gamma_{\tilde{q}} = 0.0001m_{\tilde{q}}$ . The ratio plots below show the subtracted contributions calculated with various different reshuffling procedures, over the result produced by combining the six variations. The results agree for all of the reshuffling options.

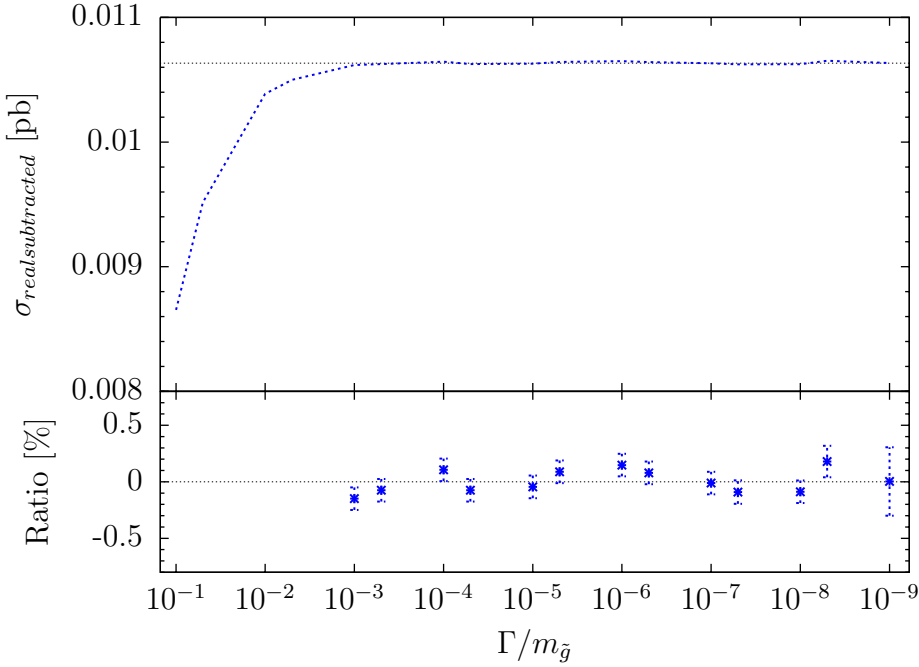


**Figure 7.12.:** Plot of the subtracted cross section for the subprocess  $d\bar{d} \rightarrow \tilde{g}\tilde{c}\bar{c}$ , which is part of the real-emission correction to  $pp \rightarrow \tilde{g}\tilde{c}$ , as a function of  $\Gamma/M$ , the regularisation parameter acting as the gluino width over the mass of the gluino.

than the leading order  $tW$  result, with the quark-quark initial states reaching a factor of two greater than the leading order result, and the gluon-gluon initial state a factor of 40 greater. When the subtraction is carried out, these large corrections are cancelled, as the large on-shell contributions are removed, leaving only the genuine NLO corrections, and the resulting correction factors have a magnitude of less than 2 for each of the subprocesses.

### 7.3. Comparative Tests

Where independent code is available for cross checks, it is obviously useful to make comparisons of results for individual phase space points. However, this type of test is not always possible due to differences in implementation. For instance, the reorganisation of the integrated dipole terms described in Section 3.8 means that the integrated dipole terms may not be completely compared to more straightforward implementations for a single phase space point, and results should only be identical after integration. However, some of the terms involved in the integrated dipole terms do directly correspond to other implementations, and careful selection and isolation of these terms does allow some

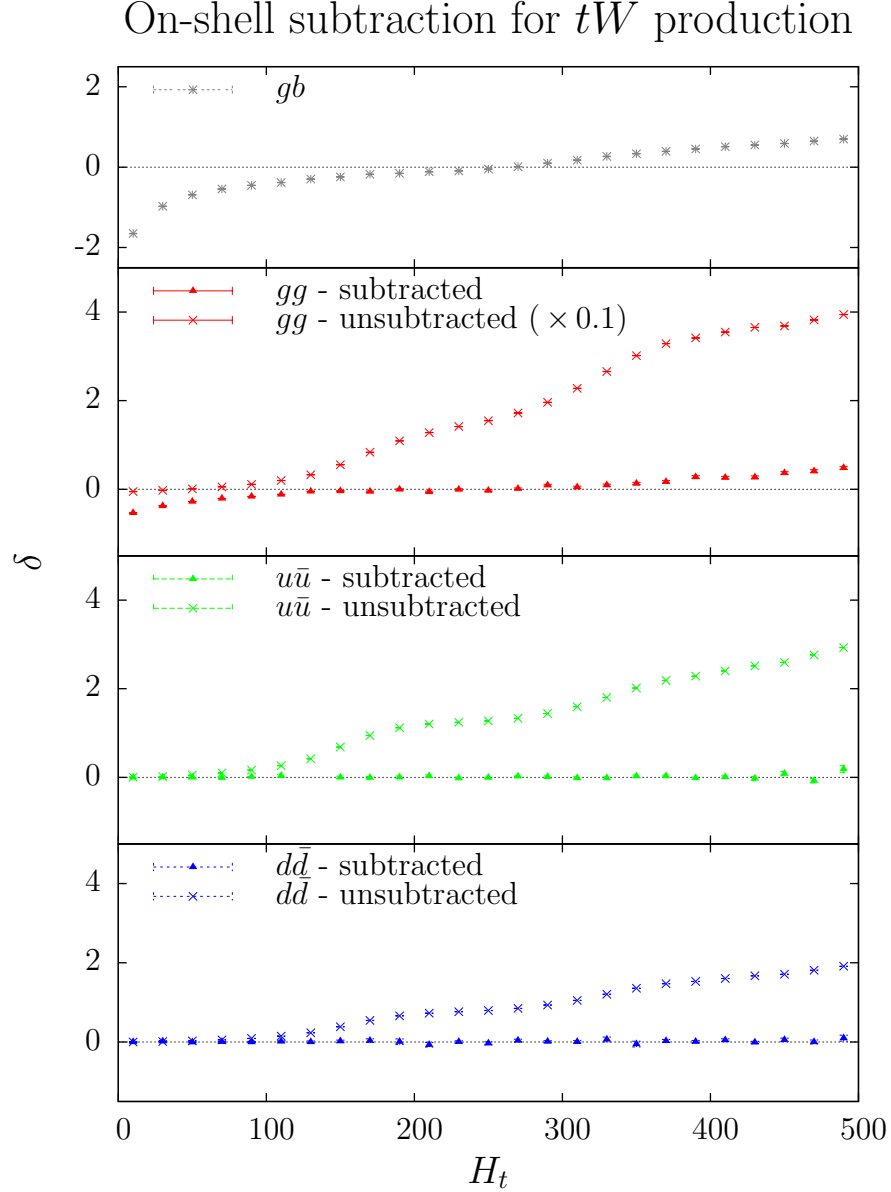


**Figure 7.13.:** The correction factors for a selection of subprocesses which contribute to the real emission QCD NLO correction to  $pp \rightarrow tW^-$ , plotted as a function of  $H_t$ , the sum of transverse energies. The correction factor,  $\delta$  is given by the real-emission NLO correction, over the leading order contribution. The partonic subprocesses are labelled according to their initial state partons. For the subprocesses  $gg \rightarrow tW^- \bar{b}$ ,  $u\bar{u} \rightarrow tW^- \bar{b}$  and  $d\bar{d} \rightarrow tW^- \bar{b}$ , on-shell subtraction is required to prevent double counting of the contribution due to an on-shell anti-top decay ( $\bar{t} \rightarrow W^- \bar{b}$ ). For these processes, the unsubtracted contribution is shown (computed using the physical top width), as well as the subtracted contribution (computed using a width  $\Gamma_t = 0.00001m_t$ ).

	Cross Section [pb]	Statistical Error [pb]
SHERPA + MCFM	808.14	0.08
MCFM native	808.01	0.18

**Table 7.1.:** Comparison of the QCD NLO cross section from SHERPA using interfaced MCFM loop code and MCFM standalone for  $t\bar{t}$  production at the LHC with a centre of mass energy of 14 TeV, using the CTEQ6m PDF set, with  $\mu_R = \mu_F = m_t = 175$  GeV. Agreement is better than per mille, and within statistical errors.

degree of cross checking at the level of a single phase space point. Also, the subtraction terms for the real-emission part offer far less scope for implementational idiosyncrasy and may easily be cross checked by phase space point. Where possible, these cross checks have been performed against available code, such as MadDipole [68, 69] for the massive QCD dipoles, SuperAutoDipole [73] for the SUSY-QCD dipoles, and RADY [98] for the photonic dipoles.

For the case of the on-shell subtraction, phase space point comparison would only be available for identical reshuffling schemes. However, integrated results were compared with a similar implementation within the automated MadGolem framework [144], and agreement was found.

## 7.4. First Physical Applications

Due to the modularity of the NLO calculation, and as described in detail in Chapter 2, the loop part of an NLO calculation may be provided by an external program interfaced to SHERPA. This may be achieved using the Binoth Les Houches Accord interface, or, if the loop code does not provide this option, a customised interface may be employed.

The MCFM code [149] does not currently provide a standard BLHA interface to allow external programs to use their one-loop matrix elements. However, SHERPA may be interfaced to MCFM one-loop amplitudes manually, to provide full NLO QCD calculations. An interface to MCFM’s one-loop  $t\bar{t}$  production amplitude, has provided a simple test case and first physical application for SHERPA’s massive QCD dipoles. Better than per-mille agreement was found, when results were compared to native MCFM cross sections, as can be seen in Table 7.1. Distributions were also compared, and examples of these are shown in Figures 7.14 and 7.15.

Also, the one-loop matrix elements for s- and t-channel single top production have been implemented within the SHERPA framework, following the calculation of reference [150]. Cross section results using this implementation and SHERPA’s massive dipole subtraction have been compared to results from reference [151], and the results agreed to better than 0.4%, which is within the quoted statistical error.

SHERPA’s photonic dipoles have been used to calculate corrections to neutral current Drell-Yan at the LHC, using one-loop amplitudes from RADY [98], linked to SHERPA through the Binoth Les Houches Accord interface [152]. Results have been compared with those produced using a standalone version of RADY, which uses an internal dipole subtraction implementation. Better than per-mille agreement was found. Figures 7.16, 7.17 and 7.18 show distributions from this comparison.

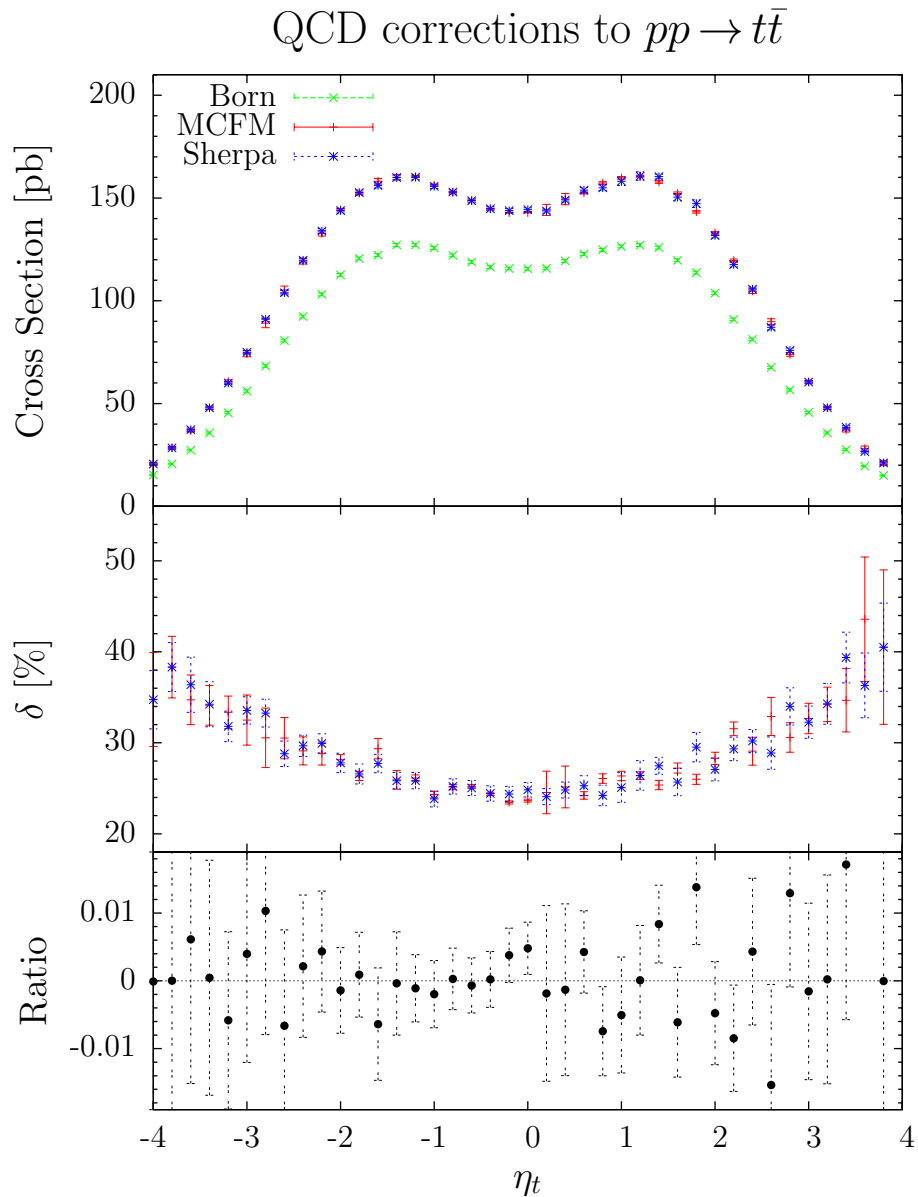


**Figure 7.14.:** Example distribution from the comparison of QCD NLO results obtained from SHERPA using interfaced MCFM loop code and MCFM standalone for  $t\bar{t}$  production.  $\delta$  is defined as  $\frac{\sigma_{NLO}}{\sigma_{LO}}$ , and the ratio is  $\frac{\sigma_{NLO}^{Sherpa} - \sigma_{NLO}^{MCFM}}{\sigma_{NLO}^{Sherpa} + \sigma_{NLO}^{MCFM}}$ .

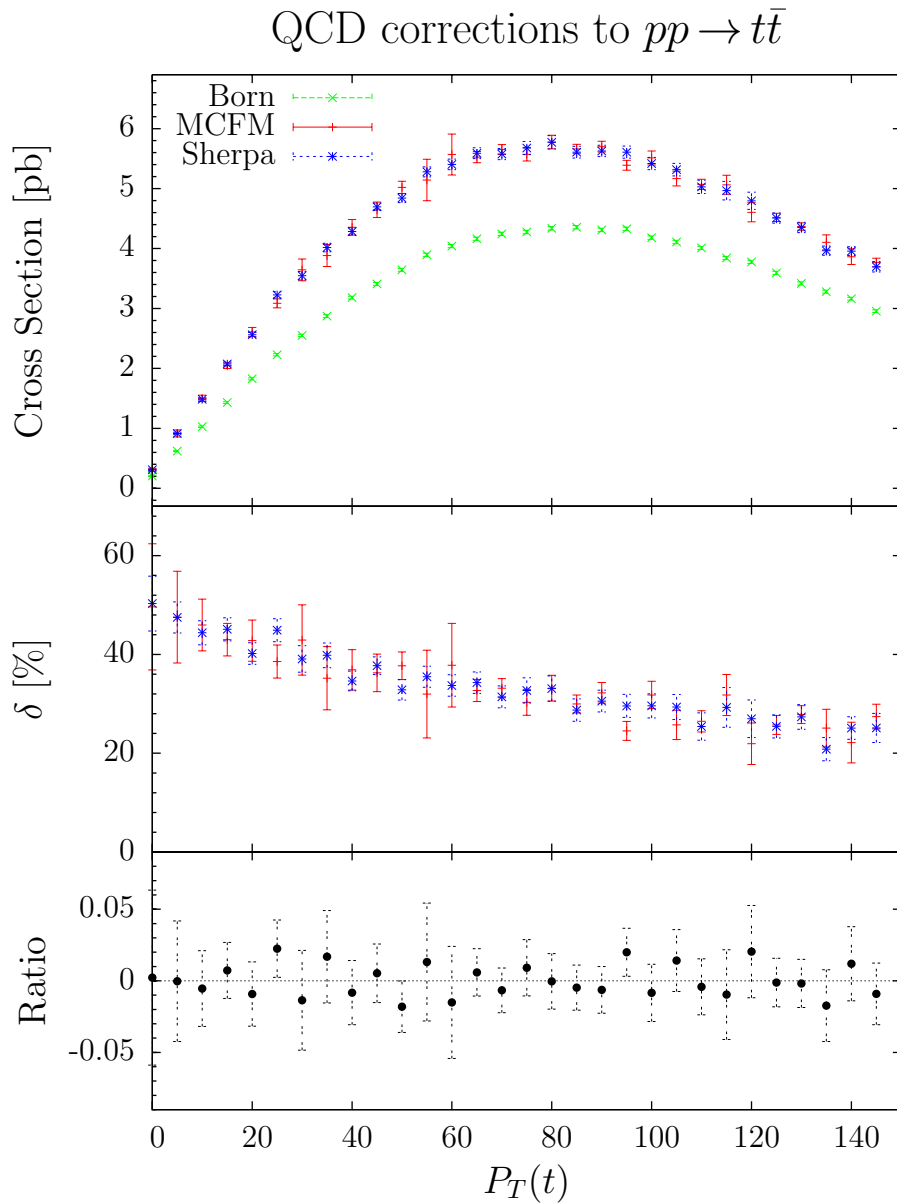


**Figure 7.15.:** Example distribution from the comparison of QCD NLO results obtained from SHERPA using interfaced MCFM loop code and MCFM standalone for  $t\bar{t}$  production.  $\delta$  is defined as  $\frac{\sigma_{NLO}}{\sigma_{LO}}$ , and the ratio is  $\frac{\sigma_{NLO}^{Sherpa} - \sigma_{NLO}^{MCFM}}{\sigma_{NLO}^{Sherpa} + \sigma_{NLO}^{MCFM}}$ .

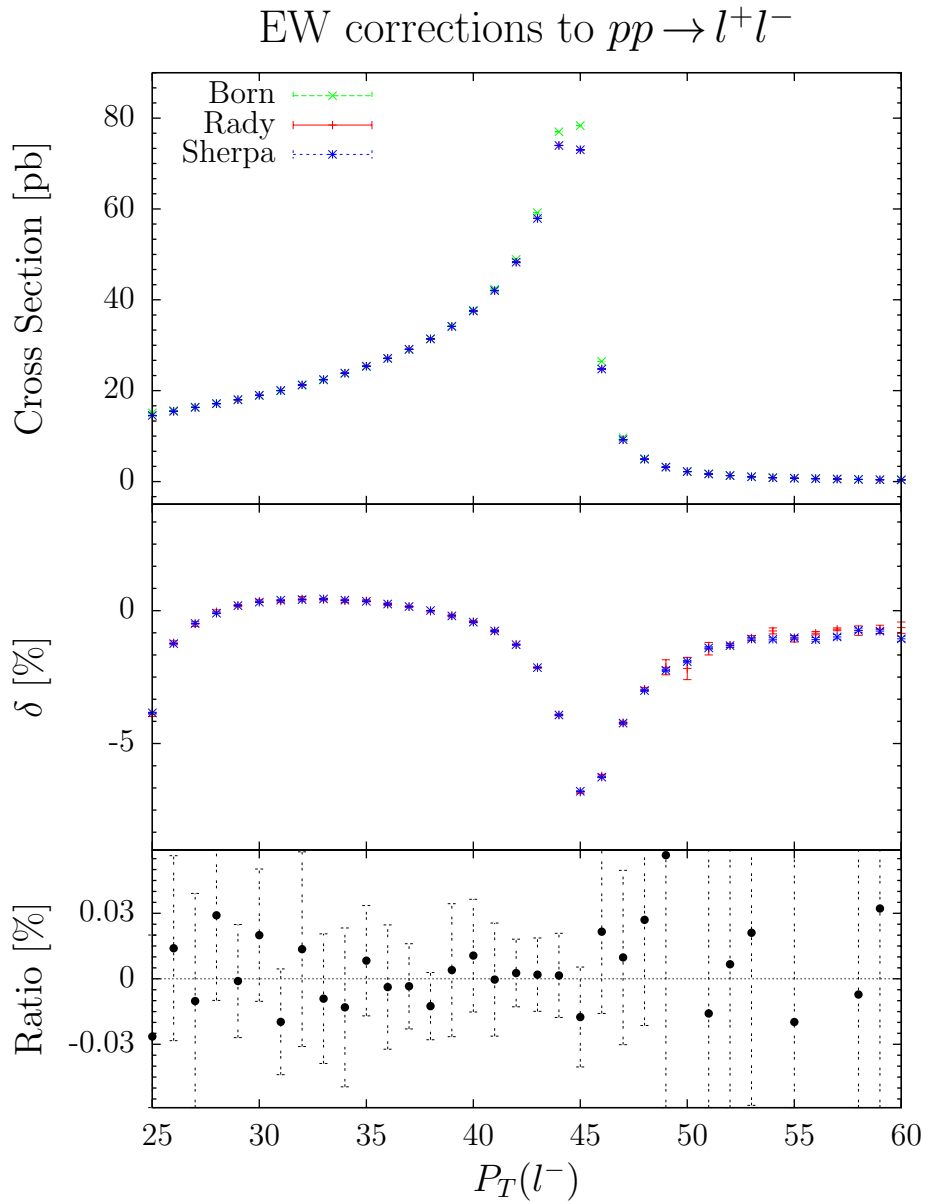


**Figure 7.16.:** Example distribution from the comparison of EW NLO results obtained from SHERPA using RADY loop code connected via the Binoth Les Houches Accord interface, and RADY standalone for  $pp \rightarrow l^+l^-$ .  $\delta$  is defined as  $\frac{\sigma_{NLO}}{\sigma_{LO}}$ , and the ratio is  $\frac{\sigma_{NLO}^{Sherpa} - \sigma_{NLO}^{Rady}}{\sigma_{NLO}^{Sherpa} + \sigma_{NLO}^{Rady}}$ .

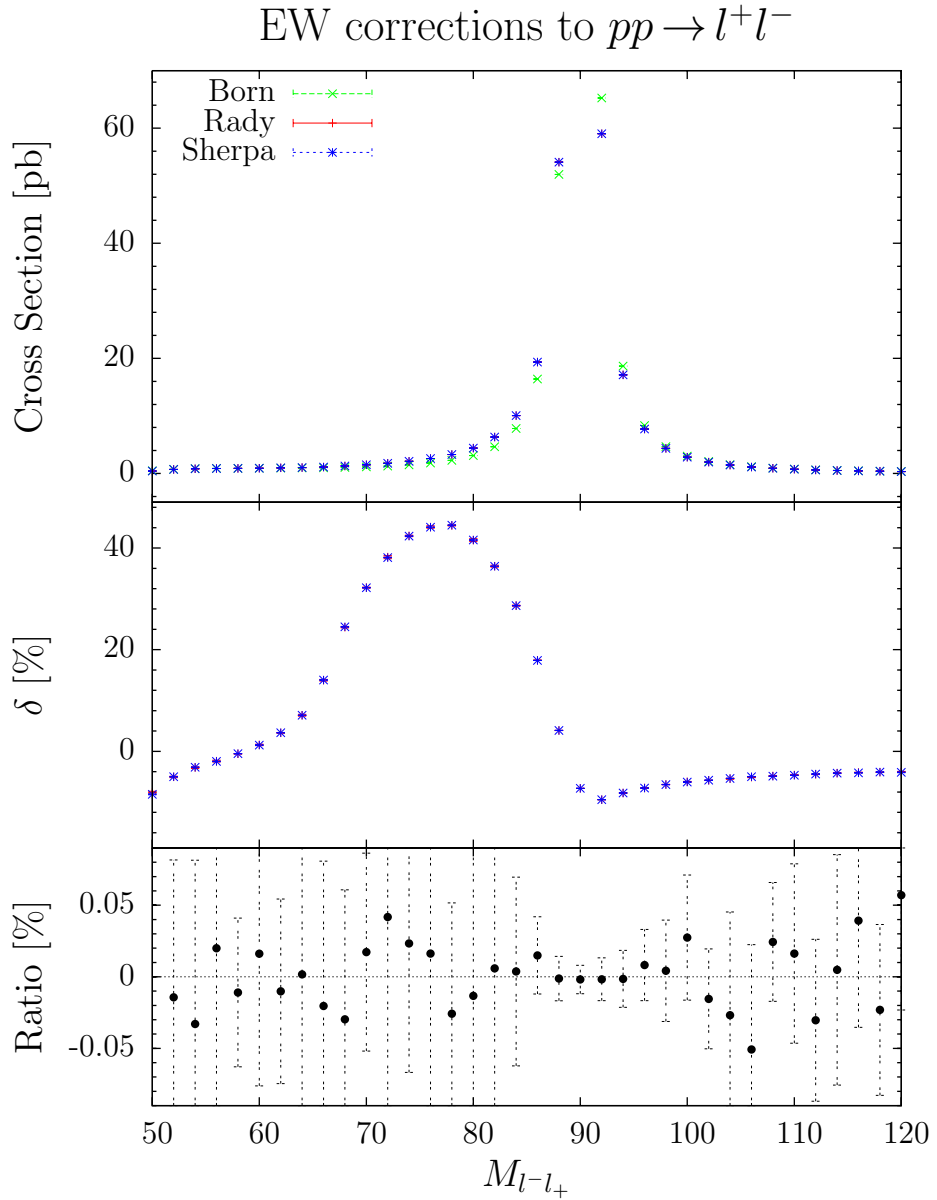


**Figure 7.17.:** Example distribution from the comparison of EW NLO results obtained from SHERPA using RADY loop code connected via the Binoth Les Houches Accord interface, and RADY standalone for  $pp \rightarrow l^+l^-$ .  $\delta$  is defined as  $\frac{\sigma_{NLO}}{\sigma_{LO}}$ , and the ratio is  $\frac{\sigma_{NLO}^{Sherpa} - \sigma_{NLO}^{Rady}}{\sigma_{NLO}^{Sherpa} + \sigma_{NLO}^{Rady}}$ .

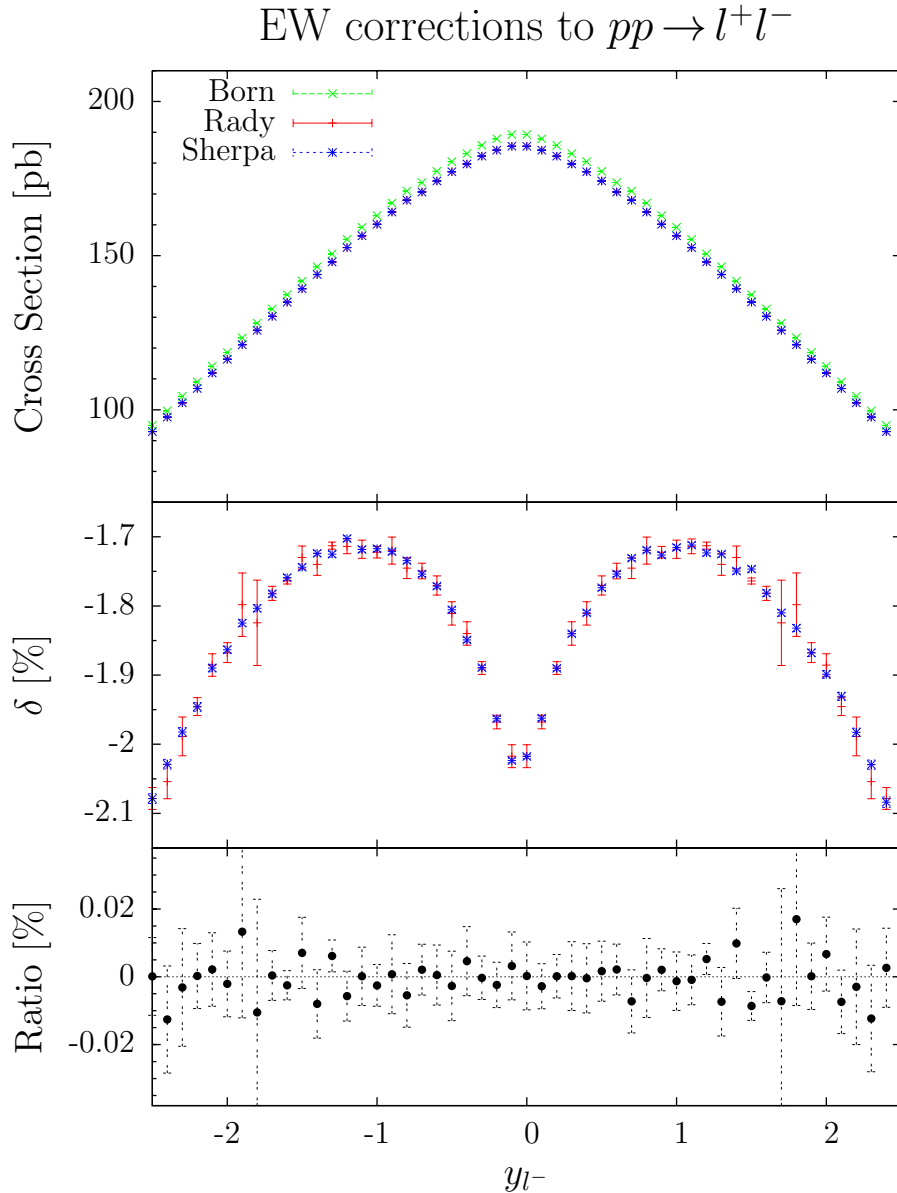


**Figure 7.18.:** Example distribution from the comparison of EW NLO results obtained from SHERPA using RADY loop code connected via the Binoth Les Houches Accord interface, and RADY standalone for  $pp \rightarrow l^+l^-$ .  $\delta$  is defined as  $\frac{\sigma_{NLO}}{\sigma_{LO}}$ , and the ratio is  $\frac{\sigma_{NLO}^{Sherpa} - \sigma_{NLO}^{Rady}}{\sigma_{NLO}^{Sherpa} + \sigma_{NLO}^{Rady}}$ .

# Chapter 8.

## Summary

The extension of general-purpose Monte Carlo event generators to full NLO accuracy has become the main goal for many within the Monte Carlo community over the past few years. The driving force behind this advance is the expected abundance of data from the LHC experiments, leading to experimental accuracy for which leading order theory calculations are insufficient.

For many years, the limiting factor in NLO advances has been the calculation of the one-loop matrix element, which has required slow and laborious analytical work on a process-by-process basis. However, the first results are now available from automated one-loop codes, which have the potential to revolutionise the NLO industry. Moreover, the modularity of NLO calculations and the introduction of a standard interface between one-loop codes and Monte Carlos, detailed in the Binoth Les Houches Accord, has opened the door for Monte Carlo event generators to perform NLO calculations without the necessity of calculating the one-loop matrix elements internally. The first implementation of a Binoth Les Houches Accord interface for electroweak NLO calculations was presented in Chapter 2 of this thesis. This interface allows a SHERPA user to connect code for calculating one-loop matrix elements, and the additional settings and parameters required for electroweak calculations were examined in detail.

From the Monte Carlo point of view, the first steps on the road to general-purpose Monte Carlo NLO automation were taken only four years ago, with the first automated framework for the subtraction of NLO soft and collinear singularities, implemented in AMEGIC++ for massless QCD [66]. Since then, there have been several other groups with similar success in automation of IR subtraction [67–73]. This thesis documented the extension of the implementation of Catani-Seymour dipole subtraction in AMEGIC++ to include dipoles involving massive QCD partons (Chapter 4). This extension not only

allows NLO treatment of massive Standard Model quarks, but also paves the way for NLO calculations with additional Beyond the Standard Model coloured particles. An example of such a theory was studied in Chapter 5, where the implementation of dipoles involving supersymmetric particles was discussed. The complications due to on-shell intermediate particles, as relevant for NLO processes with massive final states, were also addressed.

Of course QCD is only one of the fundamental particle interactions, and calculations may also be performed at NLO in the electroweak coupling. To facilitate these calculations photonic dipole functions which subtract the IR singularities due to soft or collinear photons were also implemented, as detailed in Chapter 6.

As such, in this thesis, a full framework for the calculation of NLO cross sections within the Monte Carlo event generator SHERPA was presented. This framework provides all the necessary tools to perform NLO calculations, once the user has provided code for the relevant one-loop matrix element.

The benefits of Monte Carlo integration for NLO cross sections are clear: numerical integration allows the implementation of non-trivial phase space cuts and arbitrarily complicated observables. Moreover, a multi-purpose SHERPA NLO framework provides a user-friendly, flexible, reliable, optimised tool for NLO calculations.

This NLO groundwork in SHERPA is also an essential foundation on which a full NLO event generation framework is already being built. The implementation of automated POWHEG-like NLO event generation and showering is well underway[32]. Even the next step, automated CKKW-like NLO multijet matrix element and parton shower merging, known as MENLOPS, is within reach [34].

With the help of the framework for NLO calculations presented in this thesis, the event generator SHERPA is well on the way to becoming a fully automated multipurpose NLO event generator, suitable for the comparison of theory with the precision data expected from the LHC.

# Appendix A.

## Massive QCD dipoles

In the following section, the modifications to the integrated dipole terms for the inclusion of a phase space restriction parameter are summarised. These equations were originally derived in references [69, 109–111]. For reference, these equations have been collected together here, and their notation standardised.

### A.1. Notation

It is useful to introduce some common notation for the following formulae. Following the standard convention, the phase space restriction parameter shall be denoted by  $\alpha$ . The masses are rescaled, following reference [101], as shown in Table A.1.

For the final-final dipoles, the endpoint of the  $y_{ij,k}$  integral is given by

$$y_+ = 1 - \frac{2\mu_k(1 - \mu_k)}{1 - \mu_i^2 - \mu_j^2 - \mu_k^2} , \quad (\text{A.1})$$

Dipole type	Definition of $\mu_n$	Location of definition in [101]
Final-final	$\mu_n = \frac{m_n}{\sqrt{Q^2}}$	Eq. (5.5)
Final-initial	$\mu_n = \frac{m_n}{\sqrt{2\tilde{p}_{ij}p_a}}$	Eq. (5.45)
Initial-final	$\mu_n = \frac{m_n}{\sqrt{2\tilde{p}_j p_a}}$	Eq. (5.77)

**Table A.1.:** Definition of rescaled masses for each relevant dipole type.

and for the initial-final dipoles, the endpoint of the  $z$  integration is given by

$$z_+(x) = \frac{1-x}{1-x+\mu_j^2}. \quad (\text{A.2})$$

For the final-initial dipoles, the ‘+’-distributions are modified by the inclusion of the phase space cut. The modified ditribution is similarly defined by its action on a test function,  $f(x)$ ,

$$\int_0^1 dx f(x) \left( \frac{1}{1-x} \right)_{1-\alpha} = \int_{1-\alpha}^1 dx \frac{(f(x) - f(1))}{1-x}, \quad (\text{A.3})$$

and it can be seen that the unmodified ‘+’-distribution is recovered in the limit  $\alpha = 1$ .

## A.2. Final-final

Massive dipole terms are required for final-final splittings if one or more of the emitter,  $i$ , the unresolved parton  $j$ , and the spectator  $k$ , are massive. Listed below are the modifications for the integrated dipole terms due to the phase space restriction for final-final massive dipole splittings.

### A.2.1. $Q \rightarrow Q \ g$

#### Massive spectator

The dipole modifications for this configuration were given in reference [110]. The phase space restriction was implemented using a cut of the form

$$\Theta(y_{ij,k} < \alpha). \quad (\text{A.4})$$

However, the SHERPA implementation, similar to the implementation of reference [69], uses the phase space cut

$$\Theta(y_{ij,k} < \alpha y_+), \quad (\text{A.5})$$

where  $y_+$  is the original upper kinematical limit of the  $y_{ij,k}$  integral. This choice of cut definition allows the  $\alpha$  parameter to vary in the range  $0 < \alpha \leq 1$ , rather than the range  $0 < \alpha \leq y_+$ . This change of definition is easily applied to the equations from reference [110], by the replacement  $\alpha \rightarrow \alpha y_+$ . The equations given below follow the SHERPA convention.

The one-particle phase space integration of the dipole subtraction terms may be split into two parts, one containing the eikonal, or soft, divergence, and one containing the collinear. The modifications for the phase space restriction may be similarly separated. For this splitting, the resulting structure is

$$\Delta I_{gQ,k}(\mu_j, \mu_k; \alpha) = C_F \left[ 2\Delta I^{\text{eik}}(\mu_j, \mu_k; \alpha) + \Delta I_{gQ,k}^{\text{coll}}(\mu_j, \mu_k; \alpha) \right]. \quad (\text{A.6})$$

The eikonal contribution is flavour and spin independent, and, for the general case of non-zero masses for the emitter and spectator, is given by

$$\begin{aligned} \Delta I^{\text{eik}}(\mu_j, \mu_k; \alpha) = & \frac{1}{v_{jk}} \left( -\text{Li}_2 \left( \frac{a+x}{a+x_+} \right) + \text{Li}_2 \left( \frac{a}{a+x_+} \right) + \text{Li}_2 \left( \frac{x_+ - x}{x_+ - b} \right) \right. \\ & + \text{Li}_2 \left( \frac{c+x}{c+x_+} \right) - \text{Li}_2 \left( \frac{c}{c+x_+} \right) + \text{Li}_2 \left( \frac{x_- - x}{x_- + a} \right) - \text{Li}_2 \left( \frac{x_-}{x_- + a} \right) \\ & - \text{Li}_2 \left( \frac{b-x}{b-x_-} \right) + \text{Li}_2 \left( \frac{b}{b-x_-} \right) - \text{Li}_2 \left( \frac{x_- - x}{x_- + c} \right) + \text{Li}_2 \left( \frac{x_-}{x_- + c} \right) \\ & + \text{Li}_2 \left( \frac{b-x}{b+a} \right) - \text{Li}_2 \left( \frac{b}{b+a} \right) - \text{Li}_2 \left( \frac{c+x}{c-a} \right) + \text{Li}_2 \left( \frac{c}{c-a} \right) - \text{Li}_2 \left( \frac{x_+}{x_+ - b} \right) \\ & + \log(c+x) \log \left( \frac{(a-c)(x_+ - x)}{(a+x)(c+x_+)} \right) - \log(c) \log \left( \frac{(a-c)x_+}{a(c+x_+)} \right) \\ & + \log(b-x) \log \left( \frac{(a+x)(x_- - b)}{(a+b)(x_- - x)} \right) - \log(b) \log \left( \frac{a(x_- - b)}{(a+b)x_-} \right) \\ & - \log((a+x)(b-x_+)) \log(x_+ - x) + \log(a(b-x_+)) \log(x_+) \\ & + \log(d) \log \left( \frac{(a+x)x_+x_-}{a(x_+ - x)(x_- - x)} \right) + \log \left( \frac{x_- - x}{x_-} \right) \log \left( \frac{c+x_-}{a+x_-} \right) \\ & \left. + \frac{1}{2} \log \left( \frac{a+x}{a} \right) \log(a(a+x)(a+x_+)^2) \right), \end{aligned} \quad (\text{A.7})$$

where

$$\begin{aligned}
 a &= \frac{2\mu_k}{1 - \mu_j^2 - \mu_k^2}, \\
 b &= \frac{2(1 - \mu_k)}{1 - \mu_j^2 - \mu_k^2}, \\
 c &= \frac{2\mu_k(1 - \mu_k)}{1 - \mu_j^2 - \mu_k^2}, \\
 d &= \frac{1}{2}(1 - \mu_j^2 - \mu_k^2),
 \end{aligned} \tag{A.8}$$

and

$$\begin{aligned}
 x_{\pm} &= \frac{(1 - \mu_k)^2 - \mu_j^2 \pm \sqrt{\lambda(1, \mu_j^2, \mu_k^2)}}{1 - \mu_j^2 - \mu_k^2}, \\
 v_{jk} &= \frac{\sqrt{\lambda(1, \mu_j^2, \mu_k^2)}}{1 - \mu_j^2 - \mu_k^2},
 \end{aligned} \tag{A.9}$$

with  $\lambda$  representing the standard Källen function

$$\lambda(x, y, z) = x^2 + y^2 + z^2 - 2xy - 2xz - 2yz, \tag{A.10}$$

and  $x$  denoting a reparameterisation of  $\alpha$

$$x = y_+ - \alpha y_+ + \sqrt{(y_+ - \alpha y_+) \left( \frac{1}{y_+} - \alpha y_+ + \frac{4\mu_j^2 \mu_k^2}{(\mu_j^2 - (1 - \mu_k)^2)(1 - \mu_j^2 - \mu_k^2)} \right)}. \tag{A.11}$$

The collinear contribution for this configuration is given by

$$\begin{aligned}
 \Delta I_{gQ,k}^{\text{coll}}(\mu_j, \mu_k; \alpha) &= \frac{3}{2}(1 + \alpha y_+) + \frac{1}{1 - \mu_k} - \frac{2(2 - 2\mu_j^2 - \mu_k)}{1 - \mu_j^2 - \mu_k^2} \\
 &+ \frac{(1 - \alpha y_+) \mu_j^2}{2(\mu_j^2 + \alpha y_+(1 - \mu_j^2 - \mu_k^2))} - 2 \log \left( \frac{\alpha y_+(1 - \mu_j^2 - \mu_k^2)}{(1 - \mu_k)^2 - \mu_j^2} \right) \\
 &+ \frac{1 + \mu_j^2 - \mu_k^2}{2(1 - \mu_j^2 - \mu_k^2)} \log \left( \frac{\mu_j^2 + \alpha y_+(1 - \mu_j^2 - \mu_k^2)}{(1 - \mu_k)^2} \right).
 \end{aligned} \tag{A.12}$$

### Massless spectator

As above, the modifications may be separated into the eikonal and collinear contributions,

$$\Delta I_{gQ,k}(\mu_j, 0; \alpha) = C_F \left[ 2\Delta I^{\text{eik}}(\mu_j, 0; \alpha) + \Delta I_{gQ,k}^{\text{coll}}(\mu_j, 0; \alpha) \right], \quad (\text{A.13})$$

where the eikonal term is the limit of equation (A.7), for  $\mu_k \rightarrow 0$ , given by

$$\Delta I^{\text{eik}}(\mu_j, 0; \alpha) = -\ln(\alpha) \ln(\mu_j^2) - \text{Li}_2\left(\frac{\mu_j^2 - 1}{\mu_j^2}\right) + \text{Li}_2\left(\frac{\alpha(\mu_j^2 - 1)}{\mu_j^2}\right), \quad (\text{A.14})$$

and the collinear contribution for this configuration is

$$\begin{aligned} \Delta I_{gQ,k}^{\text{coll}}(\mu_j, 0; \alpha) = & \frac{\phi}{2} \left[ 3(\alpha - 1) - \frac{(3 - \mu_j^2)}{(1 - \mu_j^2)} \ln(\alpha + (1 - \alpha)\mu_j^2) - \frac{\alpha}{(\alpha + (1 - \alpha)\mu_j^2)} + 1 \right] \\ & - 2\ln(\alpha) + 2\frac{\ln(\alpha + (1 - \alpha)\mu_j^2)}{(1 - \mu_j^2)}. \end{aligned} \quad (\text{A.15})$$

### A.2.2. $q \rightarrow q \ g$

#### Massive spectator

Again, the calculation may be separated into eikonal and collinear contributions,

$$\Delta I_{gq,k}(0, \mu_k; \alpha) = C_F \left[ 2\Delta I^{\text{eik}}(0, \mu_k; \alpha) + \Delta I_{gq,k}^{\text{coll}}(0, \mu_k; \alpha) \right] \quad (\text{A.16})$$

where the eikonal term is the limit of equation (A.7), for  $\mu_j \rightarrow 0$ , given by

$$\begin{aligned} \Delta I^{\text{eik}}(0, \mu_k; \alpha) = & \frac{1}{2} \ln^2 \left( \frac{1 - y_+^2 + 2x_+y_+}{(1 + y_+ - x_+)(1 - y_+ + x_+)} \right) - \ln^2 \left( \frac{1 + y_+ - x_+}{1 + y_+} \right) \\ & + 2 \left[ \ln \left( \frac{1 + y_+}{2} \right) \ln \left( \frac{1 - y_+ + x_+}{1 - y_+} \right) + \ln \left( \frac{1 + y_+}{2y_+} \right) \ln \left( \frac{1 - y_+^2 + 2x_+y_+}{1 - y_+^2} \right) \right. \\ & + \text{Li}_2 \left( \frac{1 - y_+}{1 + y_+} \right) - \text{Li}_2 \left( \frac{1 - y_+^2 + 2x_+y_+}{(1 + y_+)^2} \right) \\ & \left. + \text{Li}_2 \left( \frac{1 - y_+ + x_+}{2} \right) - \text{Li}_2 \left( \frac{1 - y_+}{2} \right) \right], \end{aligned} \quad (\text{A.17})$$

and the collinear contribution for this configuration is

$$\Delta I_{gq,k}^{\text{coll}}(0, \mu_k; \alpha) = -\frac{3}{2} \left[ \ln(\alpha) + y_+(1 - \alpha) \right], \quad (\text{A.18})$$

where

$$x_+ = y_+(1 - \alpha) + \sqrt{(1 - \alpha)(1 - \alpha y_+^2)}. \quad (\text{A.19})$$

### A.2.3. $g \rightarrow g \ g$

#### Massive spectator

Again, the calculation may be separated into eikonal and collinear contributions,

$$\Delta I_{gg,k}(0, \mu_k; \alpha) = 2C_A \left[ 2\Delta I^{\text{eik}}(0, \mu_k; \alpha) + \Delta I_{gg,k}^{\text{coll}}(0, \mu_k; \alpha) \right]. \quad (\text{A.20})$$

The eikonal part is given by equation (A.17), and the collinear part is given by

$$\begin{aligned} \Delta I_{gg,k}(0, \mu_k; \alpha) = & -\frac{11}{6} \left( \frac{1 - \mu_k - \alpha y_+(1 + \mu_k)}{1 + \mu_k} + \log \left( \frac{\alpha y_+(1 + \mu_k)}{1 - \mu_k} \right) \right) \\ & - \left( \kappa - \frac{2}{3} \right) \frac{\mu_k^2}{1 - \mu_k^2} \log \left( \frac{(1 - \alpha y_+)(1 + \mu_k)}{2\mu_k} \right). \end{aligned} \quad (\text{A.21})$$

Again, as in Section A.2.1, the formulae for this splitting were derived in reference [110] for the phase space cut  $\Theta(y_{ij,k} < \alpha)$ . The formulae listed here use the phase space cut  $\Theta(y_{ij,k} < \alpha y_+)$ .

### A.2.4. $g \rightarrow Q \bar{Q}$

#### Massive spectator

The modifications to the integrated dipole terms due to the phase space cut for this configuration are

$$\begin{aligned} \Delta I_{Q\bar{Q},k}(\mu_j, \mu_k; \alpha) = & -\frac{T_R}{3ca^2bd} \left\{ bd \left( -c(3c - 4\mu_j^2 + 2) \log \frac{\alpha c y_+ + d}{c y_+ + b} \right. \right. \\ & 2(e^2 + 2c + 4\mu_j^2) \left( \log \left( \frac{\alpha c^2 y_+ - de - 4\mu_j^4}{c^2 y_+ - be - 4\mu_j^4} \right) - a \log \frac{1 - \alpha y_+}{1 - y_+} \right) \\ & + 2(c(c - 2) - 2\mu_j^2(1 - 2\mu_j^2)) \left( \tan^{-1} \left( \frac{2\mu_j^2}{d} \right) - \tan^{-1} \left( \frac{2\mu_j^2}{b} \right) \right) \\ & \left. \left. + c^3 y_+^2 (\alpha^2 b - d) + 2c^2 y_+ a (\alpha b - d) + 4\mu_j^2(1 - c)(b - d) \right\} , \quad (\text{A.22}) \right. \end{aligned}$$

where we have defined

$$\begin{aligned} a &= \sqrt{1 - \mu_k^2} \\ b &= \sqrt{c^2 y_+^2 - 4\mu_j^2} \\ c &= -1 + 2\mu_j^2 + \mu_k^2 \\ d &= \sqrt{\alpha^2 c^2 y_+^2 - 4\mu_j^2} \\ e &= \sqrt{c^2 - 4\mu_j^4} . \end{aligned} \quad (\text{A.23})$$

#### Massless spectator

The limit of the case above for a massless spectator gives

$$\begin{aligned} \Delta I_{Q\bar{Q},k}(\mu_j, 0; \alpha) = & -\frac{2T_R}{3} \left( (1 - 2\mu_j^2) \log \frac{f - \alpha(1 - 2\mu_j^2)}{g + 1 - 2\mu_j^2} - \frac{2f}{2(1 - \alpha)\mu_j^2 + \alpha} + f + g \right. \\ & \left. + 2(1 - 2\mu_j^2) \left( \tan^{-1} \left( \frac{2\mu_j^2}{g} \right) - \tan^{-1} \left( \frac{2\mu_j^2}{f} \right) \right) \right) , \quad (\text{A.24}) \end{aligned}$$

where we have defined

$$\begin{aligned} f &= \sqrt{\alpha^2(1 - 2\mu_j^2)^2 - 4\mu_j^4} \\ g &= \sqrt{1 - 4\mu_j^2} . \end{aligned}$$

### A.2.5. $g \rightarrow q \bar{q}$

#### Massive spectator

The contribution due to a  $g \rightarrow q \bar{q}$  splitting consists of only a collinear contribution,

$$\Delta I_{q\bar{q},k}(0, \mu_k; \alpha) = T_R \Delta I_{q\bar{q},k}^{\text{coll}}(0, \mu_k; \alpha) , \quad (\text{A.25})$$

which is given by

$$\begin{aligned} \Delta I_{q\bar{q},k}(0, \mu_k; \alpha) &= \frac{2}{3} \left( \frac{1 - \mu_k - \alpha y_+ (1 + \mu_k)}{1 + \mu_k} + \log \left( \frac{\alpha y_+ (1 + \mu_k)}{1 - \mu_k} \right) \right) \\ &\quad + \left( \kappa - \frac{2}{3} \right) \frac{2\mu_k^2}{1 - \mu_k^2} \log \left( \frac{(1 - \alpha y_+) (1 + \mu_k)}{2\mu_k} \right) . \end{aligned} \quad (\text{A.26})$$

Again, as in Section A.2.1, the formulae for this splitting were derived in reference [110] for the phase space cut  $\Theta(y_{ij,k} < \alpha)$ . The formulae listed here use the phase space cut  $\Theta(y_{ij,k} < \alpha y_+)$ .

## A.3. Final-Initial

As massive particles are restricted to the final state, the initial state spectators in final-initial dipoles are by definition massless. Therefore, massive final-initial dipoles must involve massive final state partons.

### A.3.1. $Q \rightarrow Q \ g$

$$J_{gQ}^{a\delta}(\mu, \alpha) = 2 \ln(\alpha) \left[ \ln \left( \frac{1+\tilde{\mu}^2}{\tilde{\mu}^2} \right) - 1 \right] \quad (\text{A.27})$$

$$J_{gQ}^{a+}(x, \mu, \alpha) = \left[ \ln \left( \frac{1+\tilde{\mu}^2}{\tilde{\mu}^2} \right) - 1 \right] \left( \frac{2}{1-x} \right)_{1-\alpha} \quad (\text{A.28})$$

$$\begin{aligned} [J_{gQ}^{aR}(x, \mu, \alpha)] = & -\Theta(-x+1-\alpha) \left\{ \frac{1-x}{2(1-x+\mu^2)^2} \right. \\ & \left. + \frac{2}{(1-x)} \ln \left( \frac{(2-x+\mu^2) \tilde{\mu}^2}{(1+\tilde{\mu}^2)(1-x+\mu^2)} \right) \right\} \end{aligned} \quad (\text{A.29})$$

where we have defined  $\tilde{\mu}^2 = \mu^2/x$ .

### A.3.2. $g \rightarrow Q \ \bar{Q}$

$$[J_{Q\bar{Q}}^a(x, \mu_Q, \alpha)]_{x_+} = \frac{2}{3} \left( \frac{1-x+2\mu_Q^2}{(1-x)^2} \sqrt{1 - \frac{4\mu_Q^2}{1-x}} \right)_{1-\alpha}, \quad (\text{A.30})$$

where we define:

$$\int_0^1 dx \ f(x) (g(x))_{1-\alpha} = \int_{1-\alpha}^1 dx \ g(x) (f(x) - f(1)) \quad (\text{A.31})$$

The non-singular terms  $J_{Q\bar{Q}}^{a;\text{NS}}(\mu_Q)$  receive:

$$\Delta J_{Q\bar{Q}}^{a;\text{NS}}(\mu_Q, \alpha) = \frac{2}{9a} (5 - 16\mu_Q^2(1 + \mu_Q^2)) - \frac{2b}{9c\alpha} (5\alpha + 4\mu_Q^2) + \frac{4}{3} \log\left(\frac{b+c}{a+1}\right). \quad (\text{A.32})$$

where we define:

$$\begin{aligned} a &= \sqrt{1 - 4\mu_Q^2} \\ b &= \sqrt{\alpha - 4\mu_Q^2} \\ c &= \sqrt{\alpha}. \end{aligned} \quad (\text{A.33})$$

## A.4. Initial-final

Similarly to the final-initial dipoles, the massive partons in initial-final dipoles must be in the final state. Thus for each of the modifications listed below, the final state spectator is taken to be massive.

### A.4.1. $\widetilde{ai} : q, a : q, i : g$

$$\begin{aligned} \Delta I_Q^{qq}(x, \mu; \alpha) &= -C_F \Theta(z_+ - \alpha) \left\{ \left( \frac{2}{1-x} \right) \log \left( \frac{z_+(1-x+\alpha)}{\alpha(1-x+z_+)} \right) \right. \\ &\quad \left. - (1+x) \ln \left( \frac{z_+}{\alpha} \right) \right\} \end{aligned} \quad (\text{A.34})$$

### A.4.2. $\widetilde{ai} : g, a : q, i : q$

$$\Delta I^{gq}(x, \mu; \alpha) = -T_R \Theta(z_+ - \alpha) \left\{ \left( x^2 + (1-x)^2 \right) \left[ \ln \left( \frac{z_+}{\alpha} \right) \right] \right\} \quad (\text{A.35})$$

### A.4.3. $\widetilde{ai} : q, a : g, i : q$

$$\begin{aligned} \Delta I_Q^{qg}(x, \mu; \alpha) &= -C_F \Theta(z_+ - \alpha) \left\{ \frac{\left( 1 + (1-x)^2 \right)}{x} \left[ \ln \left( \frac{z_+}{\alpha} \right) \right] \right. \\ &\quad \left. + 2\tilde{\mu}^2 \ln \left( \frac{1-z_+}{1-\alpha} \right) \right\} \end{aligned} \quad (\text{A.36})$$

#### A.4.4. $\widetilde{ai} : g, a : g, i : g$

$$\begin{aligned} \Delta I_Q^{gg}(x, \mu; \alpha) &= -C_A \Theta(z_+ - \alpha) \left\{ 2 \left( x(1-x) + \frac{1-x}{x} - 1 \right) + \ln \left( \frac{z_+}{\alpha} \right) \right. \\ &+ \left. 2\tilde{\mu}^2 \ln \left( \frac{1-z_+}{1-\alpha} \right) - \frac{2}{(1-x)} \ln \left( \frac{\alpha(1-x+z_+)}{z_+(1-x+\alpha)} \right) \right\}. \end{aligned} \quad (\text{A.37})$$

### A.5. Organisation of the Calculation

Adapting the notation of references [56, 101], the integrated dipole terms are schematically given by.

$$\begin{aligned} &\sum_{a,b} \int d\eta_1 d\eta_2 f_a(\eta_1, \mu_F^2) f_b(\eta_2, \mu_F^2) \left\{ \int_{m+1} d\sigma_{ab}^A(\eta_1 p, \eta_2 \bar{p}) + \int_m d\sigma_{ab}^C(\eta_1 p, \eta_2 \bar{p}, \mu_F^2) \right\} \\ &= \sum_{a,b} \int d\eta_1 d\eta_2 f_a(\eta_1, \mu_F^2) f_b(\eta_2, \mu_F^2) \left\{ \int_m [d\sigma_{ab}^B(\eta_1 p, \eta_2 \bar{p}) \times \mathbf{I}(\epsilon)] \right. \\ &\quad + \sum_{a'} \int_0^1 dx \int_m [(\mathbf{K}^{a,a'}(x\eta_1 p, x) + \mathbf{P}^{a,a'}(x\eta_1 p, x; \mu_F^2)) \times d\sigma_{a'b}^B(x\eta_1 p, \eta_2 \bar{p})] \\ &\quad \left. + \sum_{b'} \int_0^1 dx \int_m [(\mathbf{K}^{b,b'}(x\eta_2 \bar{p}, x) + \mathbf{P}^{b,b'}(x\eta_2 \bar{p}, x; \mu_F^2)) \times d\sigma_{ab'}^B(\eta_1 p, x\eta_2 \bar{p})] \right\}. \end{aligned} \quad (\text{A.38})$$

where the  $\mathbf{K}$  and  $\mathbf{P}$  terms have a convolution over  $x$ , which is a boost parameter for the associated born momenta.

For the massive case, as well as the explicit dependence on  $x$ , the  $\mathbf{K}$  terms also have a dependence on a kinematic variable,  $\hat{s}$ . This variable is fixed for the  $x$  integration, but is dependent on  $\eta$

$$\hat{s} = \hat{s}(\eta) = 2p_a \tilde{p}_{ij} = 2\eta p \tilde{p}_{ij}, \quad (\text{A.39})$$

and can be identified with the variable  $s_{aj}$  in reference [101].

The  $x$  dependence of the **K** and **P** terms is given schematically by the following distribution:

$$(g(x, \hat{s}(\eta_1)))_+ + \delta(1-x)h + k(x) + \sum_F^{N_F} \left[ \left( g^{x_+^F}(x, \hat{s}(\eta_1)) \right)_{x_+^F} + \delta(x_+^F - x)h^{x_+^F} \right]. \quad (\text{A.40})$$

Here  $h$  is a constant,  $k(x)$  a regular function in  $x$  and  $(g(x, \hat{s}(\eta_1)))_+$  is defined by its action on a generic test function  $a(x)$

$$\int_0^1 dx a(x) (g(x, \hat{s}(\eta_1)))_+ = \int_0^1 dx [a(x) - a(1)] g(x, \hat{s}(\eta_1)). \quad (\text{A.41})$$

The terms under the sum contribute only to the **K** term when splittings of gluons into massive quark flavours are involved in the subtraction:  $N_F$  is the number of possible massive flavours produced in a gluon splitting. The kinematic endpoint  $x_+$  for the splitting of a final state gluon into massive quarks is a function of the kinematic variable  $\hat{s}$ , and is defined as

$$x_+ = 1 - \frac{4m_F^2}{\hat{s}} = 1 - \frac{4m_F^2}{2p_a \tilde{p}_{ij}} = 1 - \frac{4m_F^2}{2\eta p \tilde{p}_{ij}}. \quad (\text{A.42})$$

$h^{x_+^F}$  is a constant in  $x$ , and the distributions  $\left( g^{x_+^F}(x) \right)_{x_+^F}$  are defined analogously to the ‘+’-distribution as

$$\int_0^1 dx a(x) (g(x, \hat{s}(\eta)))_{x_+} = \int_0^1 dx \Theta(x_+ - x) [a(x) - a(x_+)] g(x, \hat{s}(\eta)). \quad (\text{A.43})$$

The integrated dipole contribution from equation (A.38) may be rewritten in terms of the distribution introduced in equation (4.2) giving

$$\begin{aligned}
& \sum_{a,b} \int d\eta_1 d\eta_2 f_a(\eta_1, \mu_F^2) f_b(\eta_2, \mu_F^2) \\
& \int_m \left\{ \mathbf{I}(\epsilon) d\sigma_{ab}^B(\eta_1 p, \eta_2 \bar{p}) \right. \\
& + \sum_{a'} \left[ \int_0^1 dx \left( g^{a,a'}(x, \hat{s}(\eta_1)) \left[ d\sigma_{a'b}^B(x\eta_1 p, \eta_2 \bar{p}) - d\sigma_{a'b}^B(\eta_1 p, \eta_2 \bar{p}) \right] + k^{a,a'}(x) d\sigma_{a'b}^B(x\eta_1 p, \eta_2 \bar{p}) \right. \right. \\
& \left. \left. + \delta^{a,a'} \sum_F g^{x_F^F}(x, \hat{s}(\eta_1)) \Theta(x_+^F - x) \left[ d\sigma_{a'b}^B(x\eta_1 p, \eta_2 \bar{p}) - d\sigma_{a'b}^B(x_+^F \eta_1 p, \eta_2 \bar{p}) \right] \right) \right. \\
& \left. + h^{a,a'} d\sigma_{a'b}^B(\eta_1 p, \eta_2 \bar{p}) + \delta^{a,a'} \sum_F h^{x_F^F} d\sigma_{a'b}^B(x_+^F \eta_1 p, \eta_2 \bar{p}) \right] \\
& + \sum_{b'} \left[ \int_0^1 dx \left( g^{b,b'}(x, \hat{s}(\eta_2)) \left[ d\sigma_{ab'}^B(\eta_1 p, x\eta_2 \bar{p}) - d\sigma_{ab'}^B(\eta_1 p, \eta_2 \bar{p}) \right] + k^{b,b'}(x) d\sigma_{ab'}^B(\eta_1 p, x\eta_2 \bar{p}) \right. \right. \\
& \left. \left. + \delta^{b,b'} \sum_F g^{x_F^F}(x, \hat{s}(\eta_2)) \Theta(x_+^F - x) \left[ d\sigma_{ab'}^B(\eta_1 p, x\eta_2 \bar{p}) - d\sigma_{ab'}^B(\eta_1 p, x_+^F \eta_2 \bar{p}) \right] \right) \right. \\
& \left. + h^{b,b'} d\sigma_{ab'}^B(\eta_1 p, \eta_2 \bar{p}) + \delta^{b,b'} \sum_F h^{x_F^F} d\sigma_{ab'}^B(\eta_1 p, x_+^F \eta_2 \bar{p}) \right] \left. \right\}. \tag{A.44}
\end{aligned}$$

A straightforward implementation of equation (A.44) would require the computation of Born matrix elements for several different initial state flavours and Bjorken- $x$ , for each configuration and phase space point, as given by the outer sum and integrals. However, as the number of external legs increases, the calculation of the matrix elements becomes computationally expensive, with the number of Feynmann diagrams growing factorially with the number of external legs. Therefore, as for the massless dipoles implemented in SHERPA [66], the sums and integrals are reordered such that the Born matrix element can be factored out, requiring only one evaluation per phase space point.

The expression for the integrated dipole contribution may be reorganised to factor out the Born matrix elements by simply reordering the sums over  $a$  and  $a'$  (and  $b$  and  $b'$ ), and rescaling the integration variable  $\eta$ . The value by which the  $\eta$  variable must be scaled depends on the argument of the Born matrix element for each term. The terms may be grouped into three catagories.

Firstly, terms with Born-level kinematics given by the arguments  $(\eta_1 p, \eta_2 \bar{p})$ , require no  $\eta$  rescaling. A simple reordering the sums over  $a$  and  $a'$  allows a common factor of  $d\sigma_{ab}^B(\eta_1 p, \eta_2 \bar{p})$  to be taken out:

$$\begin{aligned}
& \sum_{a,b} \int d\eta_1 d\eta_2 f_a(\eta_1, \mu_F^2) f_b(\eta_2, \mu_F^2) \\
& \quad \int_m \left\{ \mathbf{I}(\epsilon) d\sigma_{ab}^B(\eta_1 p, \eta_2 \bar{p}) \right. \\
& \quad \quad + \sum_{a'} d\sigma_{a'b}^B(\eta_1 p, \eta_2 \bar{p}) \left[ \int_0^1 dx \left( -g^{a,a'}(x, \hat{s}(\eta_1)) \right) + h^{a,a'} \right] \\
& \quad \quad \left. + \sum_{b'} d\sigma_{ab'}^B(\eta_1 p, \eta_2 \bar{p}) \left[ \int_0^1 dx \left( -g^{b,b'}(x, \hat{s}(\eta_2)) \right) + h^{b,b'} \right] \right\} \\
& = \sum_{a,b} \int d\eta_1 d\eta_2 f_a(\eta_1, \mu_F^2) f_b(\eta_2, \mu_F^2) d\sigma_{ab}^B(\eta_1 p, \eta_2 \bar{p}) \\
& \quad \int_m \left\{ \mathbf{I}(\epsilon) \right. \\
& \quad \quad + \sum_{a'} \left[ \int_0^1 dx \frac{f_{a'}(\eta_1, \mu_F^2)}{f_a(\eta_1, \mu_F^2)} \left( -g^{a',a}(x, \hat{s}(\eta_1)) \right) + h^{a',a} \right] \\
& \quad \quad \left. + \sum_{b'} \left[ \int_0^1 dx \frac{f_{b'}(\eta_2, \mu_F^2)}{f_b(\eta_2, \mu_F^2)} \left( -g^{b',b}(x, \hat{s}(\eta_2)) \right) + h^{b',b} \right] \right\}. \quad (\text{A.45})
\end{aligned}$$

Secondly, for those terms with an  $x$  multiplying one of the arguments, i.e.  $(x\eta_1 p, \eta_2 \bar{p})$  or  $(\eta_1 p, x\eta_2 \bar{p})$ , the integration variable is changed to  $\eta' = x\eta$ . The variable is then renamed from  $\eta'$  back to  $\eta$  and the summation over  $a$  and  $a'$  ( $b$  and  $b'$ ) reordered as

before:

$$\begin{aligned}
& \sum_{a,b} \int d\eta_1 d\eta_2 f_a(\eta_1, \mu_F^2) f_b(\eta_2, \mu_F^2) \\
& \int_m \left\{ \sum_{a'} d\sigma_{a'b}^B(x\eta_1 p, \eta_2 \bar{p}) \int_0^1 dx \left( g^{a,a'}(x, \hat{s}(\eta_1)) + k^{a,a'}(x) \right. \right. \\
& \quad \left. \left. + \delta^{a,a'} \sum_F^{N_F} g^{x_+^F}(x, \hat{s}(\eta_1)) \Theta(x_+^F - x) \right) \right. \\
& \quad + \sum_{b'} d\sigma_{ab'}^B(\eta_1 p, x\eta_2 \bar{p}) \int_0^1 dx \left( g^{b,b'}(x, \hat{s}(\eta_2)) + k^{b,b'}(x) \right. \\
& \quad \left. \left. + \delta^{b,b'} \sum_F^{N_F} g^{x_+^F}(x, \hat{s}(\eta_2)) \Theta(x_+^F - x) \right) \right\} \\
& = \sum_{a,b} \int d\eta_1 d\eta_2 f_a(\eta_1, \mu_F^2) f_b(\eta_2, \mu_F^2) d\sigma_{ab}^B(\eta_1 p, \eta_2 \bar{p}) \\
& \int_m \left\{ \sum_{a'} \int_0^1 dx \frac{f_{a'}(\eta_1/x, \mu_F^2)}{x f_a(\eta_1, \mu_F^2)} \left( g^{a',a}(x, \hat{s}(\eta_1/x)) + k^{a',a}(x) \right. \right. \\
& \quad \left. \left. + \delta^{a,a'} \sum_F^{N_F} g^{x_+^F}(x, \hat{s}(\eta_1/x)) \Theta(x_+^F - x) \right) \right. \\
& \quad + \sum_{b'} \int_0^1 dx \frac{f_{b'}(\eta_2/x, \mu_F^2)}{x f_b(\eta_2, \mu_F^2)} \left( g^{b',b}(x, \hat{s}(\eta_2/x)) + k^{b',b}(x) \right. \\
& \quad \left. \left. + \delta^{b,b'} \sum_F^{N_F} g^{x_+^F}(x, \hat{s}(\eta_2/x)) \Theta(x_+^F - x) \right) \right\}. \tag{A.46}
\end{aligned}$$

Lastly, for those terms with an  $x_+^F$  multiplying one of the arguments, the situation has to be considered more carefully. In close analogy to the previous case, the substitution  $\eta' = x_+^F \eta$  is performed. However,  $x_+^F$  is a function of  $\eta$ . Therefore, the full relationship between  $\eta$  and  $\eta'$  reads

$$\eta' = x_+^F \eta = \eta \left( 1 - \frac{4m_F^2}{\eta p \tilde{p}_{ij}} \right) = \eta - \frac{4m_F^2}{p \tilde{p}_{ij}}. \tag{A.47}$$

Also, in terms of  $\eta'$ , the definition of  $x_+^F$  itself must change,

$$x_+^F = 1 - \frac{4m_F^2}{\eta p \tilde{p}_{ij}} = 1 - \frac{4m_F^2 x_+^F}{\eta' p \tilde{p}_{ij}}, \tag{A.48}$$

resulting in

$$x_+^F = \left( 1 + \frac{4m_F^2}{\eta' p \tilde{p}_{ij}} \right)^{-1}. \quad (\text{A.49})$$

Once again,  $\eta'$  is renamed back to  $\eta$  and the summation is reordered over  $a$  and  $a'$  ( $b$  and  $b'$ ):

$$\begin{aligned} & \sum_{a,b} \int d\eta_1 d\eta_2 f_a(\eta_1, \mu_F^2) f_b(\eta_2, \mu_F^2) \\ & \quad \int_m \sum_F^N \left\{ \begin{aligned} & \sum_{a'} d\sigma_{a'b}^B(x_+^F \eta_1 p, \eta_2 \bar{p}) \delta^{a,a'} \left[ \int_0^1 dx \left( -g^{x_+^F}(x, \hat{s}(\eta_1)) \Theta(x_+^F - x) \right) + h^{x_+^F} \right] \\ & + \sum_{b'} d\sigma_{ab'}^B(\eta_1 p, x_+^F \eta_2 \bar{p}) \delta^{b,b'} \left[ \int_0^1 dx \left( -g^{x_+^F}(x, \hat{s}(\eta_2)) \Theta(x_+^F - x) \right) + h^{x_+^F} \right] \end{aligned} \right\} \\ & = \sum_{a,b} \int d\eta_1 d\eta_2 f_a(\eta_1, \mu_F^2) f_b(\eta_2, \mu_F^2) d\sigma_{ab}^B(\eta_1 p, \eta_2 \bar{p}) \\ & \quad \int_m \sum_F^N \left\{ \begin{aligned} & \Theta(x_+^F - \eta_1) \frac{f_a(\eta_1/x_+^F, \mu_F^2)}{f_a(\eta_1, \mu_F^2)} \left[ \int_0^1 dx \left( -g^{x_+^F}(x, \hat{s}(\eta_1 p/x_+^F)) \Theta(x_+^F - x) \right) + h^{x_+^F} \right] \\ & + \Theta(x_+^F - \eta_2) \frac{f_b(\eta_2/x_+^F, \mu_F^2)}{f_b(\eta_2, \mu_F^2)} \left[ \int_0^1 dx \left( -g^{x_+^F}(x, \hat{s}(\eta_2 \bar{p}/x_+^F)) \Theta(x_+^F - x) \right) + h^{x_+^F} \right] \end{aligned} \right\}. \end{aligned} \quad (\text{A.50})$$

Once these three contributions have been recombined, this leads schematically to an expression of the form

$$\begin{aligned}
& \sum_{a,b} \int d\eta_1 d\eta_2 f_a(\eta_1, \mu_F^2) f_b(\eta_2, \mu_F^2) \int_m d\sigma_{ab}^B(\eta_1 p, \eta_2 \bar{p}) \times \left\{ \mathbf{I}(\epsilon) \right. \\
& + \sum_{a'} \int_{\eta_1}^1 dx \left[ \frac{f_{a'}(\eta_1/x, \mu_F^2)}{x f_a(\eta_1, \mu_F^2)} \left( g^{a',a}(x, \hat{s}(\eta_1/x)) + k^{a',a}(x) + \delta^{a',a} \sum_F^{N_F} g^{x_+^F}(x) \right) \right. \\
& \quad \left. - \frac{f_{a'}(\eta_1, \mu_F^2)}{f_a(\eta_1, \mu_F^2)} \left( g^{a',a}(x, \hat{s}(\eta_1)) \right) \right] \\
& + \sum_{a'} \frac{f_{a'}(\eta_1, \mu_F^2)}{f_a(\eta_1, \mu_F^2)} \left( h^{a',a} - G^{a',a}(\eta_1) \right) \\
& - \sum_F^{N_F} \Theta(x_+^F - \eta_1) \frac{f_a(\eta_1/x_+^F, \mu_F^2)}{f_a(\eta_1, \mu_F^2)} \left[ \int_{\eta_1}^1 dx g^{x_+^F}(x) \Theta(x_+^F - x) + G^{x_+^F}(\eta_1) - h^{x_+^F} \right] \\
& \left. + \langle 1 \rightarrow 2, a \rightarrow b, a' \rightarrow b' \rangle \right\}, \tag{A.51}
\end{aligned}$$

where  $G(\eta) = \int_0^\eta dx g(x, \hat{s}(\eta/x))$  and  $G^{x_+^F}(\eta) = \int_0^\eta dx g^{x_+^F}(x, \hat{s}(\eta/x_+^F)) \Theta(x_+^F - x)$ , and  $G(\eta)$  and  $G^{x_+^F}(\eta)$  are calculated analytically.

## Appendix B.

# SUSY Integrated Dipole Phase Space Restriction Formulae

## B.1. Final state squark emitter, with final state spectator

Following the notation and conventions of reference [110], the phase space restricted integrated dipole term is given by

$$I_{ij,k}(\epsilon) \rightarrow I_{ij,k}(\epsilon, \alpha) = I_{ij,k}(\epsilon) + \Delta I_{ij,k}(\alpha) , \quad (\text{B.1})$$

where, for a squark (or anti-squark) emitter,

$$\Delta I_{g\tilde{Q},k} = C_F \left[ 2\Delta I^{\text{eik}} + \Delta I_{g\tilde{Q},k}^{\text{coll}} \right] . \quad (\text{B.2})$$

The eikonal integral  $\Delta I^{\text{eik}}$  is flavour and spin independent, and is thus given by Eq. (A.9) in reference [110].

The collinear integral is given by

$$\Delta I_{g\tilde{Q},k} = \left( 2(1+\alpha) - \frac{4(1-\mu_j^2)}{1-\mu_j^2-\mu_k^2} - 2 \log \left( \frac{\alpha(1-\mu_j^2-\mu_k^2)}{(1-\mu_k)^2-\mu_j^2} \right) \right) . \quad (\text{B.3})$$

The result above, following the conventions of reference [110], is given for the case where the imposed restriction on the phase space is given by the addition of the condition

$$y_{ij,k} < \alpha . \quad (\text{B.4})$$

The implementation in SHERPA imposes the restriction

$$y_{ij,k} < \alpha y_+ , \quad (\text{B.5})$$

for which the result is a trivial adaptation of equation (B.3), with the substitution

$$\alpha \rightarrow \alpha y_+ . \quad (\text{B.6})$$

## B.2. Final state squark emitter, with initial state spectator

The phase space restriction alters the ‘+’-distributions to ‘ $(1 - \alpha)$ ’-distributions, as defined in equation (A.3). Thus, the distributions given for the unrestricted case in reference [101], are modified to

$$[J_{g\tilde{q}}^a(x, \mu_{\tilde{q}}, \alpha)]_+ = \left( -\frac{2}{1-x} [1 + \ln(1-x + \mu_{\tilde{q}}^2)] \right)_{1-\alpha} + \left( \frac{2}{1-x} \right)_{1-\alpha} \ln(2 + \mu_{\tilde{q}}^2 - x) , \quad (\text{B.7})$$

and

$$\begin{aligned} J_{g\tilde{q}}^{a;\text{NS}}(\mu_{\tilde{q}}, \alpha) = & \frac{\pi^2}{3} - 2 \text{Li}_2\left(\frac{1}{1+\mu_{\tilde{q}}^2}\right) - 2 \text{Li}_2(-\mu_{\tilde{q}}^2) - \frac{1}{2} \ln^2(1 + \mu_{\tilde{q}}^2) \\ & + 2 \text{Li}_2\left(\frac{\alpha-1}{\mu^2}\right) - 2 \text{Li}_2\left(\frac{-1}{\mu^2}\right) - 2 \log(1-\alpha) \left( \log\left(\frac{\mu^2}{\mu^2+1} + 1\right) \right) , \end{aligned} \quad (\text{B.8})$$

while the singular endpoint part is unchanged.

# Appendix C.

## On-shell Subtraction Technicalities

### C.1. Reshuffling Procedure

One step of the on-shell subtraction procedure involves the reshuffling of the final state momenta, such that the resonant particle is on-shell. This involves adjusting the momenta of not just the two decay products, but also the momentum of at least one other particle, which, following Catani-Seymour language, we shall call the *spectator*. Therefore, a mapping must be defined from the set of original momenta, to the reshuffled momenta,

$$\{p_i, p_j, p_k\} \rightarrow \{\tilde{p}_i, \tilde{p}_j, \tilde{p}_k\} , \quad (C.1)$$

where we have used Catani-Seymour-like notation, with the resonance decay products' momenta denoted by  $p_i$  and  $p_j$ , and the spectator momentum denoted by  $p_k$ .

There is obviously a degree of arbitrariness in the definition of the reshuffling procedure; the only conditions which must be satisfied are

- that the resonant intermediate particle is on-shell

$$(\tilde{p}_i + \tilde{p}_j)^2 = m_{ij}^2 , \quad (C.2)$$

- that all final state momenta are on-shell

$$\tilde{p}_i^2 = m_i^2 , \tilde{p}_j^2 = m_j^2 , \tilde{p}_k^2 = m_k^2 , \quad (C.3)$$

- that energy-momentum conservation is preserved

$$Q = (p_i + p_j + p_k) = (\tilde{p}_i + \tilde{p}_j + \tilde{p}_k) , \quad (C.4)$$

- and that, when the resonant particle's unshuffled momentum is close to being on-shell, the reshuffling procedure minimises the changes to the momenta. In other words, in the limit that the unshuffled resonant momentum is on-shell, the reshuffling does not change any of the final state momenta,

$$\lim_{p^2 \rightarrow m^2} \{\tilde{p}_i, \tilde{p}_j, \tilde{p}_k\} \rightarrow \{p_i, p_j, p_k\} . \quad (C.5)$$

The reshuffling procedure may be effectively factorised into two independent stages. Firstly, the momenta of the spectator,  $p_k$ , and the resonance,  $p_{ij} = p_i + p_j$ , must be reshuffled to place the resonance on-shell. Secondly, the momenta of the two decay products must be adjusted, such that  $\tilde{p}_i + \tilde{p}_j = \tilde{p}_{ij}$ .

The kinematics for the first stage are very reminiscent of the Catani-Seymour final-final kinematic mapping for massive dipoles, where three final state momenta, for the emitter, unresolved and spectator partons, are combined to create two on-shell states. By definition, the momenta produced are on-shell, and conserve energy and momentum. The mapping also satisfies the last condition for a suitable procedure: when the resonant particle is already on-shell, the mapping does not change the momenta. This may be seen explicitly by setting  $(p_i + p_j)^2 = m_{ij}^2$  in the definition of the remapped momenta, giving

$$\begin{aligned} \tilde{p}_k^\mu &= \frac{\sqrt{\lambda(Q^2, m_{ij}^2, m_k^2)}}{\sqrt{\lambda(Q^2, (p_i + p_j)^2, m_k^2)}} \left( p_k^\mu - \frac{Q p_k}{Q^2} Q^\mu \right) + \frac{Q^2 + m_k^2 - m_{ij}^2}{2Q^2} Q^\mu \\ &= \frac{\sqrt{\lambda(Q^2, m_{ij}^2, m_k^2)}}{\sqrt{\lambda(Q^2, m_{ij}^2, m_k^2)}} \left( p_k^\mu - \frac{Q p_k}{Q^2} Q^\mu \right) + \frac{Q^2 + m_k^2 - m_{ij}^2}{2Q^2} Q^\mu \\ &= p_k^\mu + ((Q - p_k)^2 - m_{ij}^2) \frac{Q^\mu}{2Q^2} \\ &= p_k^\mu \\ \tilde{p}_{ij}^\mu &= Q^\mu - \tilde{p}_k^\mu \\ &= Q^\mu - p_k^\mu \\ &= p_i^\mu + p_j^\mu . \end{aligned} \quad (C.6)$$

where  $Q = p_i + p_j + p_k$ . Thus Catani-Seymour remapping may be used for the first stage of the reshuffling. However, for the dipole formalism, there is no requirement for definitions of the remapped decay product momenta, so this stage of the reshuffling procedure must be defined another way.

The two stages of the reshuffling involve similar manipulations: the kinematics in each case are basically those of a two-body decay. As such, in the centre of mass frame of the decay, given by  $p_{ij} + p_k$  in the first stage, and  $\tilde{p}_{ij}$  in the second stage, the energies and magnitude of the decay momenta are fully determined by energy-momentum conservation, but there is freedom in the choice of the direction of the momenta of the decay products.

The direction of reshuffled momenta of the decay products must be related to the direction of their unshuffled momenta, such that the direction is unchanged when the unshuffled momenta already have the resonance on-shell. Of course, after reshuffling, the decay products must be back-to-back in the centre of mass frame to conserve momentum. However, in general, the unshuffled momenta will not be back-to-back.

The spacial direction of the decay products in the centre of mass frame of the resonance is chosen to be the spacial direction of one of the unshuffled momenta in the same frame. The choice of which decay products' direction remains fixed is set by the user.

All possible combinations of the above reshuffling options are provided in SHERPA, and the results for different combinations have been compared. As expected, the details of the recombination procedure do not matter, the results agree for all possibilities.

## C.2. Higher Multiplicity Final States

For a  $2 \rightarrow 2$  process, with  $2 \rightarrow 3$  kinematics for the real emission, there is no ambiguity over the choice of spectator, as there is only one final state particle other than the resonance decay products. However, some choice of spectator must be made for processes with higher multiplicity final states.

This choice is, to some degree, arbitrary. It is therefore expected that the particular choice of spectator should not affect the overall result.

Several options for choices of spectator have been implemented:

- **Fixed choice** A final state spectator particle may be chosen by the user, and this spectator will be used for all phase space points.
- **furthest particle in phase space** For each point in phase space, the spectator is chosen to be the particle which gives the largest invariant mass when taken with the resonance. Using the notation above, this may be written as

$$\max_{k \neq i, j} \{Q_k^2\} , \quad (C.7)$$

where  $Q_k = p_i + p_j + p_k$ .

- **Closest particle in phase space** For each point in phase space, the spectator is chosen to be the particle which gives the smallest invariant mass when taken with the resonance. Using the notation above, this may be written as

$$\min_{k \neq i, j} \{Q_k^2\} . \quad (C.8)$$

- **Sum of all other momenta** The momenta of all particles, other than the resonance decay products, are summed. This total momentum is used as the spectator momentum. The result of the reshuffling, as it does not change the invariant mass of the spectator, translates to a collective Poincare transformation of all the spectator partons. This prescription has the advantage of preserving structure within the collective spectator body; for example, if there is another resonant structure within the spectators, this prescription is guaranteed not to move this second resonance off-shell.

In the case of a  $2 \rightarrow 3$  real emission process, a theta-function is applied to the subtraction term, of the form

$$\Theta \left( \sqrt{\hat{s}} - m_{ij} - m_k \right) , \quad (C.9)$$

where  $\hat{s}$  is the partonic centre of mass energy. This theta function guarantees that the subtraction term only contributes for phase space points where there is enough centre of mass energy to put both the spectator and the resonance on-shell.

A similar theta-function must be applied to subtraction terms for higher multiplicity final states. However, in this case, it is not sufficient to ensure there is enough total centre of mass energy to create all particles on-shell. The necessary generalisation of the

above formula ensures that the invariant mass of the spectator and resonance must be greater than the sum of the individual invariant masses.

$$\Theta \left( \sqrt{Q^2} - m_{ij} - \sqrt{p_k^2} \right) , \quad (C.10)$$

where  $Q^2 = p_i + p_j + p_k$ .

# Appendix D.

## Photonic Corrections

### D.1. Notation and Conventions

As in reference [54],  $\sigma_f$  will denote a charge flow sign factor; where  $\sigma_f = +1$  for incoming fermions and outgoing anti-fermions, and  $\sigma_f = -1$  for incoming anti-fermions and outgoing fermions.  $Q_f$  will denote the charge of fermion  $f$ . As such, charge conservation is expressed as

$$\sum_f Q_f \sigma_f = 0. \quad (\text{D.1})$$

Following reference [56] we will work in  $d = 4 - 2\epsilon$  space-time dimensions.

### D.2. Integrated Subtraction Terms

Below follows a summary of the integrated subtraction terms, for QED dipoles using dimensional regularisation, using the notation of reference [56].

$$\begin{aligned} \int_{m+1} d\sigma_{ab}^A(p, \bar{p}) + \int_m d\sigma_{ab}^C(p, \bar{p}; \mu_F^2) &= \int_m [d\sigma_{ab}^B(p, \bar{p}) \cdot \mathbf{I}(\epsilon)] \\ &+ \sum_{a'} \int_0^1 dx \int_m [\mathbf{K}^{a,a'}(x) \cdot d\sigma_{a'b}^B(xp, \bar{p})] + \sum_{a'} \int_0^1 dx \int_m [\mathbf{P}^{a,a'}(xp, x; \mu_F^2) \cdot d\sigma_{a'b}^B(xp, \bar{p})] \\ &+ \sum_{b'} \int_0^1 dx \int_m [\mathbf{K}^{b,b'}(x) \cdot d\sigma_{ab'}^B(p, x\bar{p})] + \sum_{b'} \int_0^1 dx \int_m [\mathbf{P}^{b,b'}(x\bar{p}, x; \mu_F^2) \cdot d\sigma_{ab'}^B(p, x\bar{p})] \quad , \end{aligned} \quad (\text{D.2})$$

where  $\mathbf{I}(\epsilon)$ ,  $\mathbf{K}^{a,b}(x)$  and  $\mathbf{P}^{a,b}(xp, x; \mu_F^2)$  are:

$$\begin{aligned} \mathbf{I}(p_1, \dots, p_m, p_a, p_b; \epsilon) = & -\frac{\alpha}{2\pi} \frac{1}{\Gamma(1-\epsilon)} \left( \frac{2}{\epsilon^2} + \frac{1}{\epsilon} + 10\pi^2 \right) \sum_i \left[ \sum_{k>i} \sigma_i Q_i \sigma_k Q_k \left( \frac{4\pi\mu^2}{2p_i \cdot p_k} \right)^\epsilon \right. \\ & \left. + \sigma_i Q_i \sigma_a Q_a \left( \frac{4\pi\mu^2}{2p_i \cdot p_a} \right)^\epsilon + \sigma_i Q_i \sigma_b Q_b \left( \frac{4\pi\mu^2}{2p_i \cdot p_b} \right)^\epsilon + \sigma_b Q_b \sigma_a Q_a \left( \frac{4\pi\mu^2}{2p_b \cdot p_a} \right)^\epsilon \right] , \end{aligned}$$

$$\begin{aligned} \mathbf{K}^{a,a'}(x) = & \frac{\alpha}{2\pi} \left\{ \overline{K}^{aa'}(x) - K_{\text{FS}}^{aa'}(x) \right. \\ & \left. + \delta^{aa'} \sum_i \sigma_a Q_a \sigma_i Q_i \gamma_i \left[ \left( \frac{1}{1-x} \right)_+ + \delta(1-x) \right] \right\} , \end{aligned}$$

$$\begin{aligned} \mathbf{P}^{f,f'}(p_1, \dots, p_m, p_b; xp_f, x; \mu_F^2) = & \frac{\alpha}{2\pi} \left( \frac{1+x^2}{1-x} \right)_+ \left[ \sum_i \sigma_i Q_i \sigma_f Q_f \ln \frac{\mu_F^2}{2xp_f \cdot p_i} + \sigma_f Q_f \sigma_b Q_b \ln \frac{\mu_F^2}{2xp_f \cdot p_b} \right] , \end{aligned}$$

$$\begin{aligned} \mathbf{P}^{f,p}(p_1, \dots, p_m, p_b; xp_f, x; \mu_F^2) = & -\frac{\alpha}{2\pi} \frac{1+(1-x)^2}{x} \left[ Q_f^2 \ln \frac{\mu_F^2}{2xp_f \cdot p_b} \right] , \end{aligned}$$

$$\begin{aligned} \mathbf{P}^{p,f}(p_1, \dots, p_m, p_b; xp_p, x; \mu_F^2) = & -\frac{\alpha}{2\pi} x^2 + (1-x)^2 \left[ Q_f^2 \ln \frac{\mu_F^2}{2xp_p \cdot p_b} \right] , \end{aligned}$$

$$\begin{aligned} \overline{K}^{fp}(x) &= \left\{ -\frac{1+(1-x)^2}{x} \ln x + x \right\} Q_f^2 , \\ \overline{K}^{pf}(x) &= \left\{ -(x^2 + (1-x)^2) \ln x + 2x(1-x) \right\} Q_f^2 , \\ \overline{K}^{ff}(x) &= \left\{ \left( \frac{2}{1-x} \ln \frac{1-x}{x} \right)_+ - (1+x) \ln \frac{1-x}{x} + (1-x) - \delta(1-x) (5 - \pi^2) \right\} Q_f^2 \\ &+ \left\{ -(1+x) \ln(1-x) + \left( \frac{2}{1-x} \ln(1-x) \right)_+ - \frac{\pi^2}{3} \delta(1-x) \right\} \sigma_f Q_f \sigma_b Q_b , \end{aligned} \tag{D.3}$$

where the indices  $i$  and  $k$  run over final state charged particles, indices  $a$  and  $b$  denote initial state partons, and  $p$  denotes photons.



# Colophon

This thesis was made in L<sup>A</sup>T<sub>E</sub>X 2 <sub>$\varepsilon$</sub>  using the “heptesis” class [153].

# Bibliography

- [1] The ATLAS, G. Aad *et al.*, (2009), 0901.0512.
- [2] A. Buckley *et al.*, Phys. Rept. **504**, 145 (2011), 1101.2599.
- [3] T. Gleisberg *et al.*, JHEP **02**, 007 (2009), 0811.4622.
- [4] G. Corcella *et al.*, (2002), hep-ph/0210213.
- [5] M. Bahr *et al.*, (2008), 0812.0529.
- [6] T. Sjöstrand, S. Mrenna, and P. Skands, JHEP **05**, 026 (2006), hep-ph/0603175.
- [7] T. Sjöstrand, S. Mrenna, and P. Skands, Comput. Phys. Commun. **178**, 852 (2008), 0710.3820.
- [8] L. Lönnblad, Comput. Phys. Commun. **71**, 15 (1992).
- [9] R. K. Ellis, W. J. Stirling, and B. R. Webber, Camb. Monogr. Part. Phys. Nucl. Phys. Cosmol. **8**, 1 (1996).
- [10] M. E. Peskin and D. V. Schroeder, Reading, USA: Addison-Wesley (1995) 842 p.
- [11] S. Weinberg, Cambridge, UK: Univ. Pr. (1995) 609 p.
- [12] H. D. Politzer, Phys. Rev. Lett. **30**, 1346 (1973).
- [13] D. J. Gross and F. Wilczek, Phys. Rev. **D8**, 3633 (1973).
- [14] J. C. Collins, D. E. Soper, and G. F. Sterman, Nucl. Phys. **B261**, 104 (1985).
- [15] S. Catani, F. Krauss, R. Kuhn, and B. R. Webber, JHEP **11**, 063 (2001), hep-ph/0109231.
- [16] L. Lönnblad, JHEP **05**, 046 (2002), hep-ph/0112284.
- [17] J. Alwall *et al.*, Eur. Phys. J. **C53**, 473 (2008), 0706.2569.

- [18] S. Mrenna and P. Richardson, JHEP **05**, 040 (2004), hep-ph/0312274.
- [19] S. Höche, F. Krauss, S. Schumann, and F. Siegert, JHEP **05**, 053 (2009), 0903.1219.
- [20] K. Hamilton, P. Richardson, and J. Tully, JHEP **11**, 038 (2009), 0905.3072.
- [21] X. Artru and G. Mennessier, Nucl. Phys. **B70**, 93 (1974).
- [22] M. G. Bowler, Z. Phys. **C11**, 169 (1981).
- [23] B. Andersson, G. Gustafson, and B. Söderberg, Z. Phys. **C20**, 317 (1983).
- [24] R. D. Field and S. Wolfram, Nucl. Phys. **B213**, 65 (1983).
- [25] B. R. Webber, Nucl. Phys. **B238**, 492 (1984).
- [26] P. Bartalini, (ed. ) *et al.*, (2010), 1003.4220.
- [27] T. Sjöstrand and P. Z. Skands, JHEP **03**, 053 (2004), hep-ph/0402078.
- [28] G. Gustafson, (2007), 0712.1941.
- [29] S. Frixione and B. R. Webber, JHEP **06**, 029 (2002), hep-ph/0204244.
- [30] P. Nason, JHEP **11**, 040 (2004), hep-ph/0409146.
- [31] S. Frixione, P. Nason, and C. Oleari, JHEP **11**, 070 (2007), 0709.2092.
- [32] S. Hoche, F. Krauss, M. Schonherr, and F. Siegert, JHEP **04**, 024 (2011), 1008.5399.
- [33] K. Hamilton and P. Nason, JHEP **06**, 039 (2010), 1004.1764.
- [34] S. Hoche, F. Krauss, M. Schonherr, and F. Siegert, (2010), 1009.1127.
- [35] C. F. Berger *et al.*, Phys. Rev. **D78**, 036003 (2008), 0803.4180.
- [36] T. Binoth, J. P. Guillet, G. Heinrich, E. Pilon, and T. Reiter, Comput. Phys. Commun. **180**, 2317 (2009), 0810.0992.
- [37] R. K. Ellis, W. T. Giele, Z. Kunszt, K. Melnikov, and G. Zanderighi, JHEP **01**, 012 (2009), 0810.2762.
- [38] G. Ossola, C. G. Papadopoulos, and R. Pittau, JHEP **03**, 042 (2008), 0711.3596.
- [39] A. van Hameren, C. G. Papadopoulos, and R. Pittau, JHEP **09**, 106 (2009),

0903.4665.

- [40] A. van Hameren, (2010), 1007.4716.
- [41] V. Hirschi *et al.*, JHEP **05**, 044 (2011), 1103.0621.
- [42] G. Belanger *et al.*, Phys. Rept. **430**, 117 (2006), hep-ph/0308080.
- [43] J.-C. Winter and W. T. Giele, (2009), 0902.0094.
- [44] T. Kinoshita, J. Math. Phys. **3**, 650 (1962).
- [45] T. D. Lee and M. Nauenberg, Phys. Rev. **133**, B1549 (1964).
- [46] F. Bloch and A. Nordsieck, Phys. Rev. **52**, 54 (1937).
- [47] H. Baer, J. Ohnemus, and J. F. Owens, Phys. Rev. **D40**, 2844 (1989).
- [48] B. W. Harris and J. F. Owens, Phys. Rev. **D65**, 094032 (2002), hep-ph/0102128.
- [49] K. Fabricius, I. Schmitt, G. Kramer, and G. Schierholz, Zeit. Phys. **C11**, 315 (1981).
- [50] G. Kramer and B. Lampe, Fortschr. Phys. **37**, 161 (1989).
- [51] W. T. Giele and E. W. N. Glover, Phys. Rev. **D46**, 1980 (1992).
- [52] W. T. Giele, E. W. N. Glover, and D. A. Kosower, Nucl. Phys. **B403**, 633 (1993), hep-ph/9302225.
- [53] T. O. Eynck, E. Laenen, L. Phaf, and S. Weinzierl, Eur. Phys. J. **C23**, 259 (2002), hep-ph/0109246.
- [54] S. Dittmaier, Nucl. Phys. **B565**, 69 (2000), hep-ph/9904440.
- [55] S. Frixione, Z. Kunszt, and A. Signer, Nucl. Phys. **B467**, 399 (1996), hep-ph/9512328.
- [56] S. Catani and M. H. Seymour, Nucl. Phys. **B485**, 291 (1997), hep-ph/9605323.
- [57] J. M. Campbell, M. A. Cullen, and E. W. N. Glover, Eur. Phys. J. **C9**, 245 (1999), hep-ph/9809429.
- [58] Z. Kunszt and D. E. Soper, Phys. Rev. **D46**, 192 (1992).
- [59] Z. Nagy and Z. Trocsanyi, Nucl. Phys. **B486**, 189 (1997), hep-ph/9610498.

- [60] S. Weinzierl, JHEP **07**, 052 (2003), hep-ph/0306248.
- [61] R. K. Ellis, D. A. Ross, and A. E. Terrano, Nucl. Phys. **B178**, 421 (1981).
- [62] C.-H. Chung, M. Kramer, and T. Robens, JHEP **06**, 144 (2011), 1012.4948.
- [63] D. A. Kosower, Phys. Rev. **D57**, 5410 (1998), hep-ph/9710213.
- [64] D. A. Kosower, Phys. Rev. **D71**, 045016 (2005), hep-ph/0311272.
- [65] A. Gehrmann-De Ridder, T. Gehrmann, and E. W. N. Glover, JHEP **09**, 056 (2005), hep-ph/0505111.
- [66] T. Gleisberg and F. Krauss, Eur. Phys. J. **C53**, 501 (2008), 0709.2881.
- [67] M. H. Seymour and C. Tevlin, (2008), 0803.2231.
- [68] R. Frederix, T. Gehrmann, and N. Greiner, JHEP **09**, 122 (2008), 0808.2128.
- [69] R. Frederix, T. Gehrmann, and N. Greiner, JHEP **06**, 086 (2010), 1004.2905.
- [70] T. Gehrmann and N. Greiner, JHEP **12**, 050 (2010), 1011.0321.
- [71] R. Frederix, S. Frixione, F. Maltoni, and T. Stelzer, JHEP **10**, 003 (2009), 0908.4272.
- [72] K. Hasegawa, S. Moch, and P. Uwer, Comput. Phys. Commun. **181**, 1802 (2010), 0911.4371.
- [73] K. Hasegawa, Eur. Phys. J. **C70**, 285 (2010), 1007.1585.
- [74] S. Catani, M. H. Seymour, and Z. Trocsanyi, Phys. Rev. **D55**, 6819 (1997), hep-ph/9610553.
- [75] Z. Kunszt, A. Signer, and Z. Trocsanyi, Nucl. Phys. **B411**, 397 (1994), hep-ph/9305239.
- [76] J. Smith and W. L. van Neerven, Eur. Phys. J. **C40**, 199 (2005), hep-ph/0411357.
- [77] A. Signer and D. Stockinger, Nucl. Phys. **B808**, 88 (2009), 0807.4424.
- [78] F. A. Berends and G. B. West, Phys. Rev. **D1**, 122 (1970).
- [79] Y. Kurihara, D. Perret-Gallix, and Y. Shimizu, Phys. Lett. **B349**, 367 (1995), hep-ph/9412215.

- [80] E. N. Argyres *et al.*, Phys. Lett. **B358**, 339 (1995), hep-ph/9507216.
- [81] A. Denner, S. Dittmaier, M. Roth, and D. Wackerlo, Nucl. Phys. **B587**, 67 (2000), hep-ph/0006307.
- [82] A. Aeppli, F. Cuypers, and G. J. van Oldenborgh, Phys. Lett. **B314**, 413 (1993), hep-ph/9303236.
- [83] W. Beenakker *et al.*, Nucl. Phys. **B500**, 255 (1997), hep-ph/9612260.
- [84] R. G. Stuart, Phys. Lett. **B262**, 113 (1991).
- [85] A. Aeppli, G. J. van Oldenborgh, and D. Wyler, Nucl. Phys. **B428**, 126 (1994), hep-ph/9312212.
- [86] U. Baur and D. Zeppenfeld, Phys. Rev. Lett. **75**, 1002 (1995), hep-ph/9503344.
- [87] G. Passarino, Nucl. Phys. **B574**, 451 (2000), hep-ph/9911482.
- [88] E. Accomando, A. Ballestrero, and E. Maina, Phys. Lett. **B479**, 209 (2000), hep-ph/9911489.
- [89] W. Beenakker, F. A. Berends, and A. P. Chapovsky, Nucl. Phys. **B573**, 503 (2000), hep-ph/9909472.
- [90] W. Beenakker, A. P. Chapovsky, A. Kanaki, C. G. Papadopoulos, and R. Pittau, Nucl. Phys. **B667**, 359 (2003), hep-ph/0303105.
- [91] M. Beneke, A. P. Chapovsky, A. Signer, and G. Zanderighi, Nucl. Phys. **B686**, 205 (2004), hep-ph/0401002.
- [92] M. Beneke, A. P. Chapovsky, A. Signer, and G. Zanderighi, Phys. Rev. Lett. **93**, 011602 (2004), hep-ph/0312331.
- [93] G. Altarelli, (Ed. ), T. Sjostrand, (Ed. ), and F. Zwirner, (Ed. ), REPORT-NUM-CERN-96-01.
- [94] A. Denner, S. Dittmaier, M. Roth, and D. Wackerlo, Nucl. Phys. **B560**, 33 (1999), hep-ph/9904472.
- [95] A. Denner, S. Dittmaier, M. Roth, and L. H. Wieders, Nucl. Phys. **B724**, 247 (2005), hep-ph/0505042.
- [96] A. Denner and S. Dittmaier, Nucl. Phys. Proc. Suppl. **160**, 22 (2006),

hep-ph/0605312.

[97] R. G. Stuart, In \*Les Arcs 1990, Proceedings, Z0 physics\* 41-49. (see Conference Index).

[98] S. Dittmaier and M. Huber, JHEP **01**, 060 (2010), 0911.2329.

[99] P. Skands *et al.*, JHEP **07**, 036 (2004), hep-ph/0311123.

[100] T. Hahn, (2004), hep-ph/0408283.

[101] S. Catani, S. Dittmaier, M. H. Seymour, and Z. Trocsanyi, Nucl. Phys. **B627**, 189 (2002), hep-ph/0201036.

[102] M. Czakon, C. G. Papadopoulos, and M. Worek, JHEP **08**, 085 (2009), 0905.0883.

[103] S. Dittmaier, A. Kabelschacht, and T. Kasprzik, Nucl. Phys. **B800**, 146 (2008), 0802.1405.

[104] G. P. Salam, Eur. Phys. J. **C67**, 637 (2010), 0906.1833.

[105] Z. Nagy and Z. Trocsanyi, Phys. Rev. **D59**, 014020 (1999), hep-ph/9806317.

[106] Z. Nagy, Phys. Rev. **D68**, 094002 (2003), hep-ph/0307268.

[107] A. D. Martin, W. J. Stirling, R. S. Thorne, and G. Watt, Eur. Phys. J. **C70**, 51 (2010), 1007.2624.

[108] S. Catani, S. Dittmaier, and Z. Trocsanyi, Phys. Lett. **B500**, 149 (2001), hep-ph/0011222.

[109] J. M. Campbell, R. K. Ellis, and F. Tramontano, Phys. Rev. **D70**, 094012 (2004), hep-ph/0408158.

[110] G. Bevilacqua, M. Czakon, C. G. Papadopoulos, R. Pittau, and M. Worek, JHEP **09**, 109 (2009), 0907.4723.

[111] J. M. Campbell and F. Tramontano, Nucl. Phys. **B726**, 109 (2005), hep-ph/0506289.

[112] S. P. Martin, (1997), hep-ph/9709356.

[113] P. Fayet and S. Ferrara, Phys. Rept. **32**, 249 (1977).

[114] F. Cooper and B. Freedman, Ann. Phys. **146**, 262 (1983).

- [115] M. F. Sohnius, Phys. Rept. **128**, 39 (1985).
- [116] F. Cooper, A. Khare, and U. Sukhatme, Phys. Rept. **251**, 267 (1995), hep-th/9405029.
- [117] A. Signer, J. Phys. **G36**, 073002 (2009), 0905.4630.
- [118] S. R. Coleman and J. Mandula, Phys. Rev. **159**, 1251 (1967).
- [119] R. Haag, J. T. Łopuszański, and M. Sohnius, Nucl. Phys. **B88**, 257 (1975).
- [120] S. Weinberg, Phys. Rev. **D13**, 974 (1976).
- [121] S. Weinberg, Phys. Rev. **D19**, 1277 (1979).
- [122] E. Gildener, Phys. Rev. **D14**, 1667 (1976).
- [123] L. Susskind, Phys. Rev. **D20**, 2619 (1979).
- [124] G. 't Hooft, (ed. ) *et al.*, NATO Adv. Study Inst. Ser. B Phys. **59**, 1 (1980).
- [125] S. Dimopoulos and S. Raby, Nucl. Phys. **B192**, 353 (1981).
- [126] E. Witten, Nucl. Phys. **B188**, 513 (1981).
- [127] M. Dine, W. Fischler, and M. Srednicki, Nucl. Phys. **B189**, 575 (1981).
- [128] S. Dimopoulos and H. Georgi, Nucl. Phys. **B193**, 150 (1981).
- [129] R. K. Kaul and P. Majumdar, Nucl. Phys. **B199**, 36 (1982).
- [130] N. Sakai, Zeit. Phys. **C11**, 153 (1981).
- [131] H. Goldberg, Phys. Rev. Lett. **50**, 1419 (1983).
- [132] J. R. Ellis, J. S. Hagelin, D. V. Nanopoulos, K. A. Olive, and M. Srednicki, Nucl. Phys. **B238**, 453 (1984).
- [133] G. G. Ross, Reading, Usa: Benjamin/cummings ( 1984) 497 P. ( Frontiers In Physics, 60).
- [134] P. Van Nieuwenhuizen, Phys. Rept. **68**, 189 (1981).
- [135] T. M. P. Tait, Phys. Rev. **D61**, 034001 (2000), hep-ph/9909352.
- [136] S. Zhu, Phys. Lett. **B524**, 283 (2002).
- [137] S. Frixione, E. Laenen, P. Motylinski, B. R. Webber, and C. D. White, JHEP **07**,

029 (2008), 0805.3067.

[138] C. D. White, S. Frixione, E. Laenen, and F. Maltoni, *JHEP* **11**, 074 (2009), 0908.0631.

[139] W. Beenakker, R. Hopker, M. Spira, and P. M. Zerwas, *Nucl. Phys.* **B492**, 51 (1997), hep-ph/9610490.

[140] W. Beenakker *et al.*, *Phys. Rev. Lett.* **83**, 3780 (1999), hep-ph/9906298.

[141] E. Re, *Eur. Phys. J.* **C71**, 1547 (2011), 1009.2450.

[142] E. L. Berger, T. Han, J. Jiang, and T. Plehn, *Phys. Rev.* **D71**, 115012 (2005), hep-ph/0312286.

[143] C. Weydert *et al.*, *Eur. Phys. J.* **C67**, 617 (2010), 0912.3430.

[144] T. Binoth *et al.*, (2011), 1108.1250.

[145] G. Corcella *et al.*, (2007), hep-ph/0210213.

[146] K. P. O. Diener, S. Dittmaier, and W. Hollik, *Phys. Rev.* **D72**, 093002 (2005), hep-ph/0509084.

[147] A. D. Martin, R. G. Roberts, W. J. Stirling, and R. S. Thorne, *Eur. Phys. J.* **C39**, 155 (2005), hep-ph/0411040.

[148] S. Brensing, S. Dittmaier, M. Kramer, 1, and A. Muck, *Phys. Rev.* **D77**, 073006 (2008), 0710.3309.

[149] J. M. Campbell and R. K. Ellis, *Phys. Rev.* **D62**, 114012 (2000), hep-ph/0006304.

[150] P. Falgari, P. Mellor, and A. Signer, *Phys. Rev.* **D82**, 054028 (2010), 1007.0893.

[151] B. W. Harris, E. Laenen, L. Phaf, Z. Sullivan, and S. Weinzierl, *Phys. Rev.* **D66**, 054024 (2002), hep-ph/0207055.

[152] T. Binoth *et al.*, *Comput. Phys. Commun.* **181**, 1612 (2010), 1001.1307.

[153] A. Buckley, The *hepthesis* L<sup>A</sup>T<sub>E</sub>X class.

# List of Figures

1.1. A pictorial representation of a Monte Carlo event ( <a href="http://www.sherpa-mc.de">www.sherpa-mc.de</a> ) . . . . .	4
1.2. Schematic diagrams of NLO contributions . . . . .	10
3.1. Schematic representation of the dipole splitting functions . . . . .	36
5.1. Diagrams of LO contributions to squark-gluino production . . . . .	55
5.2. Diagrams of NLO real-emission contributions to squark-gluino production .	56
5.3. Diagrams of LO contributions to $Wt$ production . . . . .	58
5.4. Diagrams of NLO real-emission contributions to $Wt$ production . . . . .	59
7.1. Plots of subtracted real NLO contributions as functions of $\alpha_{tech}$ . . . . .	67
7.2. Plots of subtracted real NLO contributions in bins of $y_{min}$ . . . . .	69
7.3. Number of QCD subtraction terms - $W$ -jets . . . . .	71
7.4. Number of QCD subtraction terms - single top, and top pair production	72
7.5. Number of QED subtraction terms - $W$ , $Z$ , $WW$ , $WZ$ , $ZZ$ production .	73
7.6. Alpha variation for QCD corrections to processes with massive partons .	74
7.7. Alpha variation for QCD corrections to SUSY processes . . . . .	75
7.8. Alpha variation for QED corrections to various processes . . . . .	76
7.9. Comparison of on-shell spectator choices . . . . .	77
7.10. Comparison of various on-shell reshuffling procedures . . . . .	78
7.12. On-shell subtraction width variation . . . . .	80

7.13. On-shell subtraction for $pp \rightarrow tW$ subprocesses . . . . .	81
7.14. QCD NLO $\eta_t$ distribution comparison to MCFM for $pp \rightarrow t\bar{t}$ . . . . .	84
7.15. QCD NLO $P_t(t)$ distribution comparison to MCFM for $pp \rightarrow t\bar{t}$ . . . . .	85
7.16. EW NLO $P_t(l^-)$ distribution comparison to RADY for $pp \rightarrow l^+l^-$ . . . . .	86
7.17. EW NLO invariant mass distribution comparison to RADY for $pp \rightarrow l^+l^-$ . . . . .	87
7.18. EW NLO $y_{\mu^-}$ distribution comparison to RADY for $pp \rightarrow l^+l^-$ . . . . .	88

# List of Tables

3.1. Number of dipoles for $W + ng$ processes	38
3.2. Number of dipoles for $t\bar{t} + ng$	39
3.3. Dipole phase space cuts	41
7.1. MCFM cross section comparison for $t\bar{t}$	82
A.1. Rescaled masses	91